UNIVERSITÀ DEGLI STUDI DI TRIESTE

UNIVERSITÀ DEGLI STUDI DI UDINE

XXXI CICLO DEL DOTTORATO DI RICERCA IN

AMBIENTE E VITA

Assessing sediment dynamics and check dams efficiency in a debris-flow catchment using multi-temporal topographic surveys

Settore scientifico-disciplinare:

AGR/08 IDRAULICA AGRARIA E SISTEMAZIONI IDRAULICO-FORESTALI

DOTTORANDA
SARA CUCCHIARO

COORDINATORE
Prof. GIORGIO ALBERTI

SUPERVISORE DI TESI
Prof. FEDERICO CAZORZI

CO-SUPERVISORE DI TESI
Dott. MARCO CAVALLI

ANNO ACCADEMICO 2017/2018

To the Moscardo, that has taught me
so much in these years...

Abstract

Torrent control works have always been a fundamental tool for preventing torrential hazard in mountain catchments, where the sediment transport phenomena as debris flows are one of the most dangerous geomorphic processes affecting small steep basins. The linkages between sediment source areas on the hillslopes and channel network, along with the temporal and spatial distributions of channel storage, are key controls of debris-flow occurrence and magnitude. Consequently, the prevention of natural hazards related to debris-flows requires a better understanding of sediment dynamic. Among the hydraulic engineering structures, grade control dams and sediment retention dams are the most effective and common technique to manage debris flows and debris floods hazard. These structures could have important effects on sediment dynamics. Therefore, an integrated approach that analyses the debris-flow dynamic and its interactions with torrent control works is needed to assess the efficiency of the realized structures and to improve the long-term hazard management at catchment scale. In spite of the widespread presence of such hydraulic structures in steep mountain streams worldwide, very little researches considered the role of check dams on sediment dynamics in debris-flow environments over time to enhance the planning of the torrent control works. The monitoring of debris-flow events, the estimation of debris-flow magnitude and frequency, and the analysis of spatial patterns in terms of eroded and deposited volumes, are fundamental to improve the sediment dynamic understanding. In the last two decades, High-Resolution Topography (HRT) has provided new opportunities to characterize debris-flow activity at different scales. Between these, the application of Structure from Motion (SfM) photogrammetry paired with Multi-View Stereo (MVS) algorithms has become a low-cost method to collect HRT at multiple temporal and spatial scales, also in rugged or inaccessible environments like those observed in debris-flow catchments. SfM allows carrying out HRT with high frequency; nevertheless, the SfM technique is limited at broad spatial scales. Therefore, other technologies as LiDAR surveys could be used to assess the sediment dynamic also at catchment scale. However, the use of HRT required the design of appropriate workflows for data post-processing and uncertainty assessment to compare multi-temporal surveys, especially in a topographically complex environment.

In this research, the effects of torrent control works on debris-flow dynamics were investigated by means of multi-temporal SfM and LiDAR surveys in the Moscardo torrent (eastern Italian Alps) where several check dams have been built over time. Methodological workflows enabled the realization of multi-temporal Digital Elevation Models (DEMs) which were compared (i.e., DoD) to quantify the debris mobilized and the time evolution of erosion and deposition patterns

in debris-flow channels equipped with check dams. The DoDs data were integrated with a sediment connectivity analysis to have a whole assessment of debris-flow dynamic.

The results show that the check dams considerably modified debris-flow dynamics in the studied channel but their performance cannot be considered satisfactory. They temporary stored volumes of debris just after their construction, but soon when the structures were filled the check dams acted as sediment sources that increased debris-flow magnitude. Moreover, the sediment paths flowed around some check dams. These processes triggered the slope foot erosion and activated shallow landslides, further sediment source areas for debris-flow process. The analysis proposed in this work could help to improve design approaches and to obtain more realistic cost-benefit ratios of the adopted strategies and, in this way, select the best solutions.

Abbreviations

CPs: (Control Points)

CI: (Confidence Interval)

DEM: (Digital Elevation Models)

DoD: (DEM of Difference)

DoIC: (Difference of Connectivity Index)

FIS: (Fuzzy Inference System)

GCD: (Geomorphic Change Detection)

GCPs: (Ground Control Points)

GNSS: (Global Navigation Satellite System)

GPS: (Global Positioning System)

HRT: (High-Resolution Topography)

ICP: (Iterative Closest Point)

IC: (Index of Connectivity)

IR: (Infrared)

minLoD: (minimum Level of Detection)

M3C2: (Multiscale Model to Model Cloud Comparison)

MVS: (Multi-View Stereo)

NRTK: Network Real Time Kinematic

LiDAR: (Light Detection And Ranging)

RINEX: (Receiver Independent Exchange Format)

RMSE: (Root Mean Square Error)

RTK: (Real-Time Kinematic)

SfM: (Structure from Motion)

SD: (Standard Deviation)

TIN (Triangular Irregular Network)

TLS: (Terrestrial Laser Scanner)

ToPCAT: (Topographic Point Cloud Analysis Toolkit)

UAV: (Unmanned Aerial Vehicle)

Contents

Abstract 4

Abbreviations 6

1. Introduction 9

1.1 State of the art 9

1.1.1 Debris-flow phenomena 9

1.1.2 Structural measures and debris-flow dynamics 10

1.1.3 Debris-flow monitoring 11

1.1.4 Multi-temporal HRT to assess sediment dynamics 16

1.2 Thesis aims and outline 18

2. Study catchment: The Moscardo Torrent 20

2.1 Geomorphological and geological settings 21

2.2 Monitoring of debris-flow events 23

2.3 Torrent control works in the catchment 25

3. Methods 27

3.1 Measurement and estimation of debris-flow events 27

3.2 SfM photogrammetry: workflow for monitoring geomorphic changes in mountain torrents 28

3.2.1 Survey planning 30

3.2.2 Data acquisition 32

3.2.3 Data post-processing 33

3.2.4 Error analysis 37

3.2.5 DEMs generation 39

3.2.6 DoD and budget segregation 40

3.3 LiDAR workflow 40

3.3.1 LiDAR surveys 41

3.3.2 LiDAR Point clouds georeferencing and co-registration processes 44

3.3.3 DEM generation and co-registration process 44

3.3.4 DoDs generation and error analysis 45
3.4 Index of Connectivity (IC) and Difference of IC (DoIC) 48
3.5 Inventory of torrent control works 49
4. Results and discussion 51
4.1 Volumes of debris-flow events 51
4.2 Database of torrent control works 54
4.3 SfM data 59
4.3.1 Acquisition and data processing 59
4.3.2 Post-processing point clouds 65
4.3.3 Data and error analysis 68
4.3.4 DoDs and Budget segregation at check dams scale 75
4.3.5 The sediment dynamic at check dams scale 81
4.4 LiDAR data 87
4.4.1 Co-registration processes 87
4.4.2 DoDs at catchment scale 91
4.4.3 DoDs and check dams 93
4.4.4 Index of Connectivity (IC) and Difference of IC 99
4.4.5 DoD and Difference of IC 105
4.4.6 The sediment dynamics and check dams at catchment scale 108
5. Final Remarks and Conclusions 111
References 113
Acknowledgements 130

1. Introduction

1.1 State of the art

Humans have always tried to limit the geomorphic activity of mountain streams, and related damage in populated areas, using mitigation measures based on non-structural and structural interventions (Hübl et al., 2005; Osti and Egashira 2008; Piton et al., 2016). Therefore, the combination of land use planning, non-structural countermeasures (e.g., warning systems: Kienholz, 2003; Coviello et al., 2015; Ballesteros Cánovas et al., 2016), bioengineering interventions (e.g., living slope grids, double row palisades; Hübl et al., 2005) and technical structures (e.g. check dams, retention basins, levees; Osti and Egashira, 2008; Piton et al., 2016) have always been a fundamental tool for preventing torrential hazard in mountain catchments (Hübl and Suda, 2008). In particular, structural countermeasures concern widespread hillslope intervention and channel control works. The first aim to prevent erosion and sediment supply such as reforestation, bioengineering, drainage network, and landslide stabilization works. The second may affect the initiation, transport or deposition of hydro-erosive processes changing the magnitude and frequency characteristics of events (Hübl and Fiebiger, 2005). These interventions can limit the causes and reduce the effects of hydro erosive processes that represent one of the most common and widespread natural hazards in mountain environments. Therefore, catchment-scale hydraulic control plans have emerged in order to reduce erosion, sediment transport and the risk for economic activities, endanger routes, urban areas or exposed elements located on or near the alluvial fans (Arattano and Marchi, 2008; Piton and Recking, 2014; Marchi et al., 2010).

1.1.1 Debris-flow phenomena

Among the sediment transport phenomena, debris flow is one of the most dangerous geomorphic processes affecting small mountain steep basins (Okuda et al., 1980; Pierson 1986; Jakob, 2005). These events, widespread in the eastern Italian Alps (Marchi et al., 2002; Marchi and D'Agostino, 2004) and in many parts of the word (Johnson and McCuen, 1996; Hungr et al., 1984; Takahashi, 2007), have always represented a serious natural hazard and play an important role in the evolution of headwaters. In literature, a number of classification and definition may be found (Jonson, 1970; Pierson and Costa, 1987; Coussot, 1992; Ivenson, 1997; Hungr et al., 2001; Jakob, 2005) and different terms may be used to describe these phenomena depending on the scientific background of the authors. However, the aspects in common among the different definitions lead to identifying debris flow as a type of mass movement characterized by a high concentration of solid material in water that flows like a wave with a steep front. Debris flows can be considered

a phenomenon intermediate between hyper-concentrated flows (intense bed load transport) and landslides separated from them by sharp transitions of some characteristics as celerity, deposit nature and flow type (Coussot and Meunier, 1996). Debris-flow destructiveness is due to different factors: their capability of transporting and depositing huge amounts of solid materials, their steep fronts, which may reach several meters of height and their high velocities (Arattano and Machi, 2008). The critical factors for debris-flow occurrence are rainfall events (generally during high-intensity local precipitations or, alternatively, sufficient availability of water, for example from the rapid snow melting) along steep slopes and availability of sediment to be mobilized. In particular, the sediment recharge of the channel from active erosion on hillslopes is found to be a critical factor of debris-flow magnitude and frequency (Bovis and Jakob, 1999; Marchi and D'Agostino, 2004) as channel erosion is generally the most important contribution to the debris-flow volume (Hungr et al., 1984, 2005; Remaître et al., 2005; Theule et al., 2012). Moreover, the linkages between sediment source areas on the hillslopes and channel network, along with the spatial distributions of channel storage and transport processes are, therefore, key controls of debris-flow occurrence and magnitude (Schrott et al., 2003; Schlunegger et al., 2009; Berger et al., 2011; Loye et al., 2016). Consequently, the prevention of natural hazards related to debris-flows requires a better understanding of sediment dynamic and the assessment of temporal and spatial variations of channel storage in debris-flow catchments. In channels equipped with check dams, an integrated approach that analyses the interactions of debris flows with these control works is needed to assess the efficiency of the structures and to improve the long-term hazard management at the catchment scale. However, these aspects have not often considered before taking decision and design the intervention in mountain basins.

1.1.2 Structural measures and debris-flow dynamics

The structural intervention usually built in the river beds against debris flows include debris-flow breaks, debris-flow overfall barriers, deflection dams, retention basins, debris-flow net barriers and in general different type of check dams (Hübl and Suda, 2008). Among these hydraulic engineering structures, check dams are the most effective and common technique to manage debris-flow hazard (Hübl and Fiebiger, 2005; Hübl and Suda, 2008; D'Agostino, 2013; Piton and Recking, 2017). Indeed, check dams have been a long tradition in many mountain catchments since the mid-19th century (Piton et al., 2016). No universal name exists for these structural measures against debris flow. In the literature, similar structures have been named deposition/retention/sediment retarding basins, sediment traps, open/slit/slot check dams, solid body barriers, and debris-flow breakers (Piton and Recking, 2016). In any case, these structures generally aim to retain debris in an upstream area (of course this effect stops when the storage basin is filled) and regulate solid transport by the temporary accumulation of sediment. There are

different types of check dams, in particular for debris flow, and Hübl et al. (2005) has proposed a classification of such structures that can clearly have several functions at the same time. Check dams, usually constructed in series in the transportation zone, are used to reduce steep channel slopes, minimize scour along the bottom and sides of the stream, increase bed stabilization and to retain debris. Additional functions are possible with open check dams: filtration and storage of bed-load sizing through hydraulic and mechanical control of deposit and peak flow modulation by temporarily retaining sediment. Moreover, when open check dams work together with a storage basin, the most important characteristic of these structures is the kinetic energy dissipation of a debris flow (Remaître and Malet, 2013). A large literature exists on check dams, and mainly concerns: structure stability problems (Lenzi et al., 2003; Osanai et al., 2010; Dell'Agnese et al., 2013); design (Rudolf-Miklau and Suda, 2013; Piton and Recking, 2016); functions (Suda et al., 2010; Conesa-García et al., 2007; Hassanli and Beecham, 2013). Several studies on check dams have investigated their effects on stream systems and channel morphodynamics. García-Ruiz et al. (2013) after the building of check dams observed: *i*) a sudden decrease in the coarse sediment transport, *ii*) an erosion downstream of the check dams and *iii*) a clear spatial organization of upstream sediment according to the distance from the structure. Piton and Recking (2017) highlighted that check dams changed the dynamic equilibrium of the natural erosion and deposition propagation in the streams and, in the long term, were able to temporarily store and then later released sediment by creating independent compartments depending on the distance between dams. Remaître et al. (2008) and Remaître and Malet (2013) focussed their work on the influence of check dams on bed scouring and filling processes and demonstrated that a small number of check dams located near the source area may substantially decrease the debris-flow intensity on the alluvial fans. On the other hand, to the best of our knowledge, very little researches considered the effects of check dams on sediment dynamics in debris-flow environments in broad time to improve the planning of this torrent control works. Marchi et al. (2010) evaluated the long-term effect of torrent control works on alluvial fans through historical documents, aerial photo interpretation, field observations and numerical modelling of debris flows. The study underlined the effectiveness of torrent control works in the decreasing of frequency and severity of debris flow if structures are periodically maintained. Recently, Victoriano et al. (2018) quantified erosion downstream flexible ring-net barriers along a debris-flow channel in a 7-years period and they used these data to prioritizing the maintenance and future management of the structures.

1.1.3 Debris-flow monitoring

The estimation of debris-flow magnitude and frequency, and the analysis of spatial patterns in terms of eroded and deposited volumes are fundamental to improve the sediment dynamic

understanding. These insights can be integrated into modelling approaches for a comprehensive risk management defining the control measures (Marchi and D'Agostino, 2004; Jakob, 2005). The monitoring of sediment volumes transported by debris flows, with their temporal frequency, timing, and flow characteristics (i.e., front velocity, peak discharge, volumes) can be obtained through long-term instrumental observations (e.g., ground vibration sensors, ultrasonic gauge, video cameras; Itakura et al., 2005; Arattano and Marchi, 2008; Comiti et al., 2014). Other different approaches have been proposed for the assessment of debris-flow volumes as empirical and statistical formulae (Bianco and Franzi, 2000) and geomorphological estimates based on field surveys (Hungr et al., 1984; Marchi and D'Agostino, 2004). However, these methods are often limited to the study sites where they were developed in or are subjective in their application. Nowadays a very used approach is the morphological method (Ashmore and Church, 1998) that analyses and understands the geomorphological dynamics through the repeat measurements of channel topography. Typically, these estimations were based on cross-section surveys (significant dependency to survey precision and reproducibility, and the spatial and temporal frequency of sections; Vericat et al., 2017) but now the developments in surveying techniques have brought geomorphological studies into the High-Resolution Topography (HRT) revolution (Passalacqua et al., 2015; Carrivick et al., 2016; Vericat et al., 2017). Topographic data at sub-meter resolution are increasingly becoming available and offer sufficient accuracy, precision and resolution to resolve changes of the magnitude relevant to the observed processes (Cook, 2017). Moreover, some topographic techniques allow the repetition of surveys with sufficient frequency to detect changes, therefore the debris-flow features can be analysed at an appropriately temporal scale at which surface processes operate. The use of repeated topographic surveys enables not only the characterization of debris flows in terms of their geomorphic activity (e.g. volumes eroded or deposited in a given reach), but also inferring the sediment dynamics in relation to the torrent control works at multiple temporal and spatial scales (Veyrat-Charvillon and Memier, 2006).

In the last two decades, the application of improved surveying platforms, sensors, remote sensing, data post-processing tools, and algorithms have facilitated the acquisition of such type of information. Additionally, HRT data set are also becoming available through governments and other institutions, including academics (Wulder and Coops, 2014; Tarolli et al., 2017). This data gathering revolution has greatly improved our ability and opportunities to characterize landscapes and to monitor and assess geomorphic changes. Several methods allow collecting HRT; the choice of the most appropriate survey platform must take in consideration the spatial extent and the features of the analysed area, the need for detailed and continuous survey, and the cost and flexibility of used/needed technologies (Passalacqua et al., 2015; Willi et al., 2015). Passalacqua et al. (2015) presented a review of methods to acquire HRT data. They studied the typical spatial resolution of HRT and the practical extent of the targeted reach. Instead, Willi et al. (2015)

provide a specific overview of existing field methods to analyse and quantify erosion and deposition by debris flows. Indeed, in landscapes dominated by steep inaccessible slopes and complex topography, such as those typical of most debris-flow catchments, is not always possible to apply all the technologies and specific methodologies for the multi-temporal (sometimes referred as 4D) topographic surveys must be used (Schürch et al., 2011). In rugged environments, the use of methods such as terrestrial laser scanner (TLS) is limited by access constraints (e.g. for large instruments) and the power requirements in remote areas (Westoby et al., 2012; Clapuyt et al., 2016). LiDAR (Light Detection And Ranging) technology resulted the most suitable to acquire HRT data over catchments and larger spatial scales (Cavalli and Marchi, 2008; Cavalli and Tarolli, 2011; Scheidl et al., 2008; Lopez Saez et al., 2011; Bremer and Sass, 2012; Cavalli et al., 2017), but for surveys of small extension it presents still relatively high costs and a quite low potential temporal resolution. There are still only a few studies analysing sediment dynamics in steep debris-flow catchments at multiple temporal scales using these technologies. Scheidl et al. (2008) examined a LiDAR-based method to calculate deposited and eroded volumes due to geomorphologic changes caused by debris-flow events. It is shown that the calculated volumes agree well with speditive field estimates derived from available events documentation. Berger et al. (2011) assessed the catchment-wide sediment dynamics over high temporal and spatial resolution in the Illgraben (Swiss Alps), using sequential aerial photography capable of monitoring sediment dynamics on both annual and seasonal scales. The authors highlighted that the cut-fill processes are crucial because the temporal and spatial variation of debris availability is a key parameter in the prediction of debris-flow activity. More recently, Theule et al. (2015) analysed sequences of channel scour and fill from seasonal topographic surveys of sediment transfer in a torrent in the French Alps. This study provided evidence that debris-flow scouring increases with slope and the most important contribution to the debris-flow volumes are the unconsolidated gravel deposits that were produced during bedload transport. Loye et al. (2016) studied the link between the supply of sediment and the implications in debris-flow initiation by means of seasonal TLS surveys. They underlined the fact that the monitoring of the in-storage changes within the channel, linked to the debris supply, can improve knowledge of the recharge threshold leading to debris flow activity and, therefore, on their prediction. Blasone et al. (2014) and Cavalli et al. (2017) monitored topographic changes through multi-temporal TLS and airborne LiDAR surveys in selected areas and at the catchment scale, respectively, in two debris-flow catchments in the eastern Italian Alps. These papers emphasized that the spatially-distributed assessment of erosion and deposition is critical for improving our understanding of debris-flow processes. As mentioned previously, Victoriano et al. (2018) using multi-temporal LiDAR data, evaluated how torrent control works influenced geomorphological channel evolution in a catchment of the Spanish Pyrenees.

In the last decade, the issues of costs and the need to acquire frequent 4D-surveys, needed to properly characterize geomorphic processes, have led to the use of other emerging technologies for monitoring topographic changes. The application of digital photogrammetry via Structure from Motion (SfM) and Multi-View Stereo (MVS) techniques provide a low-cost, rapid, and easy three-dimensional survey method (Fonstad et al., 2013) for acquiring HRT in a variety of environments and at multiple temporal scales (e.g., James and Robson, 2012; James and Varley, 2012; Stöcker et al., 2015; Stumpf et al., 2015; Clapuyt et al., 2017; Eltner et al., 2017; Heckmann et al., 2017; Mallalieu et al., 2017; Marteau et al., 2017; Izumida et al., 2017). The application of SfM-MVS (hereafter SfM) photogrammetry mainly requires: (*i*) a compact (non-metric) camera mounted on a platform (e.g. ground-based, Unmanned Aerial Vehicles or UAV, hand held pole), (*ii*) a network of Ground Control Points (GCPs), and (*iii*) an appropriate software to post-process the photos. The geometry of the scene, camera positions and orientation are automatically solved by the algorithm (software) that identifies matching features in a collection of overlapping digital images, while the MVS algorithms allow the generation of a high-density topography or 3D point clouds (for more details, for instance, see James and Robson, 2012; Micheletti et al., 2015b; Smith et al., 2015). Clapuyt et al. (2016) presented the accuracy of HRT for a broad range of landforms and landscapes by comparing the SfM data with other HRT methods (e.g., TLS, LiDAR, and GNSS-Global Navigation Satellite Systems). They showed that the accuracies obtained with SfM were in the same order of magnitude as those obtained with more traditional HRT methods. Its flexibility, particularly in terms of the scale or practical extent of the reach (Smith and Vericat, 2015), makes it well suited in rugged and complex terrains. They also highlighted its simplicity of use, along with being one of the reasons for its wide application. There are several papers in literature using SfM-MVS-based HRT to study: the evolution of highly erodible landscapes such as gullies and badlands (e.g., Stöcker et al., 2015; Smith and Vericat, 2015; Koci et al., 2017); fluvial morphology (e.g., Javernick et al., 2014; Marteau et al., 2017) and flood reconstruction (e.g., Smith et al., 2014); long-term changes on volcanos (e.g., James and Robson, 2012; James and Varley, 2012); glaciers (e.g., Immerzeel et al., 2014; Piermattei et al., 2015; Mallalieu et al., 2017); landslide displacement (e.g., Stumpf et al. 2015; Clapuyt et al., 2017; Eker et al., 2018); coastal recession (e.g., James and Robson, 2012; Westoby et al., 2012); submerged surfaces (e.g., Woodget et al., 2015; Dietrich, 2017) and structural geology (e.g., Bemis et al., 2014). SfM represents a "revolutionary" advance due to its easiness, resolution and extent range (Tarolli, 2014) and it has allowed increasing of the surveys frequency to temporal scales that were difficult to reach before. High-frequency monitoring has the potential to describe short-term controls on geomorphological change and a more realistic analysis of processes (e.g., Williams et al., 2018). Although SfM offers enormous opportunities, it raises problems related to the proper management of such a large amount of data. Indeed, Marteau et al. (2017) recently highlighted how a critical

part of the SfM is the development of a framework or workflow that allows data to be properly collected and analysed in accordance to the objective of the work. In the same way, despite the simplicity of this method, if not correctly applied, SfM can lead to datasets affected by large errors. James et al. (2017a) reported that point cloud densities with errors of the order of centimetres can be achieved, but important steps of acquisition and processing data must be addressed to reduce deformations and obtained accurate and repeatable data. Smith et al. (2015) highlighted that many SfM end-users are not aware of the errors associated with each user choice and, perhaps most fundamentally, with the processes actually taking place as part of their SfM workflow. Moreover, since this technique has a high level of automation, the majority of end-users consider the software as a "black-box" and they are often unaware of the accuracy and reliability of the obtained data. Micheletti et al. (2015b) highlighted that the advantage of SfM in providing a black-box tool where expert supervision is unnecessary, at the same time, may become a disadvantage because the user has much less involvement in data quality control and the origins of error in data may not be identified. This has been highlighted in different studies; Marteau et al. (2017), for instance, recently pointed out the need of a special attention to identify and filter erroneous or unwanted data in order to obtain high-quality products. In the same way, Eltner et al. (2016) stated the importance of carrying out well-established fieldwork strategies, using proper camera settings, GCPs and Control Points (CP; i.e., ground truth data) for understanding the different sources of errors. All these studies are in the line of the earlier review by Passalacqua et al. (2015) confirming the lack of guiding principles and standard analysis workflows for determining data quality and survey uncertainties in HRT. Additional to these, SfM only produces the data "back in the office", so at the time of the survey it cannot be known whether a point cloud will be successfully produced or what attributes (extent, resolution, 3D point quality) that point cloud will have (Carrivick et al. 2016). Therefore, although SfM cannot be longer considered as a future opportunity, the acquisition of HRT through SfM needs the design of appropriate workflows for survey planning, data acquisition, post-processing and uncertainty assessment. The development of this workflow is especially needed in multi-temporal surveys where the coherence among the surveys must be guaranteed and related to the extent and desired resolution.

The problems related to the comparison of 4D-surveys is not an aspect that must be considered only for SfM surveys, because in complex topography, several technologies require ad hoc workflows to post process the data and make this information comparable to each other (Schürch et al., 2011; Victoriano et al., 2018). In particular, the technology supporting LiDAR acquisition (e.g., surveying platforms, scanner, georeferencing systems and support tools) has seen major developments in the last two decades (Cavalli et al., 2008; Fonstad and Marcus, 2010; Tarolli 2014; Passalacqua et al., 2015; Torresan et al., 2018), resulting in the current availability of significant amounts of multi-temporal data that changed a lot in terms of point cloud density,

accuracy and precision over time. Therefore, data acquired at different epochs often showed several comparison problems (Carley et al., 2012; Daehne and Corsini, 2013), especially when 4D-data are not homogeneous in terms of quality. Indeed, different types of errors can be identified in each survey: positional uncertainties, classification uncertainties and surface representation uncertainties (Passalacqua et al., 2015). These observations are confirmed in the study of Lallias-Tacon et al. (2014) that highlighted how the alignment of data sets is not a simple problem of georeferencing but rather a problem of co-registration of surveys that have been correctly georeferenced using the same coordinate system.

1.1.4 Multi-temporal HRT to assess sediment dynamics

The development of methodological workflows enables the achievement of sufficient accuracy and precision in topographic data sets. This surely contributes to improve the monitoring topographic changes by exploiting multi-temporal Digital Elevation Models (DEMs) and helps to increase the temporal and spatial scales in which sediment dynamics can be studied (e.g., Brasington et al., 2012; Clapuyt et al., 2016; Cavalli et al., 2017; Vericat et al., 2017). Multi-temporal DEMs can be used to derive Difference of DEMs (i.e., DoDs) useful to quantify the debris mobilized and the time evolution of erosion and deposition patterns in catchment whose channel is equipped with torrent control works. Several methods are available for inferring spatially distributed sediment dynamics from the quantification of geomorphic change associated with erosion and deposition (e.g., Brasington et al., 2000; Lane et al., 2003; Wheaton et al., 2010; Passalacqua et al., 2015; Vericat et al., 2017). The DoDs uncertainty assessment and the sediment budget computation were a key issue for geomorphic interpretation of topographic changes, especially in steep mountain catchments (Lallias-Tacon et al., 2014; Cavalli et al., 2017; Victoriano et al., 2018). Moreover, DoDs maps and volumetric estimates can be used as benchmarks for numerical and physical modeling or simulations of debris flows in channels with check dams (Ballesteros Cánovas et al., 2016). Several recent studies confirm the relevance of improving the design of check dams, especially in debris-flow channels. Osti and Egashira (2008) proposed a method to improve the effectiveness of check dams against debris flows based on the potential storage volume of these. Piton and Recking (2014) identify key design criteria for check dams through small-scale experiments supported by field surveys (i.e., data for parameters calibration), aiming at improving their stability (e.g. toe scouring or slope adaptation). Norman and Nirula (2016) used a calibrated model that consider sediment data and debris-flow characteristics to examine the impacts of check dams on soil and water conservation. In addition, the volumes of sediment trapped after an event obtained by DoD can be used to define efficiency indicators as in the case of the study by Simoni et al. (2017). These authors used sediment volumes trapped behind check dams to derive an economic and risk indicator as a support for improving

sediment flux control and risk management. Dell'Agnese et al. (2013) proposed a damage index for check dams based on pre- and post-event field comparisons, and taking into account different structural conditions, and types and intensities of the events.

The DoD-based investigations can be enriched with information about potential sediment pathways that could be investigated through the assessment of connectivity (Heckmann and Vericat, 2018). Sediment connectivity analysis evaluates the linkages between sediment sources and downstream areas in geomorphic systems (Cavalli et al., 2013; Heckmann and Schwanghart, 2013; Wohl et al., 2018). The spatial and temporal characterization of connectivity patterns in a catchment enables the estimation of sediment contribution and transfer paths that are fundamental, especially for the controlling of debris-flow occurrence and magnitude. Schlunegger et al. (2009) demonstrated that the direct connectivity between hillslope and channelized processes in the Illgraben catchment (Switzerland) were related not only to rapid topographic modifications within the catchment, but also to sediment yields increase around 1–2 orders of magnitude larger in segments where hillslopes were connected with the channel network in respect to disconnected hillslopes. Messenzehl et al. (2014) confirmed that the rate of sediment transport, storage and reworking in sediment cascades was controlled by the strength of coupling between neighbouring storages on hillslopes and the connectivity to the stream channel. Connectivity estimation can support a better understanding of processes controlling the redistribution of water and sediments from the hillslopes to the channel network at a scale appropriate for land management practices and erosion control measures (Foerster et al., 2014). Indeed, the assessment of sediment connectivity has an important relation with hazard assessment, involving also the planning and design of structural measures at the catchment scale (Crema and Cavalli, 2018). The connectivity changes in space and time (Bracken et al., 2015), and cannel control works (e.g., check dams and barriers) can be regarded as one of major anthropogenic modifications to the landscape (Fryirs, 2013; Persichillo et al., 2018; Calsamiglia et al., 2018; Llena et al., 2019), capable of impacting on sediment spatio-temporal dynamics. The increasing availability of 4D high-resolution DEMs represents an important basis for the quantitative assessment of connectivity through geomorphometric indices (Cavalli et al., 2013; Heckmann et al., 2018). An index of connectivity (IC) allows the delineating spatial and temporal patterns of runoff and sediment pathways that govern the delivery of eroded sediments from hillslopes to the channel network, and finally to the outlet of a catchment (Heckmann et al., 2015). The estimation of the difference of IC (hereafter defined with acronym DoIC), derived from two epochs of the DEM, enables the assessment of connectivity change in time (Foerster et al., 2014; Llena et al., 2019) and the further understanding of the debris-flow dynamic. The characterization of sediment connectivity and its evolution through time provides important information about the changes in the geomorphic system structure and the involvement for the debris-flow dynamics. Indeed, the sediment pathways

derived from IC and DoIC allow inferring on structural connectivity (spatial configuration of system components; Heckmann et al., 2018), while the spatial pattern of erosion and deposition, emerged from sediment transfer of the DoD, provided important information on functional connectivity (actual transfect of sediments; Heckmann and Vericat, 2017). The understanding of connectivity in relation to the catchment morphodynamics is critical for making informed decisions in torrent management practice (Wohl et al., 2018). The synergistic use of connectivity analysis and DTM differencing may allow understanding the impact of torrent control works on sediment dynamics.

1.2 Thesis aims and outline

This thesis presents a multi-temporal analysis of sediment dynamics in a debris-flow basin (Moscardo Torrent - eastern Italian Alps) where several torrent control works were realized over the last decades. The aim of the study is to investigate the efficiency of the check dams and their role on debris-flow dynamics both at reach and catchment scale. All these geomorphometric information and analysis could be used to improve the future planning of structures or to find the best strategies to preserve the efficiency of existed torrent control works. To this end, topographic surveys were used to obtain multi-temporal DEMs which were compared (i.e., DoD) to quantify the debris mobilized and the time evolution of erosion and deposition patterns in debris-flow channels equipped with check dams. Within this context the development of specific methodological workflows to process and compare 4D-data in a rugged environment is needed and it is investigated in the present work. The analysis was focused on two spatial scales: reach and catchment. The topographic details at the fine scale were obtained through 4D-SfM surveys (10 from 2015 to 2018) in the main channel of Moscardo Torrent where two check dams were recently built. These frequent surveys enabled the continuous evolution assessment of the debris-flow dynamics with a very high level of detail. Instead, multi-temporal LiDAR surveys (2003-2009-2013) were used to quantify the debris-flow erosion and deposition patterns, and the role of check dams at the catchment scale. These data presented a lower level of detail than SfM surveys and a wide time window, but their broad spatial scale allowed the integration of DoDs data with a sediment connectivity analysis to have a whole assessment of debris-flow dynamics at the basin scale. The consistency of DoDs data was tested thought the comparison between the erosion estimate of DoDs and the volumes of debris-flow events measured through the monitoring station along the Moscardo torrent.

The thesis is organized as follow:

After an introduction on the state of art on the debris-flow phenomena, the role of torrent control works in the natural hazard and the monitoring of sediment dynamics, the second Chapter

illustrates the main features of the study area: geomorphological and geological settings, the monitoring equipment installed in the catchment, and the torrent control works realized along the Moscardo torrent. Chapters 3 and 4 represents the core of the PhD. Chapter 3 describes the specific methodological workflows realized to obtain and compare high-quality multi-temporal data in a complex environment. In particular, Chapter 3 presents a detailed workflow developed during PhD research to effectively collect and process 4D-SfM data in debris-flows channels. The workflow realized to process multi-temporal LiDAR, was specific for the Moscardo catchment where the rugged topography needed particular work methodologies. Moreover, multi-temporal LiDAR data were used to apply the connectivity index at the catchment scale. Chapter 3 also displays the method used to estimate the volumes of debris-flow events measured through the monitoring station, and describe the realization of the torrent control works inventory along the Moscardo Torrent.

Chapter 4 illustrates the application of the developed SfM workflow to a specific area of the Moscardo reach to study the effect of check dams on the debris-flows dynamics in mountain environments. Chapter 4 also presents and discusses the results of SfM and LiDAR workflows. Moreover, it illustrates the database of torrent control works, the data of recorded debris-flow events and the sediment connectivity analysis.

Chapter 5 summarizes the main conclusions from all the applications and analyses carried out in this thesis project.

Part of the material contained in this thesis is taken from the following published papers, realized and published during the PhD:

- *Cucchiaro, S., Cavalli, M., Vericat, D., Crema, S., Llena, M., Beinat, A., Marchi, L., Cazorzi, F., 2019. Geomorphic effectiveness of check dams in a debris-flow catchment using multi-temporal topographic surveys. Catena 174, 73-83.*
- *Cucchiaro, S., Cavalli, M., Vericat, D., Crema, S., Llena, M., Beinat, A., Marchi, L., Cazorzi, F., 2018. Methodological workflow for topographic changes detection in mountain catchments through 4D-Structure-from-Motion photogrammetry: application to a debris-flow active channel. Environ. Earth Sci. 77, 632.*
- *Cucchiaro, S., Maset, E., Fusiello, A., Cazorzi, F., 2018. 4D-SfM photogrammetry for monitoring sediment dynamics in a debris-flow catchment: software testing and results comparison. Int. Arch. Photogramm. Remote Sens. Spat. Inf. Sci. XLII-2, 281-288.*
- *Cucchiaro, S., Cazorzi, F., Marchi, L., Crema, S., Beinat, A., Cavalli, M., 2019. Multi-temporal analysis of sediment dynamics in a debris-flow catchment: the role of channel control works. In preparation.*

2. Study catchment: The Moscardo Torrent

The Moscardo Torrent is a small stream of the Eastern Italian Alps (Fig. 2.1), but it has been the subject of several studies on the field of geomorphology (Cavalli and Marchi 2008; Mao et al., 2009; Blasone et al., 2014; Cucchiaro et al., 2019), geology (Marcato et al., 2012), and debris-flows monitoring (Marchi et al., 2002; Arattano et al., 2012). The relatively high frequency of debris-flow occurrence (commonly one or more event per year) and the geomorphological features of the Moscardo catchment make it an important environmental for scientific researches. This catchment (Fig. 2.1; Tab. 2.1) covers an area of 4.1 km^2 and ranges from 890 m at the fan apex to 2043 m at the highest summit; the average slope is 63 %. The main channel length is about 2760 m, with an average slope of 37 % (Marchi et al., 2002). The Moscardo torrent, at less than two kilometres from the Austrian boundary, is a tributary of the But torrent that flows into the Tagliamento River. The climatic conditions are typical of the easternmost part of the Italian Alps: cold winters and mild summers with abundant precipitation throughout the year (annual average of 1660 mm with 113 rainy days per year) occurring mostly as snowfall from November to April and snowmelt-dominated runoff in May and June. Deciduous forest stands, meadows, some buildings, and a quarry deposit are present on the left side of the main channel (64% and 18% of the basin area are covered by conifer forests and shrubs, respectively). Unvegetated areas (tussock, scree and outcropping rocks), which occupy about 18% of the basin, provide most of the debris supplied to the channel network, both in the upper part of the basin and along the main channel (Mao et al., 2009).

Table 2.1: The main morphological features of Moscardo catchment.

Catchment area	Elevation ranges	Mean hillslope slope	Mean channel slope	Channel length	Mean annual precipitation
4.1 km^2	890-2043 m a.s.l.	63%	37%	2760 m	1660 mm

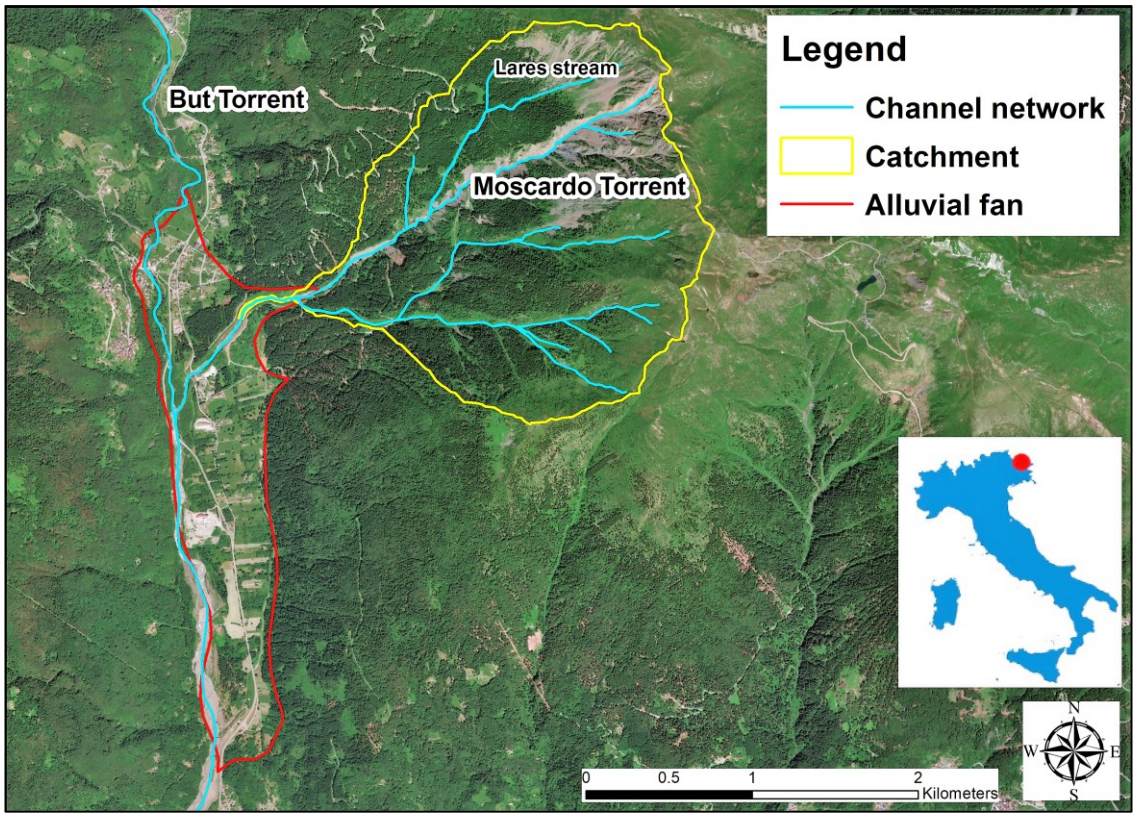

Figure 2.1: The catchment, the channel network and the alluvial fan of Moscardo torrent.

2.1 Geomorphological and geological settings

The rock masses outcropping in the basin are Carboniferous in age and consist in highly fractured and altered flysch (Fig. 2.2a), with turbiditic quartz-sandstones and gray shales, feldspar sandstones and greenish shales with volcanic explosive breccias displaying a low-grade metamorphic facies. This kind of bedrock appears to be very brittle and prone to erosion.

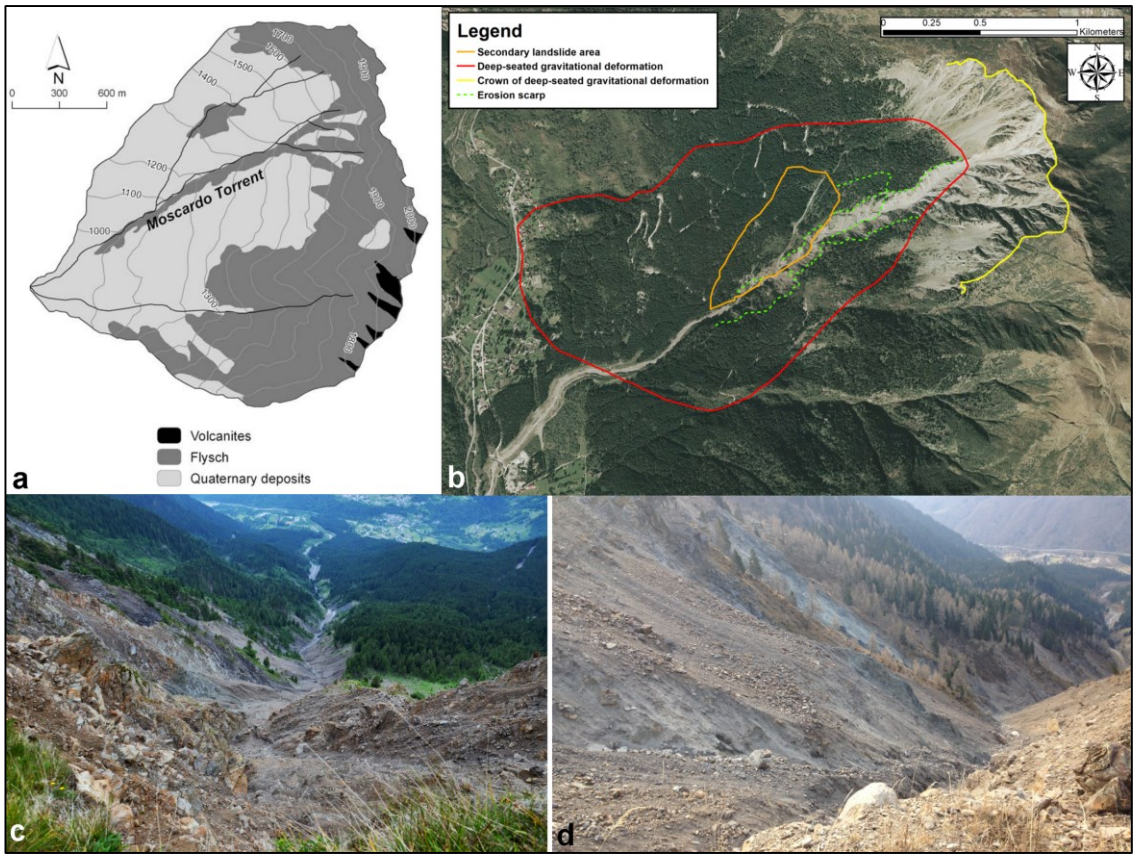

Figure 2.2: Geomorphological and geological settings of Moscardo catchment. a) Simplified geologic maps of the Moscardo Torrent from Mao et al. (2009). b) Map of the deep-seated gravitational slope deformation, the secondary landslide area, the crown of deep-seated gravitational deformation and the erosion scarp from Blasone (2014). c) The basin head characterized by widespread sediment source areas. d) The steep hillslopes of the Moscardo torrent. Cucchiaro 2017.

Nevertheless, the lithotechnical characteristics of the bedrock itself are not the only cause of the diverse slope instability phenomena observed in the area. The whole basin is involved in a large Deep-Seated Gravitational Slope Deformation (Fig. 2.2b), whose long-term evolution contributed to the progressive weakening of the rock mass properties, increasing both the magnitude and frequency of the collateral landslides phenomena, such as rockfalls and shallow landslides and debris flows, which supply large amounts of debris to the channels (Marcato et al., 2012). Therefore, quaternary deposits, mostly consisting of scree and landslide accumulations, are also common in the basin and the Moscardo torrent represents a high landslide risk site with a deep roto-translational rock slide of approximately 2 million m^3 along 2 km^2. The peculiar structural features and morphological evidence associated to deep-seated gravitational deformation are visible in the area. In particular, double crests, scarps and counter-slope scarps, slope-parallel trenches, bulging in the lower parts of the slope and also small-scale landslides, debris flows and talus slope deposits have been mapped and summarized in (Fig. 2.2b) by Marcato et al. (2012). These secondary instability phenomena cause quasi-unlimited amounts of

sediment availability, resulting in frequent debris flow events, triggered also by relatively moderate rainstorms. The initiation area of debris flows is located in the upper part of the basin and along the main channel where there are widespread sediment source areas (Fig. 2.2c and d). Initiation points can vary from event to event, generally being located at the head of the main channel; typical gradients in the initiation area are of 20°–30° for the main channel and of 30°–50° for channel banks and hillslopes. The source material consists of scree deriving from the weathering and wasting of rocks (Marchi et al., 2002).

Debris flows in the Moscardo torrent take place usually in the summer months, owing to the forcing of high-intensity storms and to the availability of sediment recharging the channels during the winter and spring months. The debris-flow deposits are poorly sorted and show a wide grain size distribution. Lateral levees and debris-flow lobes mostly consist of pebbles and medium to fine boulders supported in a muddy matrix; larger boulders with an intermediate diameter of 2–3 m are also common. The particle size distribution of debris-flow deposits shows D50 ranging approximately from 10 to 20 mm and D84 from 500 to 700 mm (Mao et al., 2009).

The Moscardo Torrent has formed a large asymmetrical fan that spreads across the valley floor, forcing the main stream (But Torrent) to the toe of the opposite valley slope (Fig. 2.1). The fan extends southward for approximately 2.7 km and covers an area of 1.27 km^2. At present, the active fan is limited to a narrow area along the main channel. Woody vegetation covers the mid-fan area in the proximity of the channel, especially on the right side where a dense coniferous stand is present. More houses are located in the northern part of the fan and a national road passes through the southern, no-longer active, portion of the fan (Cavalli and Marchi, 2008).

2.2 Monitoring of debris-flow events

Since 1989, debris flows have been monitored in the Moscardo catchment (Marchi et al., 2002). The monitoring equipment installed along the torrent has changed during the years and there were some data gaps due to the implementation of control works at the monitoring site, which caused interruption of debris flow monitoring in 1998-2000, and to malfunctioning and obsolescence of the installed instrumentation (2008-2010). Even in these periods, however, field observations permitted detecting the occurrence of debris flows and evaluating, although often with coarse approximation, their magnitude. Details regarding the monitoring system and the different types of instrumentation over time have already been presented in Arattano et al. (1997), Arattano et al. (2012), Marchi et al. (2002), Blasone (2014) and Blasone et al. (2014). Nowadays, the installed instrumentation consists of a couple of ultrasonic sensors placed at a distance of 76 m over the channel bed to measure the flow stage, a high-resolution IR (Infrared) and visible video camera (Fig. 2.3a). Three rain gauges (Fig. 2.3b, c and d) record rainfall in the upper, middle and lower

part of the basin (Fig. 2.4). Two more raingauges that belong to the regional monitoring network of Friuli Venezia Giulia Region (Omnia, 2018) are installed in neighbouring areas (Fig. 2.4). The raingauges are located respectively at 810 m a.s.l. (identification code C202; Fig. 2.4) and 1520 m a.s.l. (identification code C207; Fig. 2.4).

Figure 2.3: Installed instrumentation in the Moscardo catchment (Fig. 2.4). a) Ultrasonic sensors placed over the riverbed, and high-resolution IR (Infrared) and visible video camera. b) Raingauge installed in the upper part of the Moscardo catchment. c) Raingauge installed in the middle part of the Moscardo catchment. d) Raingauges installed above the monitoring station in the lower part of the Moscardo catchment.

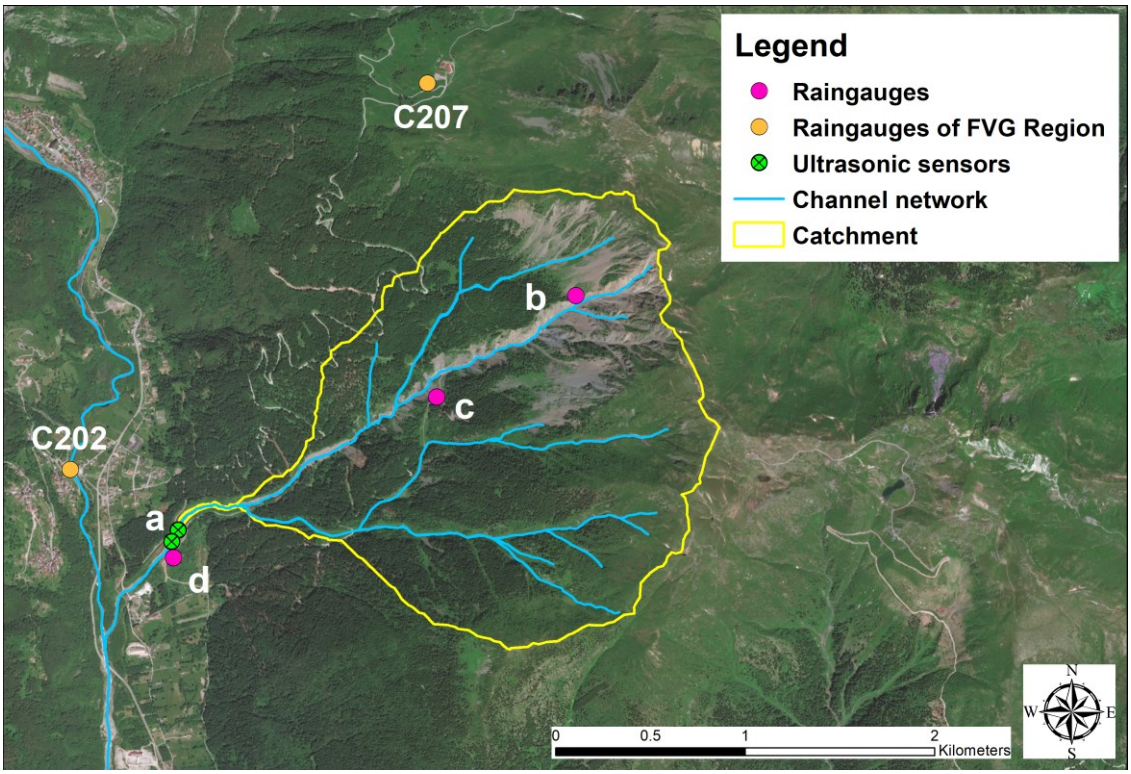

Figure 2.4: The monitoring network (raingauges and ultrasonic sensors) of the Moscardo catchment. The case letters (a, b, c, d) identify the monitoring systems in Figure 2.3, while the raingauges of FVG Region where identified with own code.

2.3 Torrent control works in the catchment

The debris-flows events of Moscardo torrent have created concerns for infrastructures located on the alluvial fan and near the confluence (Fig. 2.1) because the amount of debris could create a temporal barrier that could stop the flow of the receiving stream (But Torrent – e.g., Fig. 2.5) as it happened in the past. This could be very dangerous for the exposed elements downstream.

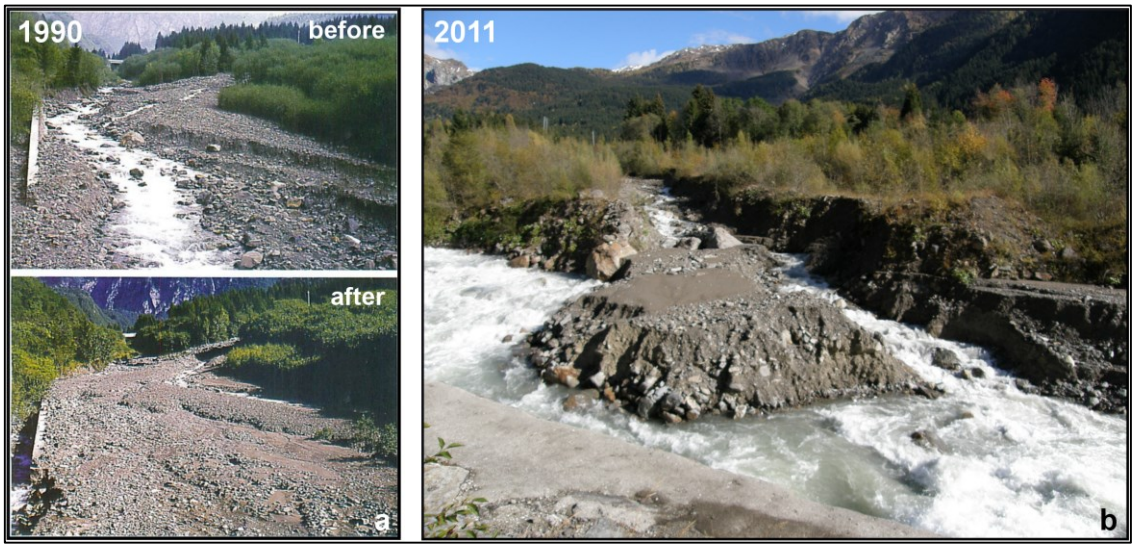

Figure 2.5: Sediment deposits at the confluence of But Torrent after the Moscardo debris-flow events. a) The confluence area before and after the debris-flow of July 1990 (Arattano et al., 1996). b) Confluence area after the debris-flow of 14 September 2011 (Blasone, 2014). Blasone 2011.

For the debris-flow hazard mitigation, over the last decades (since the 1970s), several torrent control works have been built in the main channel to limit bed erosion, to reduce channel slope and to stabilize channel banks and slopes in the middle and lower reaches (Marchi et al., 2002). The main purpose of control works was to avoid the transport of a large amount of sediment could arrive at the confluence of the But Torrent (Fig. 2.5). Different interventions were designed both on the main channel, on the tributary streams and along the hillslopes (Kravina, 1974; Puntel, 1993) to mitigate debris-flow hazards. In particular, bioengineering interventions (double-row palisades, brushes and palisade constructions, brush and fascine sills; Fig. 2.6a), riverbanks stabilization (Fig. 2.6b), protection forest rehabilitation, and drainage systems had been realized to stabilize some slopes and landslides in the time into the Moscardo catchment. However, the most used solution over time was the building of several reinforced concrete check dams (Fig. 2.6c), sills and canalizations of the Moscardo tributaries (as the Rio Lares stream; Fig. 2.6d and e).

Figure 2.6: Torrent control works over time in the Moscardo catchment. a) Bioengineering interventions built in 2014 to stabilize a slope in the upper part of the Moscardo catchment. Cucchiaro 2014. b) Riverbanks stabilization in the lower part of the catchment close to the monitoring station in 2011. Blasone 2012. c) Example of reinforced check dams built in the 1980s along the main channel of the Moscardo torrent. Cucchiaro 2018. d) Sequence of wood and boulder check dams to stabilize the slope and channelize Rio Lares stream (Fig. 2.1). Blasone 2011. e) Canalization of Rio Lares stream after debris-flow events in 2012. The structure was built in the 1980s. Blasone 2012.

3. Methods

3.1 Measurement and estimation of debris-flow events

The ultrasonic sensors installed in the lower part of the Moscardo torrent (Fig. 2.4) measured the flow stage with an interval of 1 second, making it possible to record debris-flow hydrographs. The hydrograph analysis allowed the computation of debris-flow front velocity, peak discharge and the total volume of the surge. The discharged volumes (water and solid particles) were calculated using flow stage measurements, the cross-section area of the monitored zone and the mean flow velocity. In the same case, the mean debris-flow velocity was calculated by means of a cross-correlation technique (Arattano and Marchi, 2005) that enable to determine the mean time lag between the recording of the two sets of data of the same event at cross sections. In other cases, the mean debris-flow velocity between two cross-sections was computed as the ratio of their distance to the time elapsed between the passage of the debris flow at the gauging sites (Arattano et al., 2012). More details regarding these methods can be found in Marchi et al. (2002) and Blasone et al. (2014) where the debris flow volumes were estimated as (Eq. 1):

$$Vol = \int_{t_0}^{t_f} vA(t)dt \qquad [1]$$

Vol is the volume of flowing mass, *v* is the mean flow velocity (which is often assumed equal to the mean front velocity), *A(t)* is the cross-section area occupied by the flow at the time *t* and is known from topographic surveys, t_0 is the time of arrival of the surge at the gauging site, and t_f is the time at the end of the debris-flow wave.

As highlighted in Section 2.2, there were data gaps in debris-flow monitoring and no volume data were available, therefore the volume was estimated according to the following criteria:

- The median value of the measured debris-flow volumes (15936 m^3) in the whole monitoring period (1990-2018) was used as the total volume threshold to define two classes of magnitude for recorded debris flows. The debris flows below the median were ascribed to the "small event" class (S), while the debris flow above the median belong to the "large event" class (L);
- The debris flows for which no measurements of volume were available were ascribed to one of the two classes of intensity based on post-event field observations (flow depth, thickness and extent of the deposits);
- The average volume of each class (4273 m^3 and 39797 m^3 for S and L classes, respectively) was attributed to the debris flows for which no measurements of volume were available;

- Following the approach by Blasone et al. (2014), uncertainty bounds were computed for debris-flow volumes. Relative errors of 14% are ascribed to recorded debris flows, whereas for the volumes estimated based on the magnitude class we adopted a cautionary relative error of 50%.

This procedure is affected by major uncertainties, but it permits getting an approximate estimate of sediment output from the catchment (and outlining its variability) in the considered time span. In addition, it is well known that the analysis of rainfall data can provide important information to study the role of rainfall in triggering of debris flow especially in alpine basins (Deganutti et al., 2000; Marchi et al., 2009; Borga et al., 2014; Destro et al., 2017). This aspect was not the object of the present thesis and thus it was not analysed in detail. In any case, the rainfall data recorded by raingauges network (Fig. 2.4) during 1990-2018 time span were used to identify the number of event per year that could be considered significant to trigger debris flows in the Moscardo basin. The significant thresholds for the debris-flow triggering were identified taking in account the previous studies that compared debris-flow events and rainfalls in the Moscardo catchment (Deganutti et al., 2000; Marchi et al., 2002; Arattano et al., 2012; Blasone, 2014). In particular, they assessed several storm variables including total storm rainfall, average intensity, maximum 60-min intensity and antecedent precipitation. However, only total storm rainfall and maximum 60-min intensity were significantly different between debris-flow storms and storms that did not trigger debris flows (Marchi et al., 2002). They identified how potential rainfall event capable of triggering debris flows, those exceeding 20 mm of rain cumulative until the time of reaching the maximum intensity referred to the hour and whose hourly intensity was more than 10 mm h^{-1} (Blasone, 2014). Therefore, this finding allowed the identification of the number of event per year that could be considered significant. The assessment considered different raingauges of the network because anyone of these covered the whole period 1990-2018 alone. The rainfall data were analysed for the May-October window for each year because in this period were usually recorded debris-flow events in the Moscardo catchment. In this way, it was possible to have a general view of the rainfall pattern trend in the monitoring period.

3.2 SfM photogrammetry: workflow for monitoring geomorphic changes in mountain torrents

The effect of check dams on the sediment dynamics of the Moscardo Torrent at channel scale was investigated with multi-temporal topographic surveys obtained by means of SfM photogrammetry. As mentioned before, the acquisition of high-resolution topography through SfM needs the design of appropriate workflows for data acquisition and post-processing, and uncertainty assessment,

especially in steep and rugged mountain slopes like the Moscardo study area (Cucchiaro et al., 2018a). Therefore, a comprehensive workflow (Fig. 3.1) was designed to provide a series of guidelines to monitor geomorphic changes in mountain torrents through 4D-SfM. In the following sections on the different procedural steps of the workflow are described: (*i*) data acquisition (A and B in Fig. 3.1), (*ii*) data processing (C to G in Fig. 3.1), (*iii*) data and error analysis, and DEM generation (H to J in Fig. 3.1), (*iv*) the assessment of topographic changes through DEM differencing (DoD; K to L in Fig. 3.1).

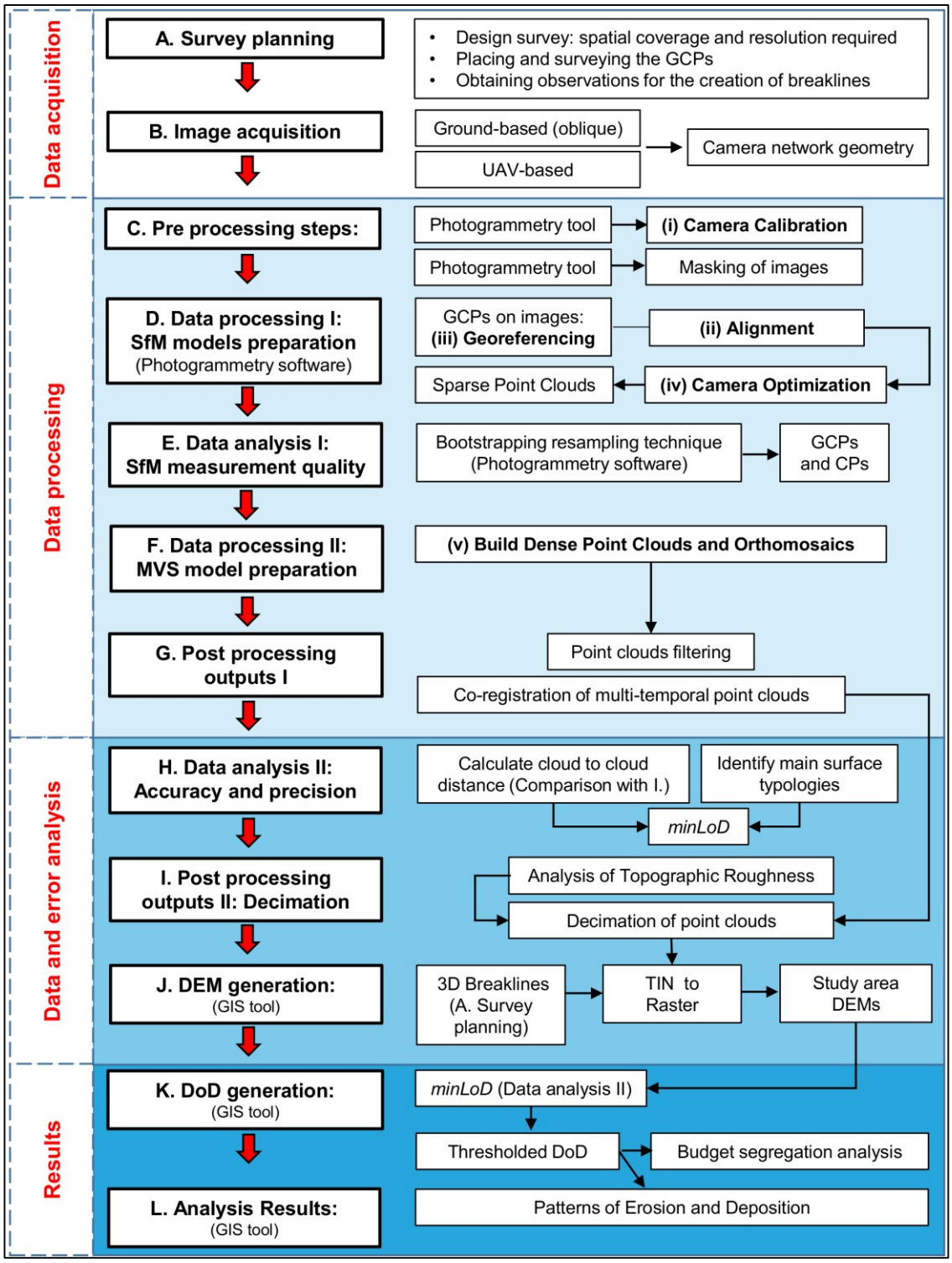

Figure 3.1: SfM general workflow chart, composed of twelve main interrelated sections (see text for more details).

3.2.1 Survey planning

One of the main strength of the SfM technique is its flexibility in the type, number, scale and positioning of input images that can be handled. However, the user has to weigh up a number of factors in making these choices: cost, accessibility, and research purpose (i.e., resolution and

spatial extent). Therefore, mission planning is a key aspect, especially to survey complex and inaccessible environments. Before going to the field it is important the choice of the image acquisition platform. A wide range of options is available, from ground-based platforms such as hand-held poles, to airborne solutions as the UAVs. In general, the platform has to consider a series of trade-offs, all of them based on the features of the surveyed area: pixel resolution, spatial coverage, image quality, and cost-effectiveness (Smith et al., 2015). An integrated approach combining ground-based and aerial images can help to overcome individual disadvantages (e.g., ground-based images are not able to guarantee areal coverage, while aerial photos may show a poor representation of vertical surfaces, being influenced by the vegetation). This approach also benefits from the acquisition of data from two different observation directions (i.e., the nadir for UAV images and oblique for terrestrial images; Stöcker et al., 2015). When accessibility is limited such as in many mountain environments, the choice of the appropriate UAV is a key aspect to analyse (Carrivick et al., 2016). UAVs present different features in terms of efficiency (energy wise – flight time), range (will determine the coverage), flexibility and operational requirements (most of them related to weather conditions), and space for take-off and landing (which may not be available in remote and rugged terrains). In general, the UAV must be suitable to survey the whole study area maximising the coverage and the overlap between the pictures, ensuring a sufficiently large image footprint. Additionally, special attention is required in terms of the flight legislation for UAVs in the country where the survey will be carried out. This will determine the permissions required before flying. To carry out the data-fusion between aerial and ground photos, it is important to use the same camera with the same focal length to minimize the integration problems in the photogrammetric models. In general, the choice of the sensor, the flight height, and the focal length are fundamental aspects to be considered (O'Connor et al., 2017). Another important aspect while planning the survey is the overlap between images that are relevant to find homologous points within several images (Eltner et al., 2016). If the UAV includes a flight control unit (coupled to a GNSS), it is possible to plan the UAV flight strips by a software that accordingly adjusts the height and speed of flight, and the image overlap (optimal overlap is 80% in flight direction and a flight strip overlap of 60%). However, the GNSS signal could be sometimes low in remote mountain areas, limiting automatic flight missions. An additional aspect to consider when the sampling design is planned is the number, location, and distribution of the Ground Control Points (GCPs; Section A in Fig. 3.1), based on the features of the studied area, extension, and desired resolution. The GCPs are used for scaling and georeferencing the SfM-based point clouds, and are fundamental for the accuracy and repeatability of the survey (James et al., 2017a). They should be located in stable areas for all the multi-temporal surveys, and uniformly distributed, not aligned or clustered (Piermattei et al., 2015), and not neglecting the margins. GCPs should be distributed also at the edge or outside the study reach (James and Robson, 2012)

to enclose the area of interest, because if the study area is extended outside the GCP area, a significant increase in error may be observed in that region (Eltner et al., 2016). To survey the coordinates of GCPs, the use of survey grade GNSS techniques should be planned whenever possible, while the use of classical surveying instruments like total stations might be advantageous for small size surveys (using a local coordinate system), or even necessary in case of poor satellite constellation geometry or missing GNSS signals due to large sky occlusions. The survey time can be chosen according to the best satellite constellation geometry. Among the GNSS techniques, RTK (Real-Time Kinematic)-GNSS (eventually NRTK-Network Real Time Kinematic- where these services are available) has the advantage to provide the user with the GCP coordinates and their expected accuracy in real time, minimizing, the surveying and post-processing time. As an alternative, the conventional Post-Processed Stop&Go Kinematic approach (i.e., the rover must first be initialized, once enough data is collected to resolve the ambiguities, the user can move the receiver) can be used. However, this approach requires further post-processing corrections in the lab using RINEX (Receiver Independent Exchange Format) data from nearby Reference Stations that can furnish full measurement control and a fairly better accuracy respect to real-time techniques. High-quality 3D coordinates of these GCP points should be preferable to improve the quality of the final point clouds (James and Robson, 2012).

3.2.2 Data acquisition

A number of factors have to be taken into account carefully before carrying out the field survey campaigns: landforms, surface reflectivity (e.g., water), illumination conditions, change in shadow length, colour and texture of the interested object (Bemis et al., 2014). If possible, the image should be acquired in constant and diffuse illumination condition, realizing an optimal camera network geometry, paying attention to minimising (moving) shadows, and ensuring the visibility of the targets in the photos that will be required later in the post-process such as GCPs. SfM survey is critical, as has been already highlighted in recent works (e.g., Bemis et al., 2014; Carrivick et al., 2016), because there are several parameters that affect the quality of the 3D point cloud and reduce key point matching that is a function on image characteristics (Gruen, 2012; Stöcker et al., 2015; Eltner et al., 2016; Mallalieu et al., 2017; Mosbrucker et al., 2017; O'Connor et al., 2017). Therefore, the camera configuration must be set considering the field conditions (Mosbrucker et al., 2017; O'Connor et al., 2017). It is important to set some key parameters of the camera like focus and exposure. The latter is a function of the lens aperture, shutter speed, and ISO sensitivity. For non-stationary camera platforms, like UAVs, it is suggested to set the exposure mode to shutter priority and select a shutter speed <1/400 s. Keep ISO sensitivity as low as possible (≤ 400) while maintaining acceptable shutter speed and aperture values (Mosbrucker et al., 2017). Several studies highlight how a prime lens (fixed focal length lens) provides superior

accuracy, precision, and stability (Shortis et al., 2006; Micheletti et al., 2015b; Mosbrucker et al., 2017). This result pairs with the common assumption in photography that a prime lens is better than a zoom lens because it does not have moving parts; it is simpler and best optimized for its specific focal length.

The image network geometry is another fundamental aspect because the capture of photographs from a limited number of poorly distributed locations (stations) can lead to model distortions (Bemis et al., 2014). In terms of coverage, every surface that will be reconstructed needs to be covered by at least three images taken from different positions, and preferably more. A high image overlap is relevant to finding homologous points within many images that cover the entire image space when combining ground-based and UAV photos (Section B in Fig. 3.1). While the mission flight software could set the UAV image overlap, for the ground-based photos it is important to acquired convergent images (high angle of convergence) at multiple object distances, with ≥ 80% frame overlap to improve the whole image network geometry (Eltner et al., 2016; Mosbrucker et al., 2017).

Before image acquisition, the GCPs should be distributed throughout the study area and their centroids surveyed (Section A in Fig. 3.1). It is important to control that GCPs could be visible in as many images as possible and easily distinguishable from the surrounding landscape (Smith et al., 2015). The same GCPs can be used for multiple surveys (i.e., fixed control network) if possible and, if this is the case, is highly recommended re-surveyed these frequently to make sure not move to guarantee the multi-temporal comparison. Moreover, in order to improve the quality of the DEMs, the edges of torrent control works structures could be also surveyed with the same Total Station or GNSS system; these observations could be used to create breaklines (Section A in Fig. 3.1) to be added in the process of DEMs generation (Section J in Fig. 3.1).

3.2.3 Data post-processing

Image processing

Various software permit processing the images to extract SfM-based HRT (Cucchiaro et al., 2018b). Here Agisoft Photoscan Pro v 1.2.0 (Manual Agisoft Lens, 2010), a commonly used software (e.g., Javernick et al., 2014; Piermattei et al., 2015; Smith and Vericat, 2015; Woodget et al., 2015; Marteau et al., 2017) has been chosen. Agisoft Photoscan (hereafter Photoscan) combines SfM and MVS to extract the 3D point clouds of the scene and, additionally, orthomosaics. The software is highly automated, and it offers few means of user-control, which are limited to some pre-processing steps, like the manual masking of moving or unwanted objects (e.g., water, vegetation and clouds in ground-based images; Section C in Fig. 3.1) that decrease the image matching but may reduce errors (Piermattei et al., 2016). Therefore, several masks can be created in Photoscan to cover unwanted objects in the photos uploaded in the software.

A total of five main steps are required:

(i) Camera calibration. The camera calibration step allows the determination the intrinsic geometry and distortion model of the camera. There are two common approaches: pre-calibration and self-calibration. The camera can be first pre-calibrated using Agisoft Lens, an automatic lens calibration routine included in Agisoft Photoscan Pro v 1.2.0 (Section C in Fig. 3.1) which uses LCD screen as a calibration target and supports estimation of the full camera calibration matrix, including non-linear distortion coefficients (Manual Agisoft Lens, 2010). If the lens is not calibrated, the software also allows establishing an automatic calibration (based on the sensor pixel size and focal length derived from image EXIF details) of the parameters during the optimization process (see next *iv* step). Pre-calibration should be preferred to software self-calibration for resolving ambiguities that cannot be determined between feature scale and distance, which can produce errors in the interior camera parameters (Piermattei et al., 2016). Previous studies (e.g., James and Robson, 2014; Carbonneau and Dietrich, 2017) highlighted how a central doming effect was presented in UAV-SfM surveys when self-calibration was used and this problem seems to be reduced when pre-calibrated parameters were employed. Moreover, the research results of Griffiths and Burningham (2018) suggests that when only single-scale nadir imagery (common in UAVs surveys) was available, pre-calibration of the camera model was more effective at mitigating systematic distortion than self-calibration. Then, the estimated camera parameters can be used in the next process.

(ii) Alignment. This process includes the following steps: identification and matching of common features in the set of images, estimation of internal camera parameters and relative orientation of the camera at the time of image acquisition, and construction of the image network (Carrivick et al., 2016; Eltner et al., 2016; Piermattei et al., 2016). A first image alignment (Section D in Fig. 3.1) should be performed to determine the photos that the software does not align for different reasons, and to delete unwanted or outliers data (i.e., points that are clearly located off the surface or have anomalous large image residuals). It is important to underline that the terrestrial and aerial photos can be aligned together when the same camera and setting are maintained, although they are usually processed separately and merged after post-processing (e.g., Stöcker et al., 2015).

(iii) Scaling and georeferencing. This step allows the scaling and georeferencing of the 3D point cloud using a seven-parameter linear similarity transformation based on XYZ coordinates of GCPs (Smith et al., 2015). Therefore, the GCPs have to be located and manually marked on at least two photographs, then the software predicts their locations in the model (Section D in Fig. 3.1), and this could be used to evaluate the success of the photograph alignment process (Cook, 2017). Moreover, this helps to georeference the sparse point cloud, to remove deformations such as the "dome effect" (James and Robson, 2014), and to refine the camera calibration parameters if necessary (Fonstad et al., 2013; Eltner et al., 2016). James et al. (2017a) highlighted how the

incorporation of control data within the image processing was a fundamental part; therefore, it is necessary to evaluate the level of GCPs uncertainty before to include these data to avoid adversely affecting data accuracy. Now several SfM-based applications allow control measurements to be included in the processing, therefore there is a more convergence between the traditional photogrammetric workflows and computer vision communities (James and Robson, 2014; Smith et al., 2015; James et al., 2017a; Mosbrucker et al., 2017). A second alignment that includes also the GCP information can be performed to improve the first alignment with a better location of the match points and the relative orientation of camera positions parameters of each image (Javernick et al., 2014; Woodget et al., 2015; James et al., 2017a). With this external information included in the algorithm, the alignment can be re-run to improve the image alignment in light of this information (Smith et al., 2015; Carrivick et al., 2016). In some occasions, an iterative process of photographs aligning may be required: i.e., marking markers or tie points (homologous points that link different images), checking photograph alignment based on predicted tie point locations, marking additional tie points, and re-aligning the photographs (Cook, 2017).

(iv) Camera optimization. The "optimization" process (Section D in Fig. 3.1) in Photoscan refines the camera position and reduces non-linear project deformations by incorporating control data (James et al., 2017a). In particular, the location of the tie points, the camera positions and the camera calibration parameters of each image are automatically and simultaneously estimated with a bundle adjustment algorithm that improves and refines their values during the camera alignment (Piermattei et al., 2016). 3D points are adjusted to minimise the sum of the re-projection and georeferencing error through a least-squares network optimisation (Granshaw, 1980). Moreover, this process allows a further optimization by removing obvious outliers and incorrect matches from the sparse point cloud. This optimization can improve the survey accuracy by an order of magnitude (Javernick et al., 2014), as can be observed looking at the reprojection error expressed in pixels and in meters by the software (Piermattei et al., 2015; Section D in Fig. 3.1). This error could be a preliminary indication of the quality of the point cloud (Eltner et al., 2016).

(v) Extraction of high-density 3D point clouds and orthomosaics. This final step (Section F in Fig. 3.1) involves the implementation of MVS image matching algorithms that operate at the individual pixel scale to build dense clouds (Piermattei et al., 2015) that increase the point density by several orders of magnitude (Woodget et al., 2015). Then the point clouds may need to be cleaned manually by removing stray and belowground level points in regions where points are poorly correlated and have high errors, primarily within the wet areas (see next Section 3.2.4). Additionally, in this final process, orthomosaics can be also exported, being their resolution in agreement with the point cloud density and the resolution of the photos.

Point cloud Post-Processing

Several processing operations may be applied once the point clouds are obtained and before the creation of DEMs (Passalacqua et al., 2015). In this workflow, a preliminary editing is performed by means of the CloudCompare software (Omnia Version: 2.9.1; http://www.danielgm.net) through a manual filtering, and then using the "SOR filter tool". This filter is used to remove outliers (Section G in Fig. 3.1) through the computation of the average distance of each point to its neighbours, and then it rejects the points that are farther than the average distance plus a defined number of times the standard deviation. Additionally, the Iterative Closest Point (ICP) algorithm can be used to automatically co-register point clouds. It iteratively revises a transformation solution (using a roto-translation matrix that included rotational parameters, translation parameters, and a scale parameter) in order to minimize the spatial difference between two point clouds (Zhang, 1992) and to fit a compared point cloud to a reference one. The co-registration can be performed with the aim of improving the quality of the multi-temporal clouds considering the accuracy of the GNSS measures, especially in the elevation component (GCPs were re-surveyed every time since some of them could have moved). The ICP can be also used to check the manual identification of markers in the images, which could produce inaccurate georeferencing and could lead to an unreal shift or rotation between 3D models. Therefore, the combined use of ICP and GCPs allows a "double registration process" to increase the quality of the point clouds. Moreover, Williams et al. (2018) affirmed that the accuracy of alignment is one of the key sources of error when detecting change between two point clouds, while Carrivick et al. (2016) confirmed that ICP reduces overall SfM errors. Eltner et al. (2016) stated that ICP algorithm can improve the accuracy significantly if a systematic linear error (e.g., shifts, tilts or scale variations) is given. ICP has previously been used (James and Robson, 2012) to optimize a roto-translation matrix to fit a compared point cloud to a reference one. The ICP should be used on a subset of the point clouds located in stable areas, where no change occurred between the SfM acquisitions, and then the obtained rigid transformation (matrix) should be applied to the whole-original point clouds to remove every possible not real change between the final multi-temporal 3D clouds (Passalacqua et al., 2015; Loye et al., 2016).

Furthermore, the point cloud may need to be decimated in order to reduce the processing constraints and the extremely high density of 3D clouds. In the particular case of this study, the geostatistical Topography Point Cloud Analysis Toolkit (ToPCAT) implemented in the Geomorphic Change Detection software for ArcGIS, (Wheaton et al., 2010; available in http://gcd6help.joewheaton.org/) is used. This tool has been successfully used in several studies working with 3D point clouds (e.g., Brasington et al., 2012; Vericat et al., 2014; Smith and Vericat, 2015; Javernick et al., 2014; Marteau et al., 2017). ToPCAT allows an intelligent decimation by decomposing the point cloud into a set of non-overlapping grid-cells (the size is defined by the

user) and calculate statistics for the observations in each grid (e.g., minimum, mean, maximum elevation). Following the work by Brasington et al. (2012), the minimum elevation within each grid cell is considered the ground elevation. Even so, as in Brasington et al. (2012), a preliminary analysis of surface roughness (Section I in Fig. 3.1) can be carried out to assess the role of the size of the grid-cells used for data decimation, and the definition of optimum grid cell size. Roughness is considered a 3-D measure of the topographic complexity and the analysis of the changes on this parameter as the grid size of the cells is increased gives relevant information in terms of losing topographic complexity as cell size increases. The roughness, computed in this case as the ratio between the surface area and the planimetric area, can be calculated using the DEM Surface Tools for ArcGIS (Jenness, 2013).

3.2.4 Error analysis

Data Precision and Accuracy

The quality of the obtained 3D point clouds should be always assessed because photogrammetric factors and processing settings can affect DEM accuracy and repeatability (James et al., 2017a). Two analyses are presented in the workflow (Sections E and H in Fig. 3.1). First, following Marteau et al. (2017), a bootstrapping resampling technique to randomly select 1/3 of the GCPs and use them as CP (Section E in Fig. 3.1), is applied. These CPs are not used by Photoscan to georectify the data (i.e., georeferencing) but are used to provide an independent measure of accuracy (the difference between the real coordinates in this point and the modelled values; i.e., residuals). This random selection is done 1000 times iteratively and, consequently, after all iterations during which the alignment optimisation is reset, the accuracy and precision of each point when used as GCP or CP, is obtained. This exercise proves also an opportunity to check for potentially biased points. Additionally, the mean of the residuals provides an indication of the accuracy of the registration process and the point cloud, when the GCPs and CPs residuals are used respectively, while the standard deviation of the residuals yields an indication of the precision (Section E in Fig. 3.1). A second aspect taken into account for an error assessment is the comparison of the multi-temporal point clouds in wide stable surfaces where there should have been no topographic change (bedrock outcrops or torrent control structures) and, consequently, the point clouds should be the same over time. The M3C2 (Multiscale Model to Model Cloud Comparison) tool of CloudCompare (Omnia Version: 2.9.1; see more details above), which allows the calculation of the cloud-to-cloud distance in stable zones of the study area (Section H in Fig. 3.1), is used. The M3C2 algorithm finds the best-fitting normal direction for each point, and then calculates the distance between the two point clouds along a cylinder of a given radius projected in the direction of the normal (Lague et al., 2013). The standard deviation

of the distance between point clouds is used as an indication of the measurement precision, while the absolute mean of distance can be considered as the accuracy of the point clouds.

Multiple Error Assessment and minimum Level of Detection

The point cloud obtained from each photogrammetric survey could be heterogeneous in terms of point density, accuracy and precision due to the different circumstances and environments when the photos are taken. For example, especially in mountain environments, the shadowed areas are variable as well as the areas under the water. These differences must be considered and a multiple error assessment of vertical component, based on different surface typologies, can be assessed if necessary. This type of assessment has been used previously in other studies. For instance, Lane and Chandler (2003) assessed differences in terms of uncertainty values on the basis of whether the surface was wet or dry. In particular, three main typologies are often identified in the point clouds of river environments: "Data" "No Data" and "Water" (and even "Vegetation" which has been long recognized as a source of error in photogrammetry; Cook, 2017). The "Data" typology includes areas of the cloud where the point density is high while the "No Data" typology involve zones where the point density is too low or there are shadows or holes in the point cloud that may produce relatively high errors (Eltner et al., 2016). Finally, the "Water" typology encompasses the wet areas where the water surface produces high errors due to refraction. A vertical error or elevation uncertainty (δz) for each surface typology could be attributed if it is possible to identify the different typologies in the SfM point clouds. The precision results obtained following all analyses presented in "Data Precision and Accuracy" Step could be used for the "Data" typology. For "No data" areas (if present), an error value similar to the maximum variability in elevation attributed to the micro-topography can be used when these are relatively small in extension. Such error value can be estimated, considering the size of the largest particle in the channel. Finally, for the "Water" typology the error could be evaluated through the estimate of the mean water depth when the survey is carried out, or by considering a theoretical refraction coefficient (Section H in Fig. 3.1). Even so, submerged topography may require a special treatment to correct the effects of refraction to reduce errors in such areas when the extension covered by the water is significant such as depth (see for instance the methods by Woodget et al., 2015 and Dietrich, 2017). In summary, these errors can be computed for each DEM and can be propagated when two DEMs are compared (see Section 3.2.6). A minimum Level of Detection (*minLoD*) can then be calculated as described by, for instance, Brasington et al. (2000); Lane et al. (2003); Wheaton et al. (2010); Carley et al. (2012); Vericat et al. (2017); Cavalli et al. (2017); Marteau et al. (2017). This *minLoD* allows distinguishing what is considered as real topographic change and what could be inherent noise (as per Brasington et al., 2003). The *minLoD* is computed based on the elevation uncertainty estimates of each DEM and the Confidence Interval (CI)

considered. For topographically complex environments, a spatially distributed approach is recommended (e.g., Wheaton et al., 2010; Milan et al., 2011) to propagate the errors and identify the *minLoD* for detecting high magnitude geomorphic changes. This involves calculation of the spatial distribution of Student's *t*-scores (Lane et al., 2003; Eq. 2):

$$t = \frac{|z_{new} - z_{old}|}{\sqrt{\left(\delta z_{new_i}\right)^2 + \left(\delta z_{old_i}\right)^2}} \qquad [2]$$

where $\delta z_{new\text{-}i}$ and $\delta z_{old\text{-}i}$ are the elevation uncertainty of a given pixel (i) for two DEMs (the most recent and the oldest DEM respectively), considering that each pixel i is attributed to different surface typology; t is the critical t value for a given confidence interval (1.28 for 80% CI, 1.96 for 95% CI); and z_{new} and z_{old} are the elevations in a given cell of DEMs. The change observed in each cell is estimated to be uncertain or not, based on the chosen minimum threshold of t-score in the DoDs. This statistical *minLoD* can be calculated as (Brasington et al., 2003; Eq. 3):

$$minLoD = t\sqrt{(\delta z_{DEMnew_i})^2 + (\delta z_{DEMold_i})^2} \qquad [3]$$

when the difference in elevation (z_{new} - z_{old}) in a given cell is smaller than the *minLoD*, the change is considered uncertain at the chosen confidence interval t (e.g., 1.28 for 80% CI, 1.96 for 95% CI).

3.2.5 DEMs generation

The minimum elevation within each grid cell (Zmin) obtained by ToPCAT for each multi-temporal point cloud could be used to develop a TIN (Triangular Irregular Network; Section J in Fig. 3.1) in which the breaklines of the structures surveyed with the total station or the GNNS can also be included (Section A in Fig. 3.1). Prior to selecting the interpolation algorithm, it is essential to consider the data density, the surface composition, and the topographic complexity (Milan et al., 2011). TINs have been often used in fluvial geomorphology (e.g., Brasington et al., 2000) especially when the survey data feature high point density. In some context, the sharp discontinuities produced from TIN can be very unnatural and other interpolation algorithms are more appropriate. However, Heritage et al. (2009) and Milan et al. (2011) stated that TINs are computationally efficient and well suited to discontinuous shapes such as ridges and breaks of slope, present in complex environments. Therefore, in these conditions, TINs are considered suitable and can be converted to a raster to obtain the DEM.

3.2.6 DoD and budget segregation

Topographic changes are analysed through the comparison of sequential DEMs (DoD; Section K in Fig. 3.1) where a simple DEMs cell-by-cell subtraction is performed to calculate, knowing the size of each cell, the total volumes of erosion, deposition and net change. The significance of these changes is thresholded by applying a spatial *minLoD* as described in "Multiple Error Assessment and minimum Level of Detection" step. The Geomorphic Change Detection (GCD) software for ArcGIS (Wheaton et al., 2010; available in http://gcd6help.joewheaton.org/) is used to threshold the DoDs to robustly distinguish real changes from noise. Moreover, the budget segregation function of GCD could be used to segment the DoD by specific areas of interest to investigate their erosional and depositional features for quantifying in detail the spatial pattern of erosion and deposition induced, for example, by the passage of debris flows.

3.3 LiDAR workflow

The sediment dynamics at the catchment scale was investigated through the realization of high-resolution DEMs, derived from LiDAR surveys. The 4D-data allow the analysis of morphological change due to debris-flow events and the application of geomorphometric index. The latter is useful for the assessment of sediment connectivity changes in the time at the catchment scale, in a torrent equipped with torrent control structures.

As already mentioned in the introductory part, multi-temporal LiDAR often presents several problems when two point clouds of different epochs need to be compared, especially when they are not homogeneous in terms of quality and they are not perfectly aligned. Therefore, it is important to develop a workflow (Fig. 3.2) that aims at addressing all the possible issues and errors that multi-temporal comparison could generate. In the following sections on the main procedural steps are described: (*i*) pre-processing (A in Fig. 3.2), (*ii*) data processing and DEM generation (B to E in Fig. 3.2), (*iii*) data and error analysis, (F and G in Fig. 3.2) and (*iv*), the assessment of debris-flow dynamic through DoDs and the sediment connectivity analysis (H and I in Fig. 3.2).

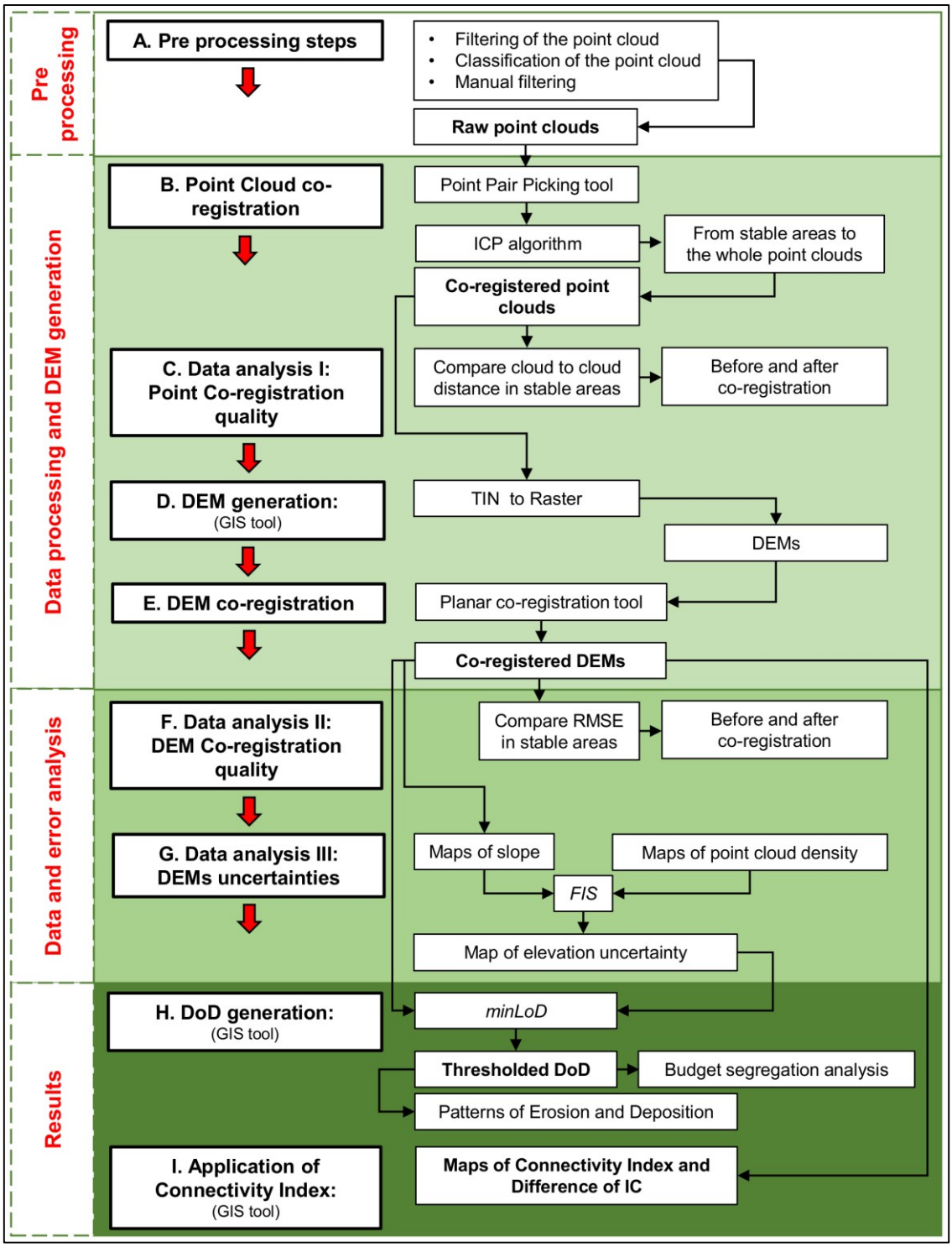

Figure 3.2: LiDAR data workflow chart, composed of nine main interrelated sections (see text for more details).

3.3.1 LiDAR surveys

The LiDAR surveys, covering all catchment and the alluvial fan of the Moscardo torrent (with the exception of the 2013 survey covering only the basin), were acquired in 2003, 2009 and 2013. Table 3.1 summarizes the characteristics of each flight.

- **2003**: The first survey was acquired from a helicopter using an Optech ALTM 3033, at an average altitude of 1000 m above ground level (a.g.l.) during snow-free conditions in November 2003. The flying speed was 80 knots, the scan angle 20 degrees and the scan rate 33 kHz. The survey design point density (Fig. 3.3a) was specified to be 2.5 points per m^2, with first and last return recorded, and a vertical accuracy <15 cm (Cavalli and Marchi, 2008). The survey point density of bare ground was 0.26 points per m^2.
- **2009**: LiDAR data of 2009 were acquired using an Optech ALTM Gemini at an average altitude of 850 m (a.g.l.) in August 2009. The scan angle was 25 degrees and the scan rate 57 kHz. The survey design point density (Fig. 3.3b) was specified to be 4 points per m^2 while the density of bare ground was 1.85 points per m^2.
- **2013**: 2013 LiDAR survey was carried out using an Optech ALTM 3100EA scanner, from a helicopter at an average altitude of 500 m (a.g.l.), on 14 June 2013 (snow-free conditions). The flying speed was 50 knots, the scan angle 42 degrees and the scan rate 100 kHz. The mean density of 19 line scrapes was 15.03 points per m^2 for the all pulse return whereas the density of the last return was 12.66 points per m^2 (Fig. 3.3c). The survey point density of bare ground was 8.79 points per m^2 (Blasone, 2014).

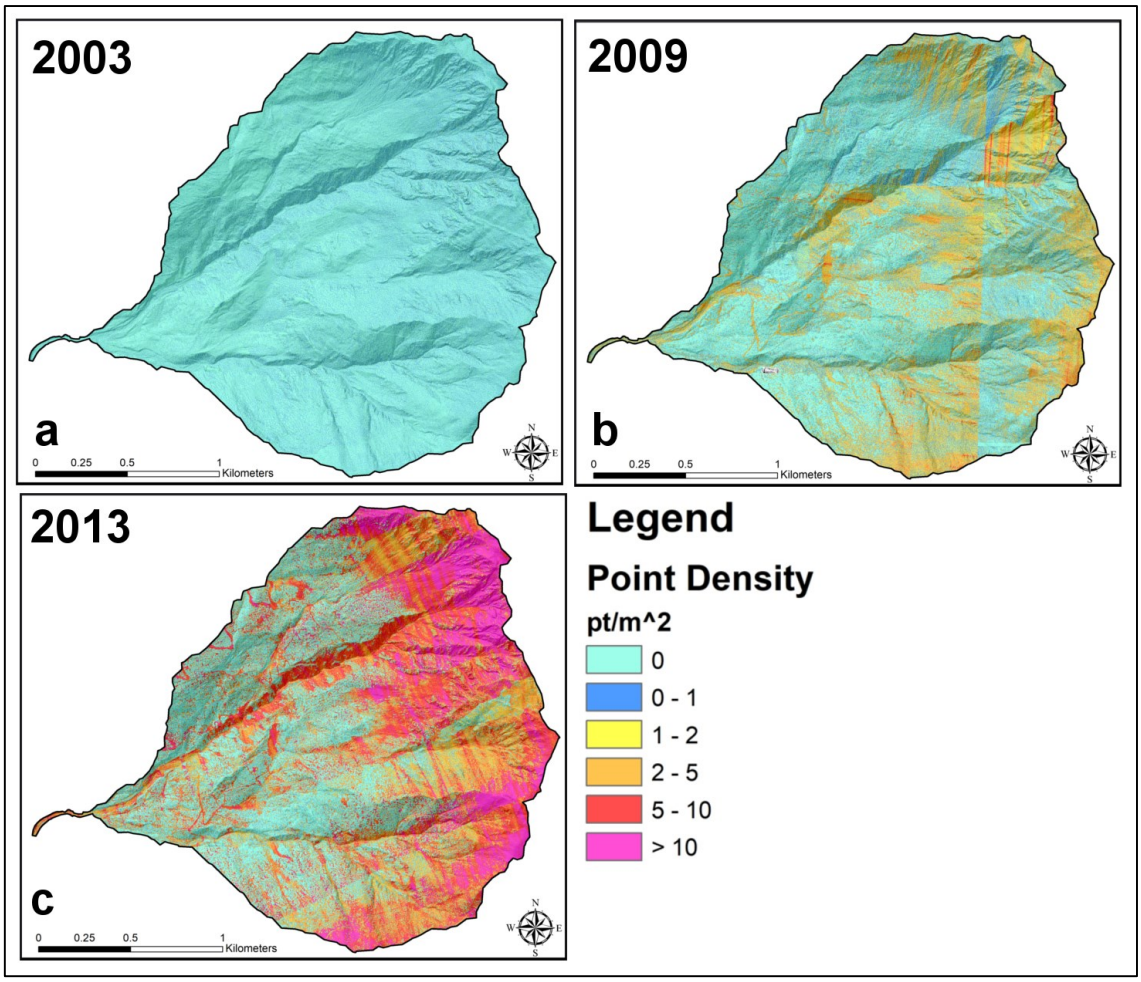

Figure 3.3: Comparison between the maps of LiDAR ground point density. a) The point density of the 2003 LiDAR survey. b) The point density of the 2009 LiDAR survey. c) The point density of the 2013 LiDAR survey.

Table 3.1: LiDAR flight parameters and point cloud data specifications from the 2003, 2009 and 2013 surveys.

	2003	**2009**	**2013**
Average flight altitude (a.s.l.)	1000 m	850 m	500 m
Scan angle	20°	25°	42°
Scan rate	33 kHz	~ 60 kHz	100 kHz
Total point density	2.5 pt/m^2	4 pt/m^2	15.03 pt/m^2
Bare ground point density	0.26 pt/m^2	1.85 pt/m^2	8.79 pt/m^2

LiDAR point measurements were filtered into returns from vegetation (and buildings) and bare ground using classification routines and algorithms of the Terrascan™ package (TerraScan, 2016; http://www.terrasolid.com). The classification of the point cloud, including vegetation classification, can be one of the most critical operations in natural and complex landscapes due to the multi-scale nature of the features present (Passalacqua et al., 2015). Then a manual check

was carried out to filter and remove every possible error linked to the software automatic classification (Section A in Fig. 3.2).

3.3.2 LiDAR Point clouds georeferencing and co-registration processes

The multi-temporal point clouds were projected in the WGS84 UTM-33N coordinate system and, in order to remove possible errors related to shift or rotation in the point clouds, they have been co-registered. The point clouds co-registration was carried out in two steps, using CloudCompare software through the Align (Point Pair Picking) tool and the ICP algorithm (Section B in Fig. 3.2). Initially, some homologous points (recognizable mainly in the stable areas of the surveys) were selected in the different point clouds to roughly align the survey, with the aim of improving the quality of the following ICP application. Then, in order to obtain a registration matrix to be applied to the whole point clouds, an initial co-registration was performed only on a subset of the point clouds located in stable areas, such as rocky outcrop, forest roads, stable meadows, human infrastructures. Finally, a rigid transformation was applied to the whole-original point clouds using the matrix derived by ICP application. The most recent and accurate data (i.e., 2013-point cloud) as a reference for the alignment, was used. To assess the effectiveness of the point cloud co-registration step, the M3C2 tool of Cloud Compare v. 2.9.1 (Lague et al., 2013) was used to calculate the cloud-to-cloud distance between the multi-temporal point clouds located in stable areas before and after the co-registration process (Section C in Fig. 3.2). As in Section 3.2.4, the standard deviation (SD) of the distance between point clouds was used as an indication of the measurement precision, while the absolute mean of distance was considered as the accuracy of the point clouds.

3.3.3 DEM generation and co-registration process

The co-registered LiDAR point clouds were interpolated into TINs (Section D in Fig. 3.2). Finally, the TIN was converted into a raster using Natural Neighbour interpolation to obtain the DEMs (2003 – 2009 – 2013; Section D in Fig. 3.2). The DEM grid spacing of 1 m was chosen to reach the finer possible resolution given the suitable point cloud density of LiDAR 2009 and 2013.

In order to further improve the accuracy of the point cloud co-registration, a second registration step was carried out on the raster DEMs (Section E in Fig. 3.2). A specific tool was developed to perform a planar co-registration, shifting the target DEM, in order to minimize the RMSE (Root Mean Square Error) with the reference DEM, by analysing areas subset of the DEMs that were not subject to change. Given a reference DEM_r with pixel size p_r (m), a target DEM_t with pixel size p_t (m), a base shift s (m) and a maximum shift w (m), initially each pixel of the two DEMs was subdivided into a number of equal pixels of size s in order to obtain two reduced *RDEM* with

an equal number of columns and rows. Then the $RDEM_t$ was iteratively and alternatively shifted in X and Y with increasing multiples of s and, at each shift step, the Root Mean Square Error ($RMSE_{xy}$) is computed, only for stable areas, as (Eq. 4):

$$RMSE_{xy} = \sqrt{\frac{\sum_{xy}\left(RDEM_{t,xy} - RDEM_{r,xy}\right)^2}{number\ of\ pixels}} \qquad [4]$$

Finally, the tool finds $min(RMSE_{xy})$ and with this given x and y shifts adjusts the target DEM_t with pixel size p_t for the whole catchment (Section F in Fig. 3.2).

3.3.4 DoDs generation and error analysis

The geomorphic change due to debris-flow events was assessed using DoDs at the catchment scale. Also in this case, in order to obtain a reliable DoD and to discriminate the actual changes in surface elevation from noise, the analyses of DEMs uncertainties and error propagation were carried out. Moreover, as mentioned in Section 3.2.4, in high topographic complex environments a spatially distributed error approach is needed. There are many different approaches in building spatially variable error models, but not all of these methods are appropriate for all surveys and it is important to find the most appropriate solution (Vericat et al., 2015). For example, Kaplinski et al. (2014) differentiated a spatial error estimate for each survey method. In complex topographic survey at wide scale (e.g., catchment) through LiDAR, different factors as slope (Scheidl et al., 2008; Milan et al., 2011), wet or dry areas (Brasington et al., 2003), point cloud quality (Schürch et al., 2011) or a combination of slope, sampling density and positional point quality (Picco et al., 2013) can determine the surface uncertainties (Blasone et al., 2014; Keilig et al., 2019). Therefore, LiDAR data need a different analysis of DEMs uncertainties than SfM data (Section 3.2.4), because the spatial scale and the source of errors are different. Thus, the method proposed by Wheaton et al. (2010), encompassing the use of fuzzy inference systems (FIS) to assess spatially variable errors, was considered more suitable in this case (Section G in Fig. 3.2). FIS is a convenient framework for taking the information that is known (e.g. point density, slope, etc.) and producing an appropriate output (i.e., a spatially distributed δz in this case) based on expert-based rule tables (Vericat et al., 2017). In this approach, both input and output are represented with continuous variables and use fuzzy membership functions to translate them into categorical data. The key to fuzzy inference systems is that membership of a given category can overlap and, therefore, multiple rules can apply to any combination of input, which gives rise to a much richer model output.

Following the approach by Cavalli et al. (2017), the spatially variable uncertainty assessment was addressed by creating ad-hoc FIS (Fig. 3.4) using slope and point clouds density as proxies for

vertical uncertainty in the DEMs. Slope and point density were chosen to represent a proxy of survey accuracy and uncertainty related to topographic complexity (Wheaton et al., 2013). Geomorphic Change Detection (GCD) ArcGIS plugin developed by Wheaton et al. (2010) was used to create the FIS by defining Membership Functions (MFs) for the input variables (i.e., slope and point density). Three classes (Low, Medium, High) were identified by setting a range of values for each class of the input data. The second step required the definition of the rules relating inputs to outputs. The last phase of FIS was the definition of the MF for the elevation uncertainty (δz) output variable (i.e., four classes: Low, Average, High, Extreme; Tab. 3.2). These functions were calibrated for each parameter to the observed ranges of variability assigning to high point density a higher weight (Cavalli et al., 2017). Finally, a map of spatially vertical uncertainty δz of each individual DEM was obtained. Then, the elevation errors of each survey is propagated into the DoDs according to Equation 2 and 3. As in Section 3.2.4, the maps of significant elevation change and volumes of erosion and deposition were calculated by multiplying all elevation changes in the DoD raster cell, thresholded considering a critical *minLoD* (Section H in Fig. 3.2), by the cell area and accounting separately for erosion and deposition areas in the Moscardo catchment. In this case, a t = 1.96 (i.e., 95% CI) was used to follow a conservative approach.

Table 3.2: Rules definition scheme for the two-input FIS used to evaluate geomorphic changes in the Moscardo basin.

Slope (%) / **Point density (pt/m²)**	**Low**	**Medium**	**High**
Low	High δz	High δz	Extreme δz
Medium	Average δz	Average δz	High δz
High	Low δz	Average δz	Average δz

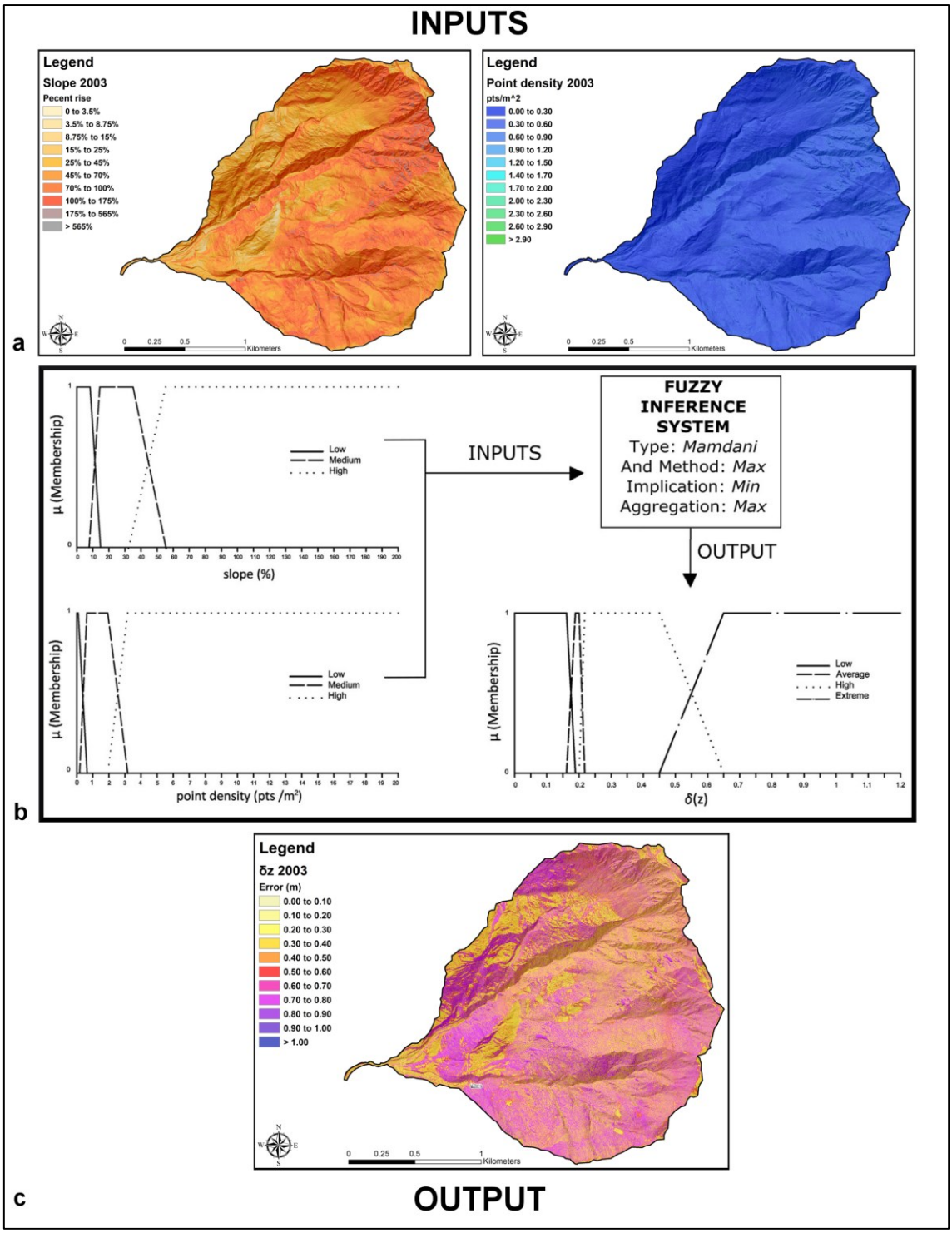

Figure 3.4: Example of FIS workflow. a) Inputs: maps of slope and point density. b) Fuzzy membership functions (Cavalli et al., 2017). c) Output: map of elevation uncertainty (δz).

Also in this case, the budget segregation function of GCD ArcGIS plugin (Section H in Fig. 3.2) was used to segment the DoDs in specific zones of interest, as the channel areas where the torrent control works were built. Moreover, the net balance resulting from the DoDs estimates within a

certain time span was compared with the data recorded at the monitoring station in the same period, to test the consistency of DoDs estimation.

3.4 Index of Connectivity (IC) and Difference of IC (DoIC)

The connectivity index (IC) proposed by Cavalli et al. (2013), that is a new version of the landscape-based index developed by Borselli et al. (2008), was used in order to investigate the effect of check dams on sediment connectivity. Following the approach of Cavalli et al. (2013) and, Crema and Cavalli (2018), IC is defined as (Eq. 5):

$$IC = log_{10}\left(\frac{D_{up}}{D_{dn}}\right) \qquad [5]$$

where D_{up} and D_{dn} are the upslope and downslope components of connectivity respectively (Fig. 3.5). IC is defined in the range of $[-\infty, +\infty]$, with connectivity increasing for larger IC values. D_{up} is the potential for downward routing of the sediment that is produced upstream and it depends on the upslope contributing area, mean slope and terrain roughness. It is assessed as follows (Eq. 6):

$$D_{up} = \overline{WS}\sqrt{A} \qquad [6]$$

Where, A is the upslope contributing area (m^2), $\overline{W}$ is the average weighting factor of the upslope contributing area, and $\overline{S}$ is the average slope of the upslope contributing area (m/m). The weighting factor, intended as a proxy of sediment fluxes impedance, results from a local measure of surface roughness, derivable from the DEM (Cavalli and Marchi, 2008).

D_{dn} takes into account the flow path length that a particle has to travel to arrive at the nearest target (e.g., catchment outlet) or sink (e.g., check dam) and it depends on path length, terrain roughness and gradient along the downslope path (Eq. 7):

$$D_{dn} = \sum_i \frac{d_i}{W_i S_i} \qquad [7]$$

d_i is the length of the flow path along the i^{th} cell according to the steepest downslope direction (m), Wi and Si are the weighting factor and the slope of the i^{th} cell, respectively.

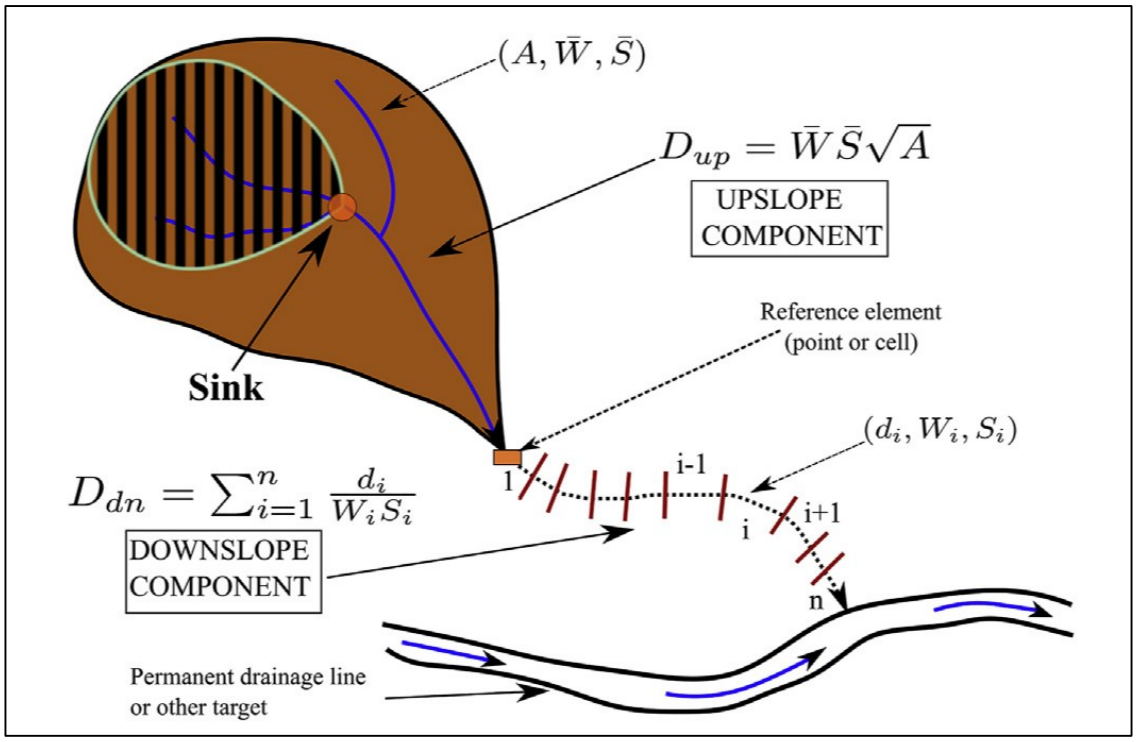

Figure 3.5: Index of sediment connectivity: components, computation, and representation (Crema and Cavalli, 2018).

IC was computed for the three DEMs (2003-2009-2013; Section I in Fig. 3.2) by using the stand-alone application SedInConnect 2.3 (Crema and Cavalli, 2018). The main required inputs are: (*i*) a DEM that can be hydrologically corrected for local depression to carry out a catchment-scale analysis, or uncorrected, preserving the original morphology, to characterize sediment pathways considering local sinks; (*ii*) a target feature (set at the monitoring station in this study) and, (*iii*) the original DEM (not hydrologically corrected) to compute the weighting factor, representing the impedance to runoff and sediment fluxes, due to surface roughness. More details on IC computation can be found in Cavalli et al. (2013) and, Crema and Cavalli (2018).

The main aim of connectivity analysis was the assessment of changes in sediment connectivity in the 2003-2013 time window and the investigation of the interaction among changes in sediment transfer pathways, natural processes and hydraulic control works in the catchment. The Differences of IC (DoIC) were calculated through the subtraction of the new and the old IC maps. Results of connectivity analysis have been finally compared with the erosion and deposition patterns derived from DoDs analyses to investigate the relationship between sediment dynamic changes induced by debris-flow processes and torrent control works functionality.

3.5 Inventory of torrent control works

An inventory of the hydraulic control works built along the main channel of the Moscardo Torrent over the last decades has been created by exploiting the Regional Cadastre of hydraulic structures

built by Friuli Venezia Giulia Region (IRDAT, 2018) and through field surveys. This database gathers all the structures characteristics, the year of their buildings, their locations and their functional states at the survey data. The studies and technical designs by Kravina (1974), Puntel (1993) and Arattano et al. (1996) that report important information about the Moscardo torrent control works over the time, were also consulted. In order to verify the database and to update it with the current functional state, a full GNSS field survey of structures was carried out in April 2018. The structures were surveyed using a Leica Zeno 20 L1+L2 GNSS system in Relative Stop&Go post-processed mode. All the points coordinates were referred to RDN2008/ UTM zone 33N (EPSG: 7792) reference system, which is the current Italian national realization of ETRS89.

4. Results and discussion

4.1 Volumes of debris-flow events

The hydrographs recorded in the Moscardo Torrent (e.g., Fig. 4.1) show relevant differences (velocities and hydrograph shapes) from event to event. Sometimes the hydrographs appear to be very irregular with abrupt fluctuations of the stage (e.g., Fig. 4.1a), as if many smaller waves had followed the main surge (Marchi et al., 2002). In this case, it was difficult to determine the mean flow velocity, the peak discharge and volumes. In other cases, debris flows appear as a single, well-defined wave (e.g., Fig. 4.1c) with a steep front (e.g., Fig. 4.1d) followed by a continuous and regular decrease in flow height. A few, well-defined, smaller waves may follow the main surge. Moreover, in some cases malfunctions in the instrumentation prevented to record data.

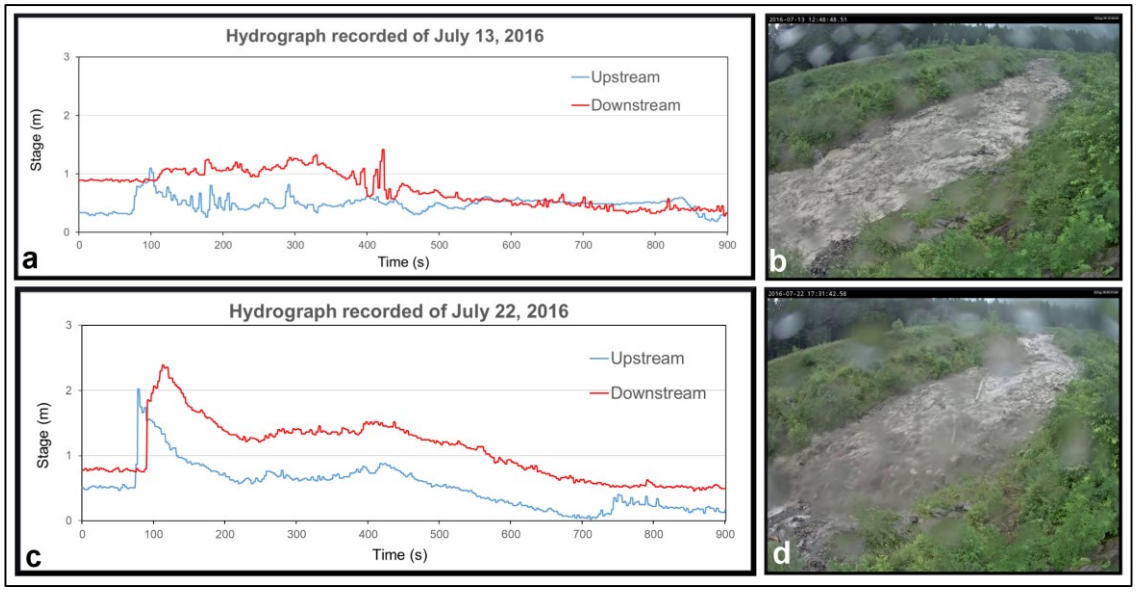

Figure 4.1: Example of debris-flow hydrographs recorded in July 2016 by ultrasonic sensors. a) Irregular Hydrographs recorded on 13 July 2016. b) A selected video picture of 13 July 2016 event. c) Hydrographs recorded on 22 July 2016. The characteristic sharp rising limb can be easily observed, denoting a well-defined wave with a steep front, followed by secondary smaller waves, which are common features observed in debris-flow hydrographs. d) A selected video picture of 22 July 2016 wave.

Table 4.1 summarizes the debris-flow volumes derived from the data recorded by the monitoring system (Marchi et al., 2002; Arattano et al., 2012; Blasone, 2014; Blasone et al., 2014) and the field estimates from 1990 to 2018 in the Moscardo Torrent.

*Table 4.1: Debris-flow events measured and estimated in the period 1990-2018 in the Moscardo catchment. In Marchi et al. (2002), Arattano et al. (2012), Blasone et al. (2014) can be found more details regarding these recorded data. The measures related to events in the period covered by LiDAR surveys (2003-2013) are outlined in bold. *These are considered total volumes, incorporating solids and water. **There were two classes of magnitude for recorded debris*

flows: the debris flows below the median of the measured debris-flow volumes were ascribed to the "small event" class (S), while "large event" class (L) were the debris flow over the median (Section 3.6). [(a)]Underestimated because final hydrograph part is missing (Blasone et al., 2014). [(b)]Assessed from average values representative of Moscardo's debris flows (Blasone et al., 2014).

Event data	Mean front velocity ($m\ s^{-1}$)	Peak discharge ($m^3\ s^{-1}$)	Debris-flow measured volume* (m^3)	Debris-flow estimated volume (central value) (m^3)	Magnitude class**
17.08.1990	1.0	-	-	-	S
13.08.1991	5.0	88	19000		L
30.09.1991	1.9	24	3250		S
01.09.1992	2.5	46	5800		S
11.07.1993	3.0	14	5600		S
19.07.1993	0.9	3	730		S
20.07.1993	4.3	16	6500		S
14.09.1993	2.5	-	3800		S
18.07.1994	4.0	-	-	-	L
05.07.1995	-	-		4320	S
22.06.1996	3.5	139	16133		L
08.07.1996	4	194	57800		L
27.06.1997	2.9	25	3000		S
23.06.1998	-	-	51000		L
04.08.2002	-	-		4320	S
23.07.2004	**-**	**-**		**4320**	**S**
24.06.2006	**1.6**	**-**	**5500**		**S**
09.06.2009	**-**	**-**		**4320**	**S**
29.08.2010	**-**	**-**		**4320**	**S**
14.09.2011	**3.6**	**71**	**4700 [(a)]**		**S**
24.09.2012	**3-4 [(b)]**	**91-121 [(b)]**	**57000 [(b)]**		**L**
27.09.2012	**3-4 [(b)]**	**119-159 [(b)]**	**89500 [(b)]**		**L**
16.06.2016	4.5	53-87	15936		L
11.07.2016	0.5	2-3	-	-	S
13.07.2016	2.4	22	-	-	S
22.07.2016	4.8	95-130	21808		L
10.08.2017	4.0	61-94	30000		L
12.06.2018	2.0	-	-	-	S

The time series includes four events (24 August 2006, 11 and 13 July 2016, 12 June 2018) which occurred as debris floods on the alluvial fan (e.g., Fig. 4.1a and b), but featured characteristics typical of debris flows in upstream channel reaches, where they caused significant morphological impacts. Therefore, it was important to keep track of them. For example, the event of 24 August 2006 was associated to a remarkable debris flows (Arattano et al., 2012) that deposited most

material upstream the check dam described in the next Section 4.4. Other events (17 August 1990 and 18 July 1994) were characterised by channel aggradation or degradation at the reach segment where the ultrasound stations were located. Therefore, the discharge and volume computations were not carried out for these events (Marchi et al., 2002).

Seven events occurred in the 2003-2013 period considered in the LiDAR analysis. The sensors installed at the monitoring station recorded four events, while others were estimated as described in Section 3.1. In addition, the volumes of debris-flow events were added in the two-time intervals covered by LiDAR surveys, considering uncertainty bounds (Tab. 4.2).

Table 4.2: Debris-flow volumes in the two-time intervals covered by LiDAR surveys.

Total debris-flow volume 2003-2009 (m^3)	**Uncertainty range 2003-2009 (m^3)**	**Total debris-flow volume 2009-2013 (m^3)**	**Uncertainty range 2009-2013 (m^3)**
14140	9050 - 19230	155520	132850 – 178190

Weekly surveys from spring to autumn and the analysis of monitoring station-recorded video permitted to identify these debris-flow events as the main responsible for the morphological changes observed in the Moscardo channel reach. The role of floods with bedload and suspended load mostly occurring in autumn and of snowmelt runoff, although not negligible, is small if compared to debris flows.

In addition, the rainfall data in the Moscardo were used to assess the trend of the rainfall pattern since the debris-flow events have been monitored (1990-2018). This information can be help to make some considerations on the role of torrent control works in the debris-flow dynamic. As described in Section 3.1, the rainfall pattern analysis examined the number of event per year that could be considered significant, based on the thresholds of the debris-flow triggering in the Moscardo basin. Table 4.3 displays the number of event per year with hourly rainfall intensity higher than 10 mm h^{-1} and 20 mm h^{-1} recorded by raingauges network of Moscardo catchment from 1990 to 2018. The data presented in Table 4.3 do not seem to be steady to perform an accurate statistical analysis for the trend detection because of the presence of there were several data gaps. However, these preliminary results showed how the evolution of the rainfall pattern has not undergone important changes during the monitoring time window, considering the number of events per year.

Table 4.3: The number of event per year with hourly rainfall intensity higher than 10 mm h^{-1} and 20 mm h^{-1} recorded by raingauges network (Fig. 2.4) of Moscardo catchment over the time. As described in Section 3.1., the analysis considered different raingauges of the Moscardo network. They are located very close to each other and to the debris-flow trigger area. In particular, the rainfall data of the raingauges with code C207, C202 and c (Fig. 2.4) were used for the rainfall pattern analysis. The selected raingauges showed the greatest data coverage in the time series.

Raingauge code	**C207**		**C202**		**c**	
Year	**no. of events > 10 mm/h**	**no. of events > 20 mm/h**	**no. of events > 10 mm/h**	**no. of events > 20 mm/h**	**no. of events > 10 mm/h**	**no. of events > 20 mm/h**
1990	10	1	-	-	-	-
1991	15	1	-	-	-	-
1992	-	-	-	-	-	-
1993	19	3	-	-	-	-
1994	19	6	-	-	-	-
1995	14	1	-	-	-	-
1996	17	3	-	-	-	-
1997	16	3	-	-	-	-
1998	-	-	-	-	32	9
1999	-	-	-	-	21	1
2000	-	-	-	-	-	-
2001	-	-	-	-	11	0
2002	-	-	-	-	15	2
2003	-	-	-	-	**17**	**3**
2004	-	-	-	-	**28**	**2**
2005	-	-	**27**	**12**	-	-
2006	-	-	-	-	**9**	**1**
2007	-	-	**24**	**6**	-	-
2008	-	-	**30**	**6**	-	-
2009	-	-	**12**	**3**	-	-
2010	**14**	**4**	**15**	**5**	-	-
2011	**19**	**5**	**13**	**2**	-	-
2012	**21**	**4**	**17**	**5**	-	-
2013	**10**	**0**	**7**	**0**	**9**	**0**
2014	17	2	16	3	14	2
2015	11	0	9	0	7	0
2016	15	4	12	1	-	-
2017	8	2	10	2	-	-
2018	20	0	24	3	-	-

4.2 Database of torrent control works

The database of torrent control works was fundamental to assess the functionality over time of structures. Table 4.4 shows the torrent control works in the main stream of the Moscardo Torrent in 2018 (Fig. 4.2). The GNSS survey allowed the identification of 32 structures, recorded in the database with a progressive identification number (hereafter n.).

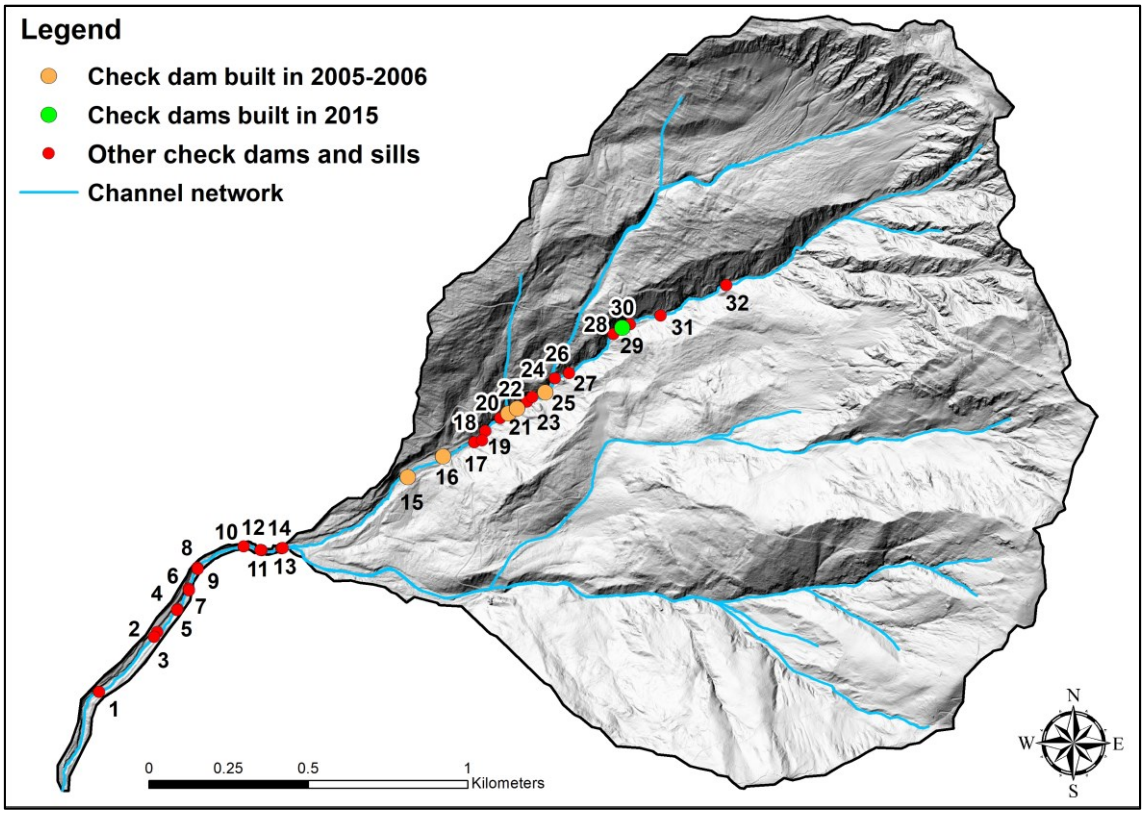

Figure 4.2: The current torrent control works in the main stream of the Moscardo Torrent in 2018. Each structure has a progressive identification number in the database.

Table 4.4: Existed torrent control works in the main stream of the Moscardo Torrent in 2018 (Fig. 4.2) and their functionality.

Typology of Structures	**Number of structures**	**Year of building**	**Functionality/Status: number of structures**	**Check dam / sill number (Fig. 4.2)**
Sills	1	1980	Operative: 1	n. 1
Check dam	13	1980	Filled: 1	n. 19
			Destroyed: 3	n. 17, 18, 28
			Damaged: 7	n. 2, 20, 23, 24, 27, 31, 32
			Operative: 1	n. 3
			Destroyed/Rebuilt in 2015: 1	n. 30
Check dam	1	1990	Operative: 1	n. 26
Sills	10	1993	Damaged: 1	n. 6
			Operative: 9	n. 4, 5, 7, 9, 10, 11, 12, 13, 14
Check dam	1	1993	Damaged: 1	n. 8
Check dam	3	2005	Over filled: 1	n. 16
			Operative: 2	n. 21, 22
Check dam	2	2006	Operative: 2	n. 15, 25
Check dam	1	2015	Operative: 1	n. 29

Over time, many torrent control works were over filled, damaged or destroyed (Fig. 4.3) by debris-flow events along the Moscardo main channel.

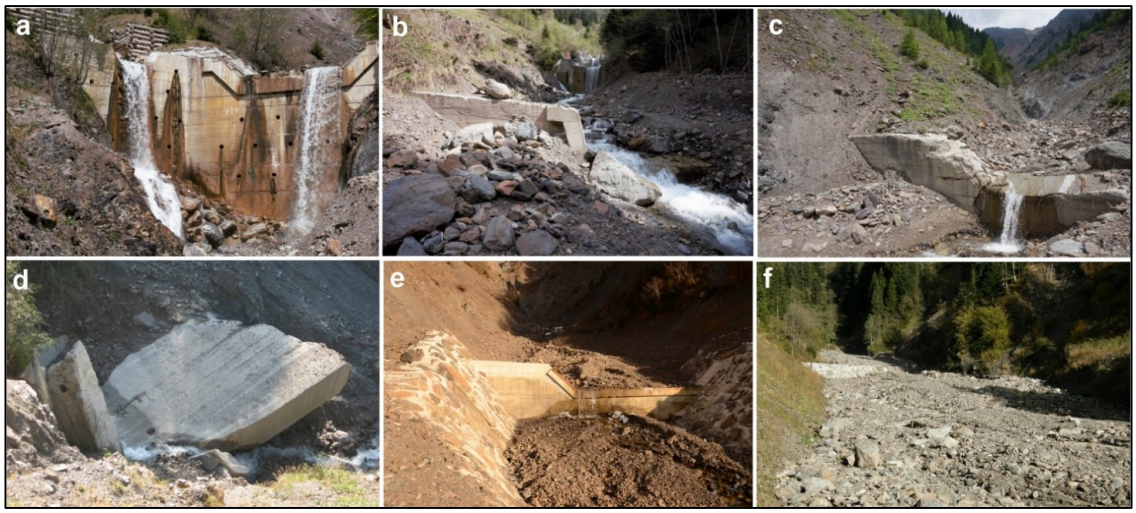

Figure 4.3: Examples of Moscardo check dams (Fig. 4.2) and their functionality (Tab. 4.4): a) Operative check dam (n. 26). Cucchiaro 2018; b) Filled check dam (n. 19). Cucchiaro 2018; c) Damaged check dam (n. 31). Cucchiaro 2018; d) Destroyed check dam (n. 28). Blasone 2011; e) Rebuilt check dam (n. 30). Cucchiaro 2015; f) Over filled check dam (n. 16). Blasone 2011.

Some structures, as the check dam n. 17, were destroyed and flowed downstream by debris-flow events, becoming hardly detectable along the channel (i.e., Fig. 4.4).

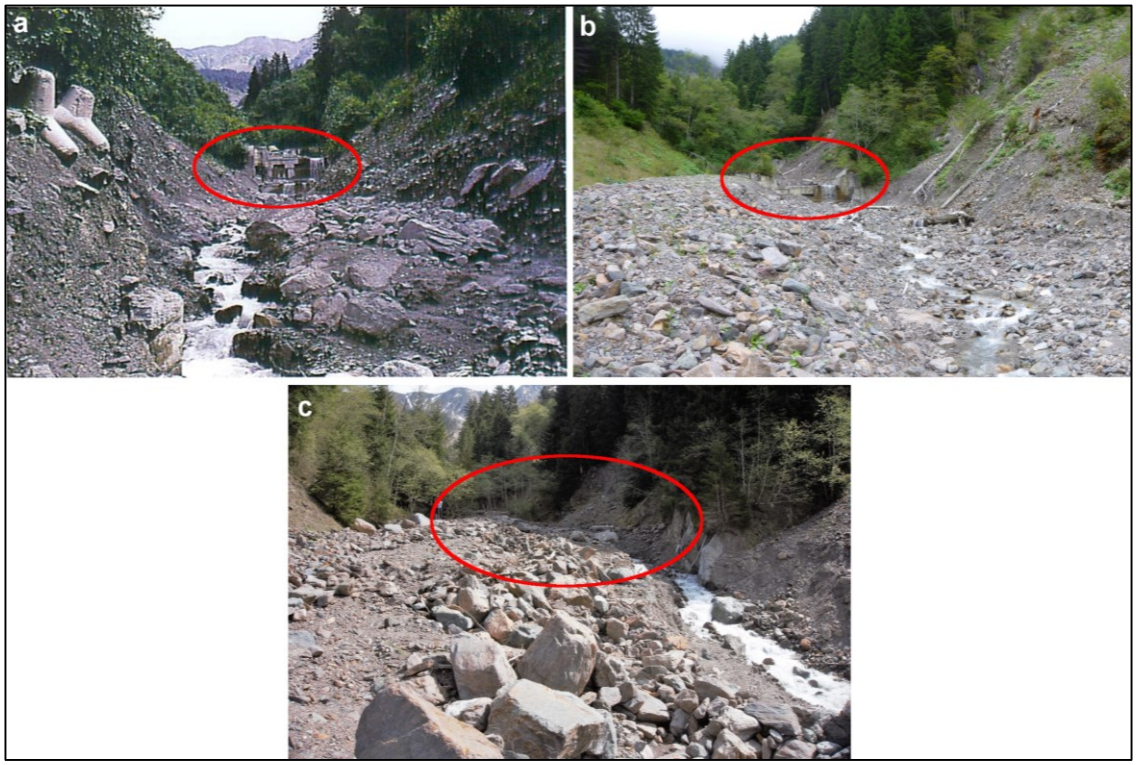

Figure 4.4: Example of check dam functionality during the time. The check dam (n. 17) was built at 1067 m a.s.l. on the Moscardo main channel in 1980. Over time, the sediment damaged and over filled the check dam. Then the structure

was flowed downstream by debris flow events. a) The check dam in Arattano et al. (1996) when the functionality of the structure was still active. b) The check dam in 2013 when the structure was filled. Blasone 2013. c) The check dam in 2018 when it has been no longer visible along the channel. Cucchiaro 2018.

In 2003-2013 time span, five check dams were built along the Moscardo stream between 2005-2006 (Fig. 4.5). In particular, in 2006 an important check dam (n. 15; Fig. 4.5a), in terms of size, was built in the lower part of the Moscardo reach (height at the spillway level of 7 m, length 50 m and width 1 m). The aim of these structures was to control channel incision and retain sediment transported by debris flows, thus reducing its delivery to the alluvial fan and to the receiving stream (But Torrent; Fig. 2.1).

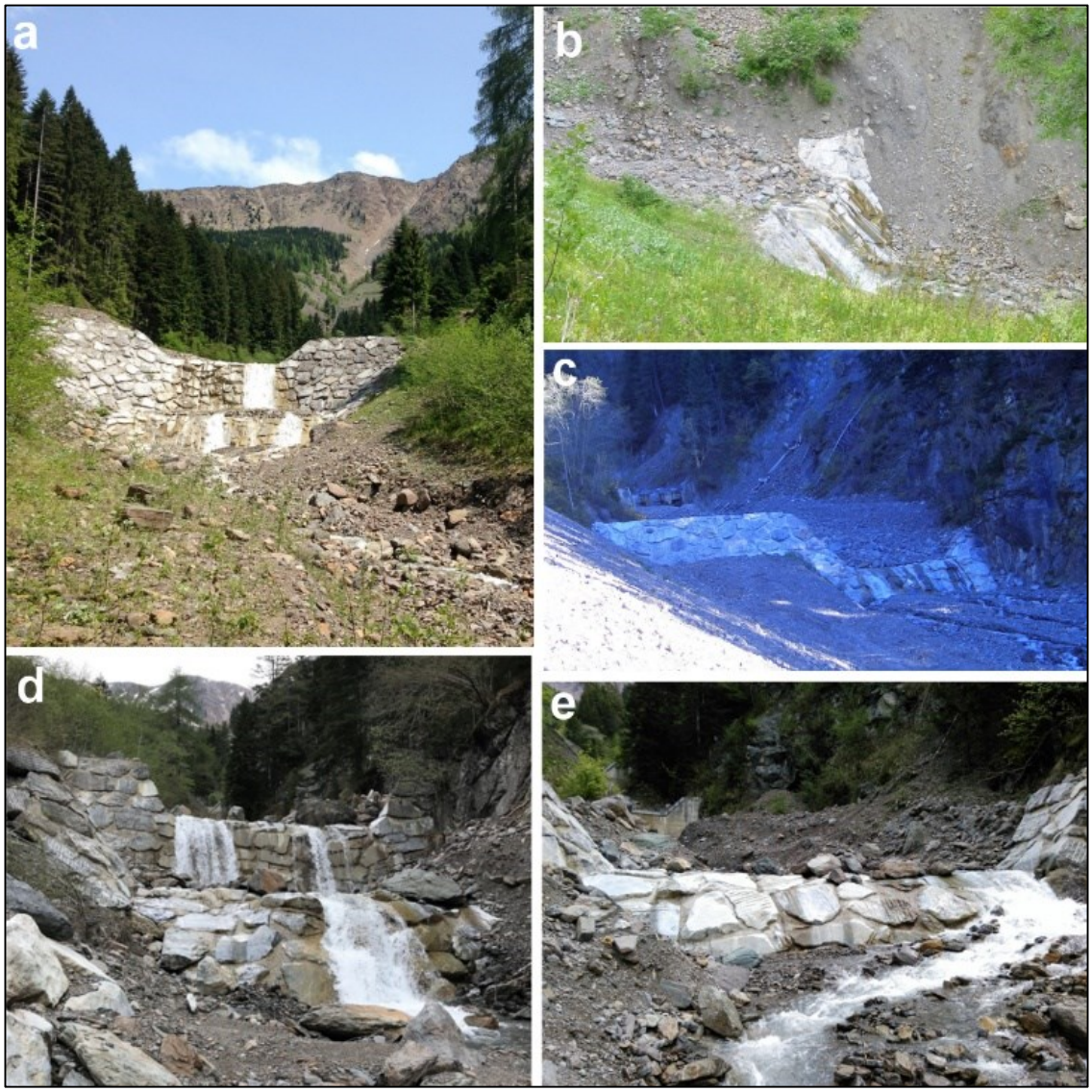

Figure 4.5: Check dams built along the Moscardo stream between 2005-2006 (Fig. 4.2). a) Check dam (n. 15) built in the lower part of the Moscardo channel. Cucchiaro 2018; b) Check dam (n. 25) built in the middle part of the Moscardo channel. Cucchiaro 2018; c) Check dam (n. 16) built in the lower part of the Moscardo channel. Cavalli 2006; d)

Check dam (n. 21) built in the middle part of the Moscardo channel. Cucchiaro 2018; e) Check dam (n. 22) built in the middle part of the Moscardo channel. Cucchiaro 2018.

At the beginning of 2015, two new check dams (n. 29 and 30; Fig. 4.6a, b, c and d) were built in the upper part of the basin (Fig. 4.2), close to the main area of debris-flow triggering. The lower (most downstream) check dam n. 29 (height at the spillway level 3 m, length 27 m and width 1.5 m; Fig. 4.6b) was built close to another one, fully destroyed a few years ago (n. 28; Fig. 4.3d). The upper check dam n. 30 (height at the spillway level 2 m, length 20 m and width 2 m; Fig. 4.6a) was built at the site of a former dam that had been seriously damaged by past debris flows. The aim of the works was the same as the check dams built during 2005-2006, to control channel erosion and store sediment transported by debris flows. A further motivation for these check dams is to stabilize the foot of the slope (Fig. 4.6d), which is an active source of sediment for the debris flows.

The building of these two check dams in this area represented a good opportunity to monitor the topographic changes caused by the interaction of debris flows with check dams (see the next Section 4.3).

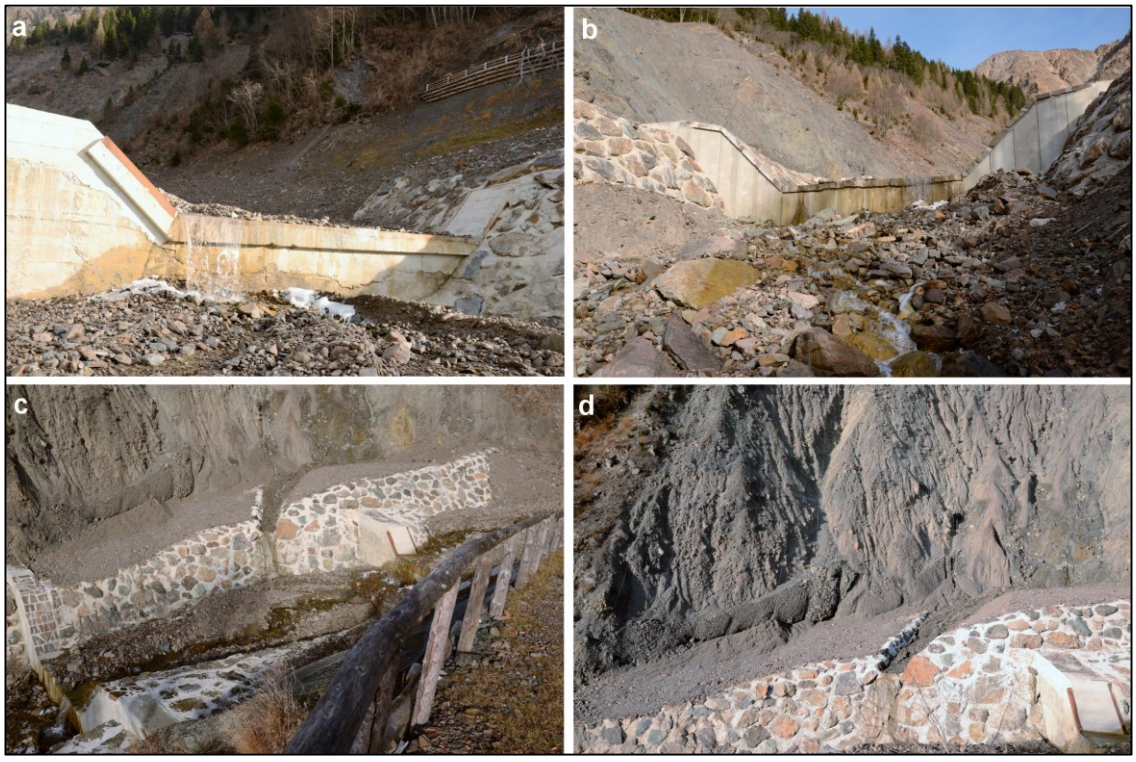

Figure 4.6: The check dams built in 2015 in the upper part of the Moscardo catchment (Fig. 4.2). Cucchiaro 2015. a) The upper check dam (n. 30) rebuilt in 2015. b) The lower check dam (n. 29) built in 2015; c) SfM study area where hydraulic control works were realized in 2015; d) The right bank of hydraulic control works.

4.3 SfM data

The 4D-SfM surveys were carried out in the upper part of Moscardo Torrent along the main channel (1180 m a.s.l.; Fig. 4.7a). Steep slopes and rugged and hardly accessible zones characterize the study area where severe topographic changes were observed after every debris flow. This area covers 2015 m^2 and has an average slope of 55% (Fig. 4.7b, c) and two concreate check dams (n. 29 and 30; Fig. 4.6) were built in 2015, as described in previous Section 4.2.

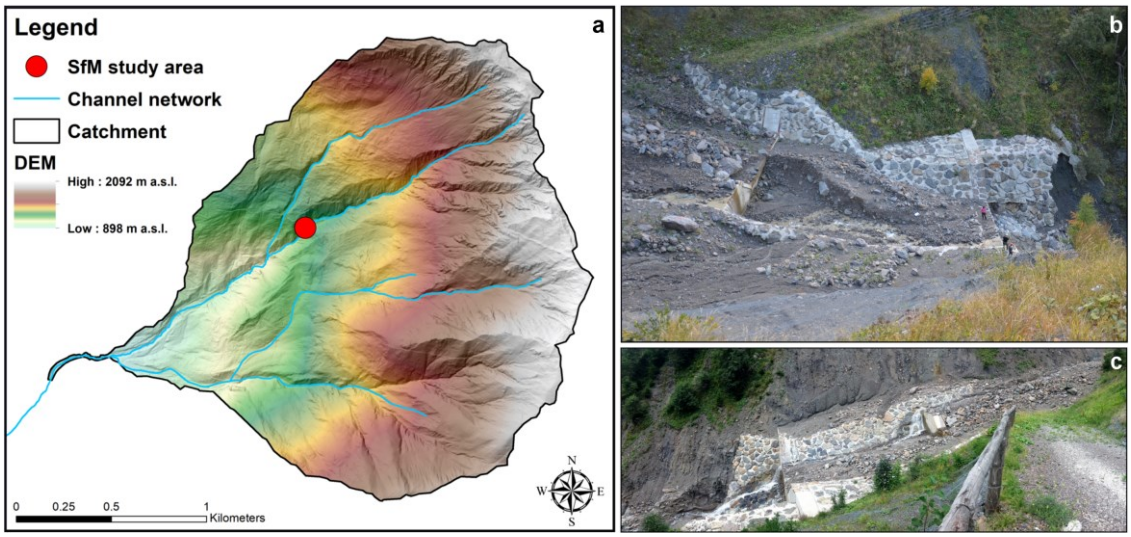

Figure 4.7: The SfM study area in the Moscardo catchment where two concreate check dams (n. 29 and 30) were built in 2015. a) The location of the SfM study area in the Moscardo basin. b) The study area seen from the top of the right slope. Marchi 2018. c) The study area seen from the left slope. Cucchiaro 2017.

4.3.1 Acquisition and data processing

Ten SfM surveys were carried out from December 2015 to October 2018 in the study area (Fig. 4.8). The surveys were done before and after each winter season (December 2015, June 2016, October 2016, and May 2017), as well as after the debris-flows events (July 2016, August 2016, July 2017, August 2017, June 2018, October 2018), which typically take place during summer months. In this time interval, six debris flows of different magnitude occurred. The surveys implemented before and after winter\early spring are intended to detect possible topographic variations caused by channelized snow avalanches or snowmelt runoff.

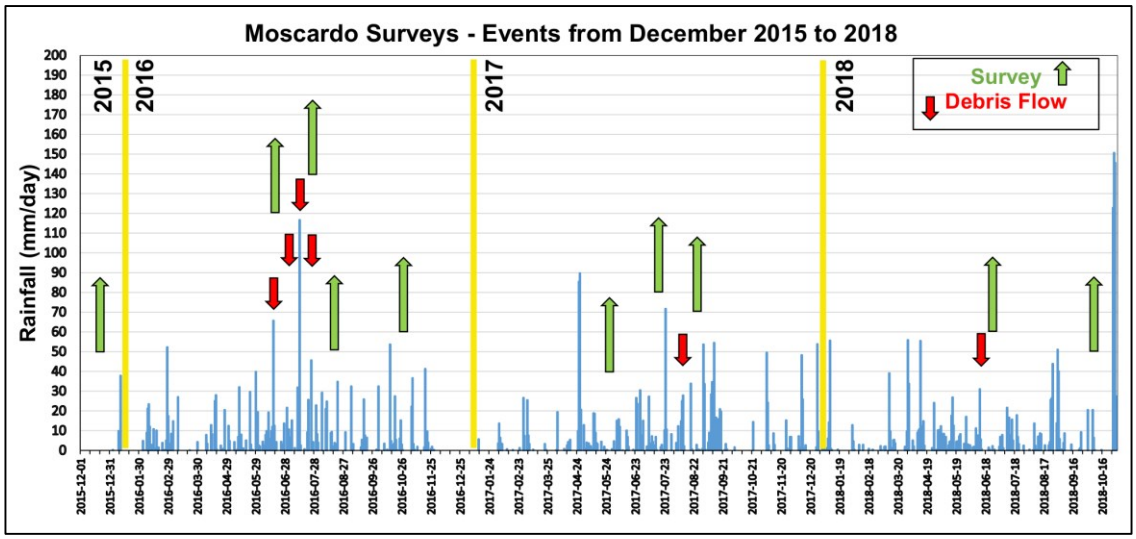

Figure 4.8: Timing of the SfM surveys in relation to rainfall measured by raingauges network of the Moscardo catchment and debris flow events.

Aerial and terrestrial images were collected with a Sony Alpha 5000 compact digital camera (20 Mpixels, focal length 16mm, APS-C sensor size 23.2 x 15.4 mm). For the aerial survey, the camera was mounted on a professional 8-rotors (on four axis) UAV (Neutech Airvision NT-4C; Fig. 4.9) that has high flexibility and stability in most weather conditions and needs only a small space for take-off and landing strip (a fundamental feature for the survey of a narrow and confined mountain channel). The GNSS signal is usually very low in the specific part of the catchment where the surveys were carried out. Therefore, it was not possible to plan the UAV flight strips and the image overlap by a software. The UAV missions were realised through manual flight mode and the time-lapse function of the camera allowed the capturing an image at 2 s intervals, sufficient to guarantee the overlap in sequential photographs, which is essential for the image matching algorithms used in SfM.

Figure 4.9: The 8-rotors UAV used for the surveys.

Test flights indicated that flying at 20 m altitude along three lines (flight speed 1.5 m/s) ensures a sufficiently large overlap (80% in flight direction and a flight strip overlap of 60%) and image footprint with a mean Ground Sampling Distance of 0.006 m. For the ground-based surveys, the photographs were taken maintaining an adequate average distance from the object (the images were taken from the perimeter and hillcrests of the study area); a mean baseline (3 m) between adjacent cameras positions avoided large jumps in scale and minimized the interval between image to reduce the effects of change in lighting conditions (Smith et al., 2015; Eltner et al., 2016). A Leica 1200 L1+L2 GPS (Global Positioning System) in Relative Stop&Go post-processed mode, allowed the surveying of check dams edges and n = 19 GCP (Fig. 4.10). The GCPs were kept in place and used in all surveys (i.e., fixed control network). However, they were re-surveyed frequently to make sure none had moved.

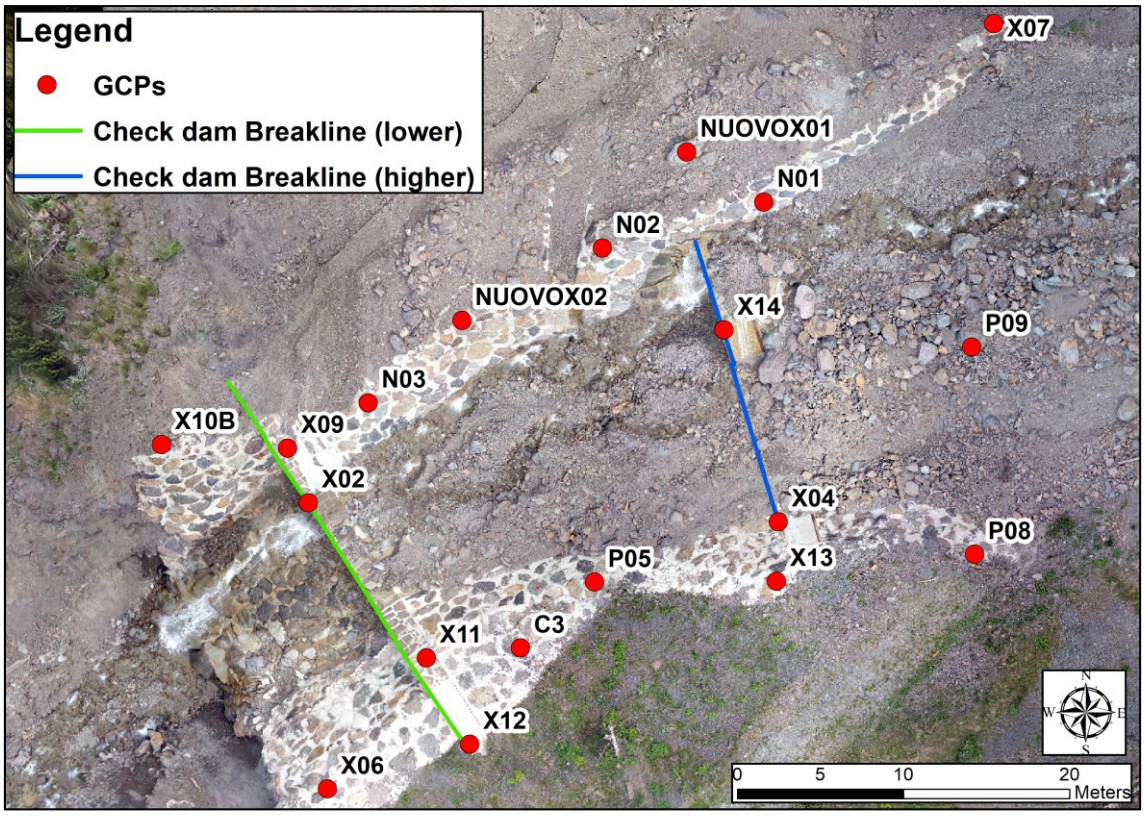

Figure 4.10: GCPs distribution and breaklines of check dam edges in the SfM study area.

*Table 4.5: Characteristics of the GPS and SfM surveys in the Moscardo study area. * Following Marteau et al. (2017) we applied a bootstrapping resampling technique to randomly select 1/3 of the GCPs and use them as CP to assess the uncertainty of each point (see Section 3.2.4). **Mean measures provided by Photoscan software, considering all GCPs as control points in the 3D model. GCPs image precision reflects the precision in image space that GCP observations were made to while tie points precision is the equivalent measure for tie points.*

Survey data	Number of images processed	Number of GCPs (as control, [as check])*	GPS positional accuracy of GCPs (Easting-Northing - Height; m)	GCPs image precision (pixel - m)**	Tie points image precision (pixel - m)**
15.12.2015	226	19 [6]	0.020 - 0.030	1.972 - 0.123	0.971 - 0.220
23.06.2016	100	19 [6]	0.030 - 0.040	2.130 - 0.051	0.914 - 0.199
22.07.2016	172	19 [6]	0.020 - 0.030	3.256 - 0.035	0.843 - 0.201
09.08.2016	172	19 [6]	0.020 - 0.040	1.938 - 0.050	1.441 - 0.298
28.10.2016	232	19 [6]	0.030 - 0.040	1.213 - 0.043	1.175 - 0.255
30.05.2017	240	19 [6]	0.030 - 0.040	1.640 - 0.048	1.257 - 0.250
20.07.2017	210	19 [6]	0.020 - 0.040	1.411 - 0.045	1.222 - 0.275
31.08.2017	289	19 [6]	0.020 - 0.030	1.007 - 0.037	1.314 - 0.271
19.06.2018	408	19 [6]	0.020 - 0.030	0.941 - 0.054	0.833 - 0.180
09.10.2018	297	19 [6]	0.030 - 0.040	0.929 - 0.032	0.970 - 0.193

All the points coordinates were referred to RDN2008 / UTM zone 33N (EPSG: 7792) reference system. Table 4.5 synthetizes the characteristics and the level of uncertainty of the GPS surveys and the 3D model of the scene (e.g., Fig. 4.11) obtained through the aerial and terrestrial photos processing with Agisoft Photoscan Pro v 1.2.0.

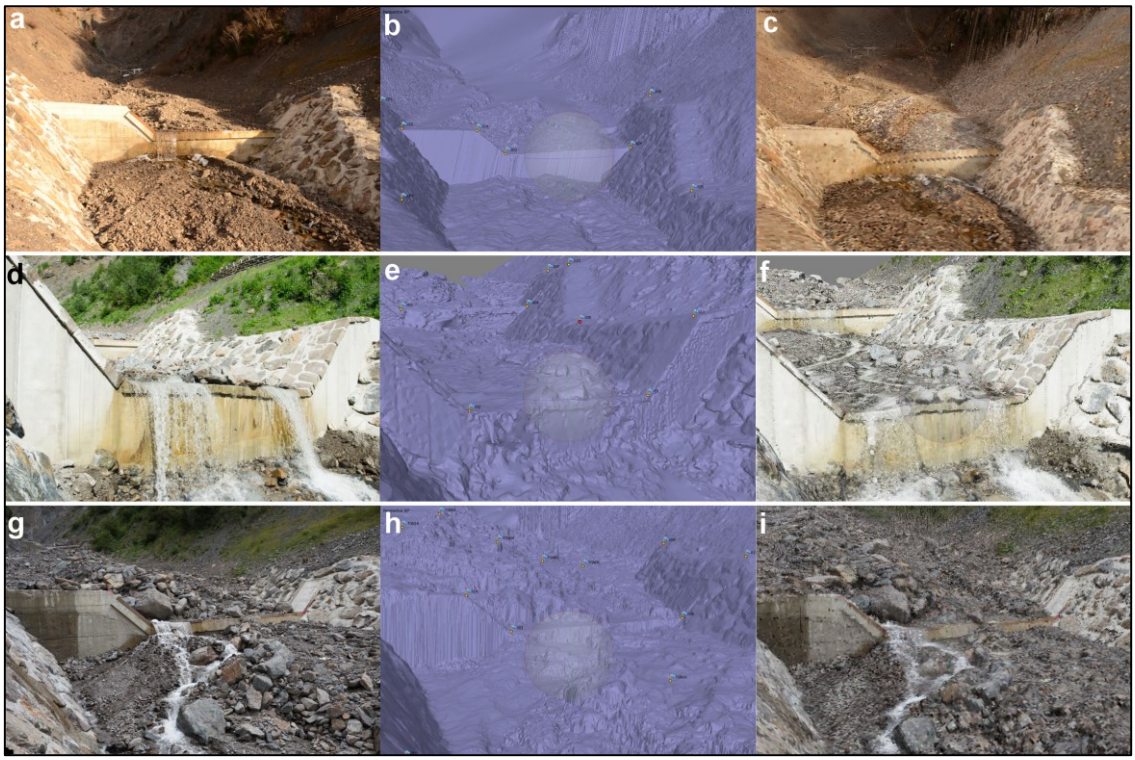

Figure 4.11: Example of comparison between the photos (used as input in SfM software) and 3D models (terrain and tiled model) obtained by Photoscan software for the SfM study area. a) The photo of the check dam (n. 30). Cucchiaro, December 2015. b) The terrain model that reconstruct 3D view of Figure 4.11a. c) The tailed model that reconstruct 3D view of Figure 4.11a. d) The photo of check dam (n. 29). Cucchiaro, June 2016. e) The terrain model that reconstruct 3D view of Figure 4.11d. f) The tailed model that reconstruct 3D view of Figure 4.11d. g) The photo of check dam (n. 30). Cucchiaro, August 2016. h) The terrain model that reconstruct 3D view of Figure 4.11g. i) The tailed model that reconstruct 3D view of Figure 4.11g.

The obtained 3D Photoscan point cloud (Fig. 4.12) showed that an integrated approach of ground-based images and aerial acquisition was needed to survey the complex topography of the Moscardo study area. Indeed, ground-based images can provide a more accurate representation of complex surfaces for detail-scale 3D reconstruction, especially when steep or sub-vertical surfaces (e.g., the vertical walls of the check dams) were surveyed (Passalacqua et al., 2015). However, the matching of oblique ground-based images over large areas can be unreliable on relatively flat terrain (Smith and Vericat, 2015) due to a very oblique perspective with a very low incidence angle (Stöcker et al., 2015). These key aspects were clearly visible in Figure 4.12a that represents a point cloud (density 6944 points/m^2) obtained only from ground-based images. It shows how the walls of check dams were well surveyed while there was a low density in flat

zones. However, the spatial extent of ground detection was much smaller than aerial survey that permits to cover large areas in small amounts of time (Piermattei et al., 2016; Mosbrucker et al., 2017). Nevertheless, aerial photos showed a poor representation of steep terrain with small curvature radii, and data gaps in vertically oriented and overhanging topography (Stöcker et al., 2015; Loye et al., 2016; Cook, 2017). Figure 4.12b, which represents a point cloud (density 9715 points/m^2) obtained only from UAV images, explicitly shows the data lack of vertical structures of the check dams that can be captured by including oblique images of vertical surfaces.

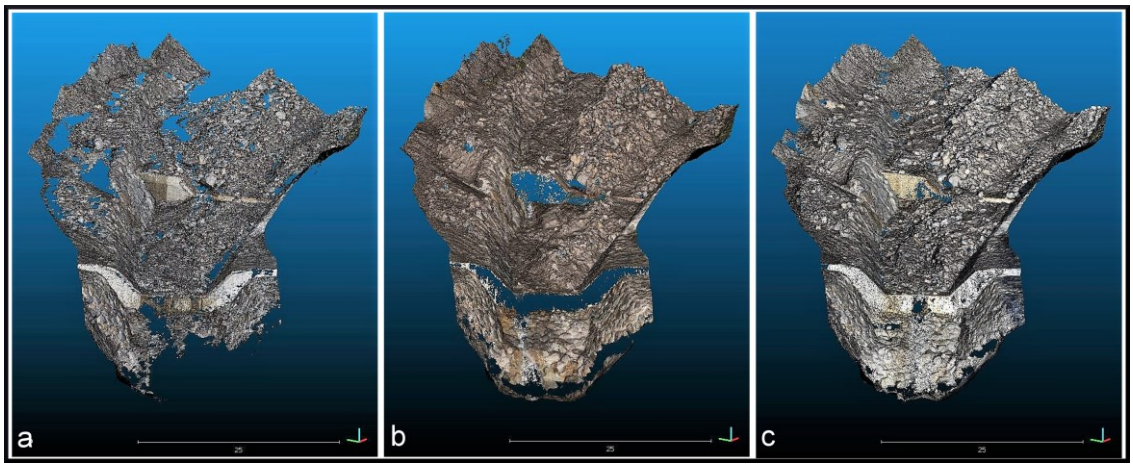

Figure 4.12: Dense point clouds of Moscardo SfM study area. (a) Point cloud of August 2016 (6944 points/m^2) obtained only from ground-based images (b) Point cloud of August 2017 (9715 points/m^2) obtained only from UAV images (c) Point cloud of October 2016 (15221 points/m^2) obtained from the integrated approach of terrestrial-aerial image.

Ground-based and UAV photos were directly fused to the alignment process in Photoscan to avoid subsequent data fusion problems at level of point clouds. Several studies used aerial and terrestrial photos in the SfM surveys (Stöcker et al., 2015; Smith and Vericat, 2015; Glendell et al., 2017; Koci et al., 2017), but rarely photogrammetric processing of aerial and terrestrial data was done together. The integrated approach of terrestrial-aerial image (Fig. 4.12c) allowed the achievement of (*i*) denser point clouds (15221 points/m^2); (*ii*) an optimal camera network geometry (i.e., great image overlap and high angle of convergence); (*iii*) point clouds without gaps in data; and (*iv*) fewer deformation errors or large-area distortions. Fonstad et al. (2013) confirmed that the union of ground-based and aerial images in SfM process permits overcoming many disadvantages, such as the line-of-sight obscuration that happen due to vegetation and other complex objects. Having many different cameras perspectives greatly increases the point cloud density, the individual point precision, the robustness of topographic mapping and high-resolution detail. In addition, Stöcker et al. (2015) found similar outcomes. They stated that high-density point clouds of gully headcuts, based on the fusion of UAV and terrestrial image SfM data, show a significant improvement of 3D reconstruction of gully systems, compared to unique processing of single data sources.

Moreover, Wackrow and Chandler (2011), James and Robson (2014), Smith and Vericat (2015), Bemis et al. (2014), Eltner et al. (2016) highlighted as the likelihood of detectable systematic DEM error in UAV surveys, as "doming effect", can be reduced through the collection of oblique imagery. Furthermore, James et al. (2017a) confirmed that the addition of oblique photographs into a UAV survey considerably strengthens the network geometry and reduces error in estimated camera parameters, thus minimising systematic DEM deformation, even if no control points are present.

Additionally, at the end of the image processing, orthomosaics with resolutions in agreement with the resolution of the photos were exported (Section J in Fig. 3.1).

4.3.2 Post-processing point clouds

Preliminary editing of the raw point cloud was performed in Cloud Compare. The use of the "SOR filter tool" allowed the outliers cleaning in the point clouds, and proved to be very effective paired with a manual filtering that gives the user full control over what is considered redundant or incorrect. This was an important step because SfM data rarely have homogeneous point densities and small errors in matching could lead numerous outliers that could corrupt subsequent analysis (Smith et al., 2015; Carrivick et al., 2016).

The cleaned point clouds were co-registered using the ICP algorithm. The 3D point cloud of October 2016 was used as a reference because it presented a good precision and accuracy in terms of CPs (0.014 m and 0.018 m respectively, see next Section 4.3.3), and the highest of point cloud density (15221 points/m^2) with the fewest lacking data. In multi-temporal surveys, it was important to delete every possible shift or rotation between final 3D point clouds due to the residual errors (e.g., residual errors of GNSS measures because the GCPs are re-surveyed every time since they could have moved) in each point cloud. Moreover, Westoby et al. (2012) indicated how errors in the co-registration procedure could be linked to the manual identification of ground control points in both point cloud datasets. Victoriano et al. (2018) highlighted that comparability between data sets is a hard task in morphologically complex terrains, such as the mountain regions. In order to cope with these issues, the ICP was applied first in stable zones of the study area such as check dams structures, that were stable and uniform in terms of point density. Micheletti et al. (2015a) also suggested to isolate stable zones and to apply an ICP procedure, improving the quality of change detection in areas where change has occurred.

Next, the multi-temporal clouds were decimated and regularised using ToPCAT. The optimum grid cell size of decimation was assessed through an analysis of topographic complexity lost in a specific zone (Fig. 4.13) of the Moscardo study area (e.g., Brasington et al., 2012). A subset point cloud for this zone was analysed at different grid-sizes (from 0.05 m to 6 m) to obtain various DEMs (e.g., Fig. 4.14), from whose a cross section was extracted to analyse changes on

the topographic profile associated to a loss of topographic complexity (Fig. 4.15). The loss of topographic information, as the grid size of the analyses increases, was clear as can be seen in the cross section A-B presented in Figure 4.15 for two different survey periods.

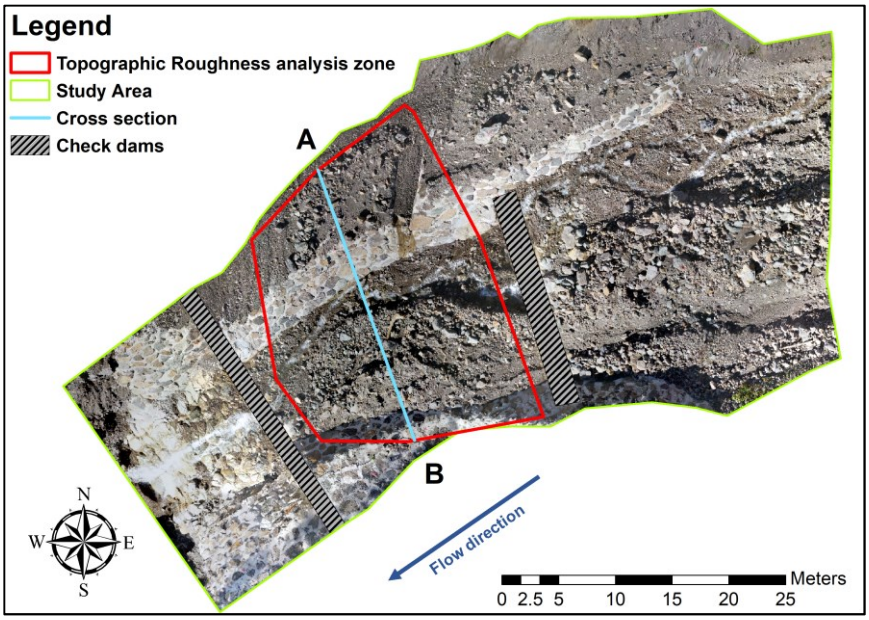

Figure 4.13: Location of the cross section A-B where the profile was extracted a different grid size resolution (Fig. 4.14) and the area where the topographic roughness analysis was performed.

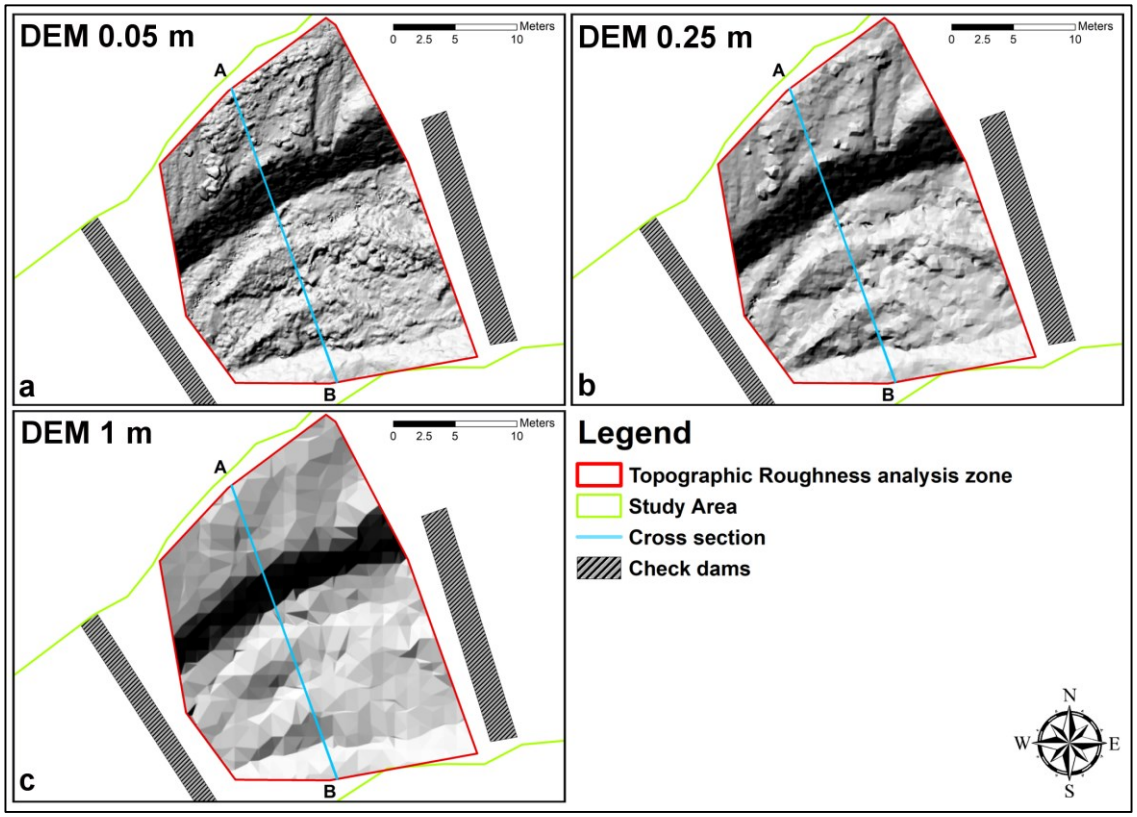

Figure 4.14: Examples of shaded relief map of DEMs at 0.05 m, 0.25 m and 1 m of resolution for the October 2016 survey in the Moscardo study area. The line A-B represents the cross section defined in each DEM.

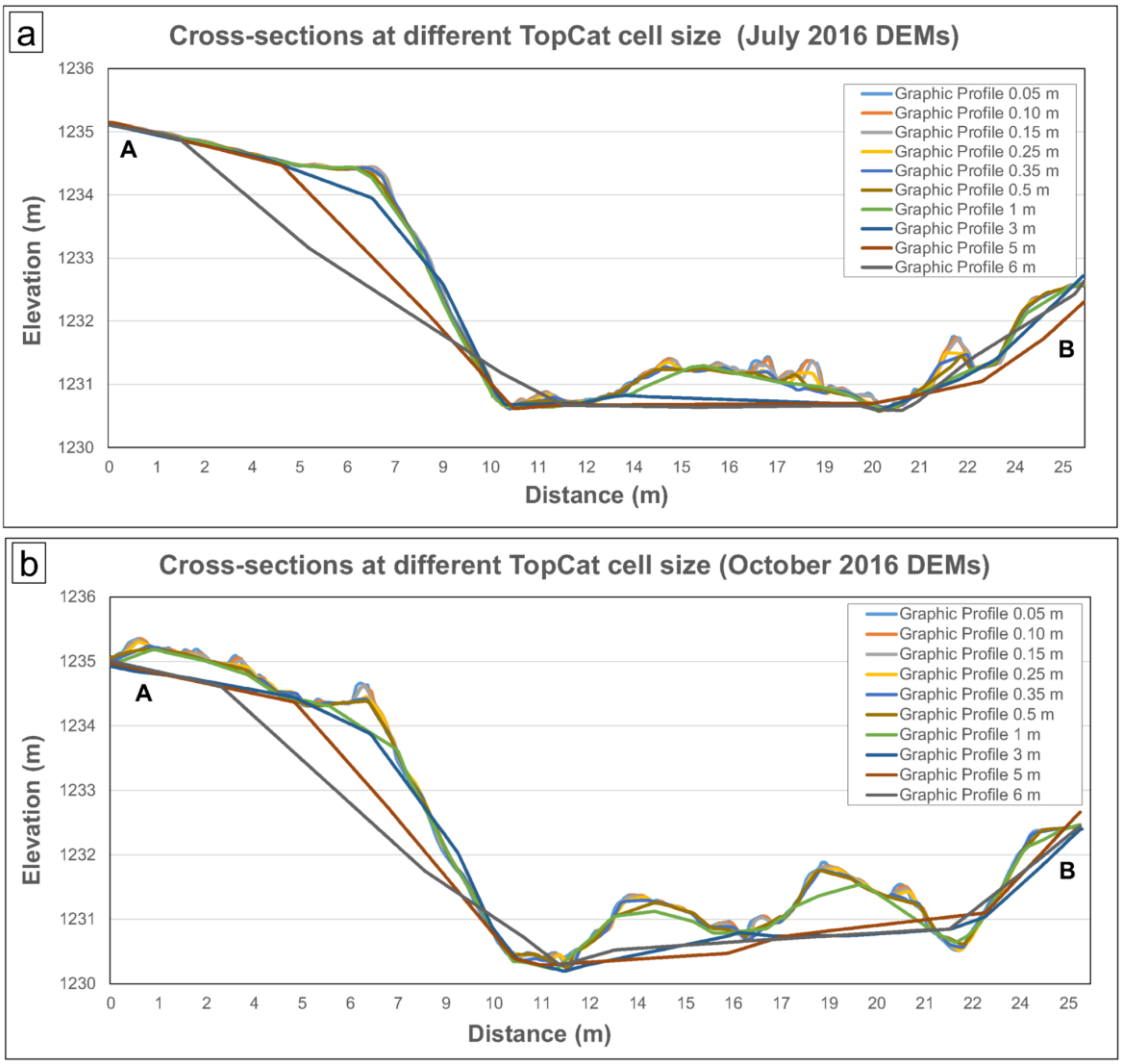

Figure 4.15: Example of cross-sections (shown in Fig. 4.13) obtained changing the grid size for which ToPCAT was applied (increasing from 0.05 m to 6 m) for: (a) July 2016 and (b) October 2016 surveys in the Moscardo study area. Note that, these two examples show also the evident evolution of the channel over the October-July period in 2016.

Finally, the DEMs were used to calculate the surface topographic roughness at multiple grid sizes to statistically demonstrate the loss of topographic complexity (already pointed out in the analyses of the cross-sections, Fig. 4.15). The relationships between the average and standard deviation of topographic roughness with the grid size plotted in Figure 4.16 underline, as expected, a clear scaling pattern. The topographic roughness falls rapidly from 0.05 m to 1 m cell size, whereas a more gradual decrease was observed for resolutions between 1 to 6 m. The ToPCAT grid-size was set to 0.05 m to preserve the maximum available topographic complexity. Point clouds density resulted in about 400 points/m^2 on average after the decimation processes using ToPCAT.

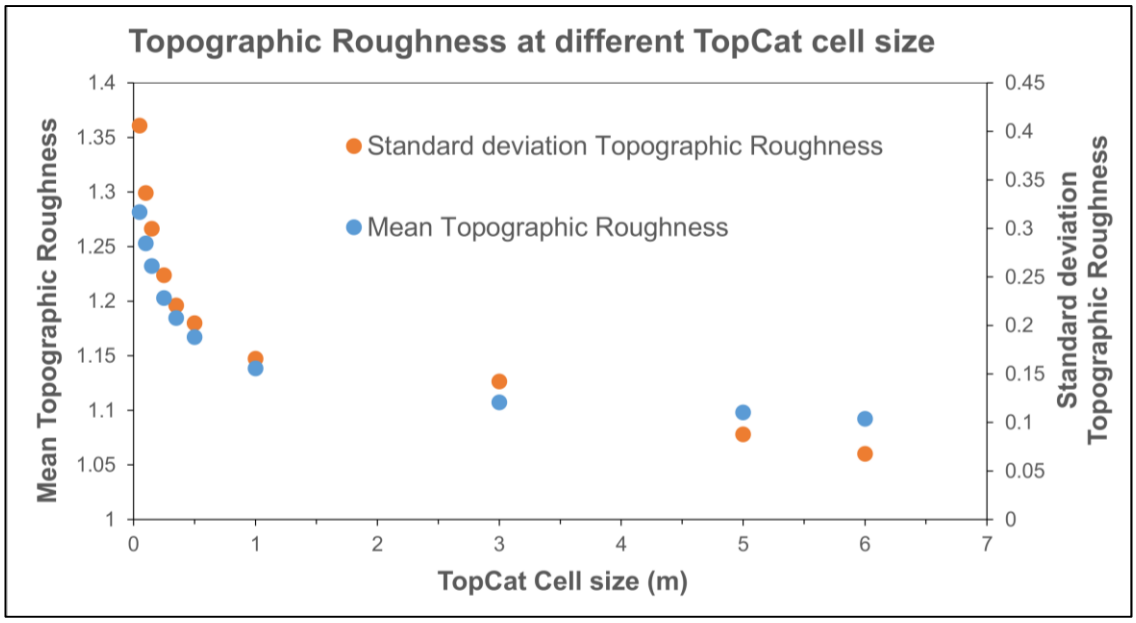

Figure 4.16: Relationships between the average and standard deviation of topographic roughness in relation to the ToPCAT grid size used for the analyses for the October 2016 survey in the Moscardo study area.

The minimum elevation observations within each cell for each multi-temporal point cloud were used to derive the DEMs with a 0.20 m resolution. This choice was based on the topographic roughness analysis, the precision and accuracy assessment of surveys, the uncertainty analysis, and the features of the Moscardo study area.

4.3.3 Data and error analysis

The quality of the 3D point clouds is an important aspect of the workflow as described in Section 3.2.4 and it was estimated through the point's quality assessment of the GCPs and CPs in terms of precision, accuracy and registration error. Table 4.6 summarizes all these errors aspects for each of the surveys.

Table 4.6: Registration errors, precision and accuracy of all point clouds on GCP and CP residuals. The registration errors evaluated the GCPs residuals for georeferencing the point clouds. The standard deviation and the mean value of the CPs residuals assessed the precision and accuracy of the point clouds respectively (Marteau et al., 2017). These errors are provided by the bootstrapping technique applied in Photoscan software.

Point Cloud	Registration error (m): GCP			Point cloud accuracy* (m): CP			Point cloud precision** (m): CP		
	x	y	z	x	y	z	x	y	z
December 2015	0.085	0.085	0.029	0.099	0.094	0.055	0.078	0.093	0.044
June 2016	0.027	0.041	0.016	0.027	0.037	0.018	0.020	0.041	0.013
July 2016	0.023	0.025	0.017	0.018	0.023	0.017	0.013	0.020	0.013
August 2016	0.038	0.027	0.018	0.034	0.031	0.023	0.039	0.025	0.015
October 2016	0.018	0.035	0.018	0.017	0.029	0.018	0.015	0.040	0.014
May 2017	0.019	0.020	0.040	0.015	0.017	0.035	0.013	0.012	0.033
July 2017	0.020	0.025	0.034	0.019	0.023	0.033	0.014	0.014	0.021
August 2017	0.018	0.015	0.030	0.015	0.013	0.027	0.010	0.009	0.018
June 2018	0.035	0.026	0.032	0.029	0.021	0.029	0.020	0.016	0.021
October 2018	0.011	0.023	0.019	0.009	0.017	0.014	0.007	0.017	0.016

*Accuracy estimated as the absolute mean value of the residuals.

**Precision assessed as the standard deviation of residuals.

The errors of the GCPs and CPs, which determine overall SfM survey accuracy (Smith et al., 2015) are all in the magnitude order of centimetres. The bootstrap resampling technique allowed a more detailed assessment of accuracy and precision based on the ground control network. Even so, precision and accuracy can be also examined by surveying extra validation points, additional to the GCP network. Moreover, the results of the bootstrapping technique also allow calculating, for each marker, the mean, maximum and minimum error (e.g., Fig. 4.17). This permit to identify the suspicious markers with the highest errors and to decide if they must be removed due to their inadequate placement or movement.

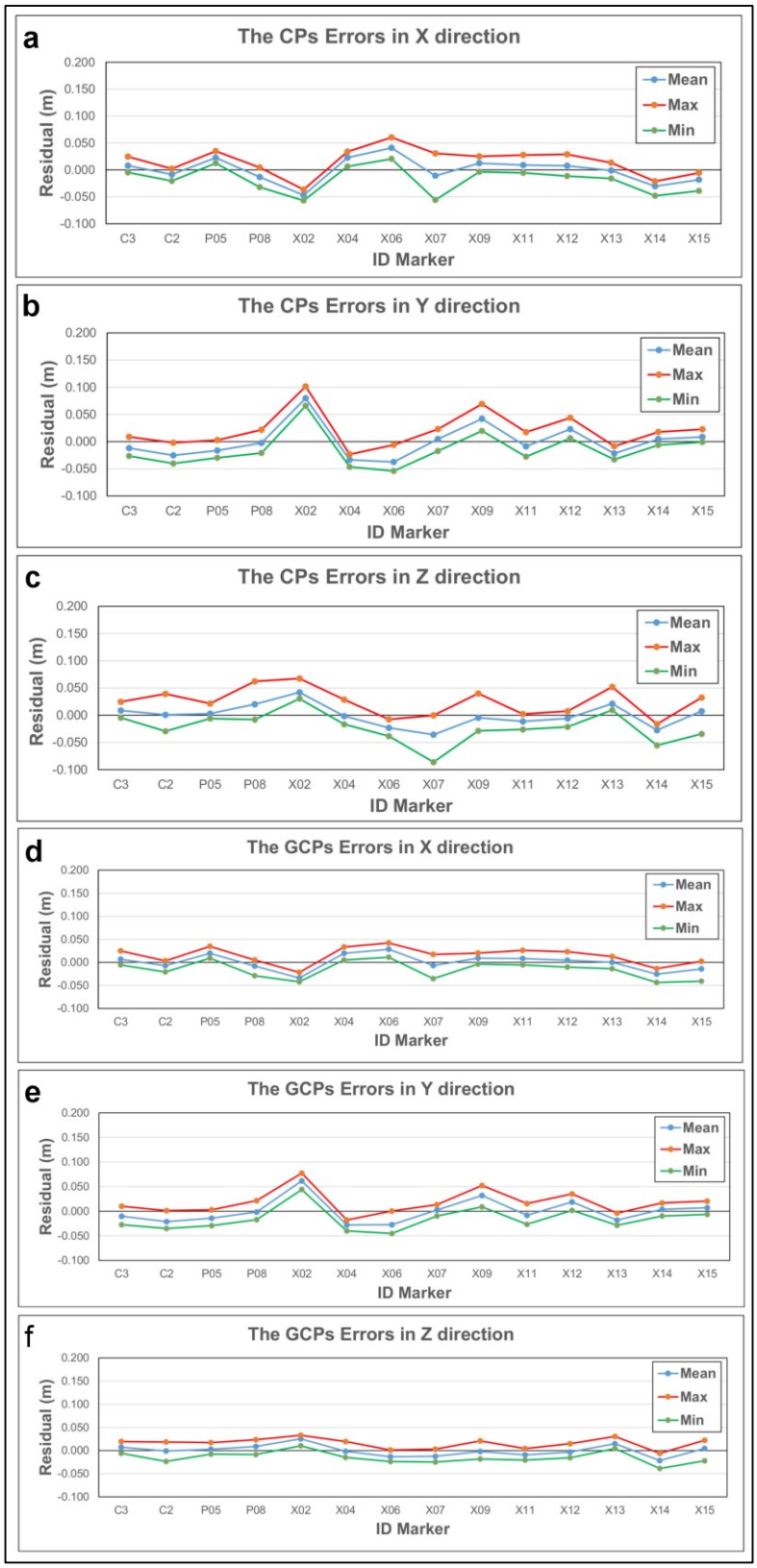

Figure 4.17: Examples of CPs and GCPs errors (mean, maximum and minimum error) in X, Y, Z direction for each marker used in the photogrammetric survey of the July 2016. a) CPs errors in X direction for each marker. b) CPs errors in Y direction for each marker. c) CPs errors in Z direction for each marker. d) GCPs errors in X direction for each marker. e) GCPs errors in Y direction for each marker. f) GCPs errors in Z direction for each marker.

For example, Figure 4.17 shows the CPs and GCPs errors (residuals) of each marker for the X, Y and Z components in the July 2016 survey. This allows evaluating the uncertainty for the different markers used in the photogrammetric survey. In this case, the markers with ID name X02 and X07 presented relatively high CPs errors in each coordinate (Fig. 4.17a, b, c). The analysis of marker distribution map (Fig. 4.10) suggests that the marker X02 was located close to the wet area. Therefore, the surface produced high differences between the real coordinates in this point and the modelled values due to high reflection of the water that is a significant problem for photogrammetry software (Fonstrad et al., 2013; Bemis et al., 2014; Micheletti et al., 2015b; Eltner et al., 2016). Instead, the marker X07 was placed in a point where the elevation component changed a lot in a small space; consequently, these conditions produced high CPs errors of marker placement by the software. In addition, the GCPs residuals for X02 and X07 markers (Fig. 4.17d, e, f) also displayed that these points were not optimal for the quality of the registration process because the errors were slightly high and they were not in line with the trend of the other marker. Therefore, the significant differences between the real coordinates of these points and their estimated values by the software, suggested: (*i*) the removal of these suspicious markers in the 3D model; (*ii*) the improvement of these markers placement in future surveys to reduce the resulting errors in the point cloud generation. In this way, it is possible to draw some considerations about the marker location in the area of interest and to plan the best GCPs position for the future design. Indeed, several papers (e.g., Vericat et al., 2009; James and Robson, 2012; James and Robson, 2014; Piermattei et al., 2015; Smith and Vericat, 2015; James et al., 2017a; Koci et al., 2017; Sanz-Ablanedo et al., 2018) highlighted how the GCPs distribution influences the final quality of the process of georeferencing, as emerged from these results. If the GCPs are well distributed across the study area (not neglecting the margins), they could effectively decrease survey failure and mitigate systematic errors like the 'dome effect', which results from the use of exclusively vertical imagery (James and Robson, 2014; Smith and Vericat, 2015). Moreover, the Monte Carlo approach developed by James et al. (2017a), could help identify minimal GCP deployments for future topographic repeat surveys, thus offering substantially reduced field survey effort. James et al. (2017a) underlined how the needed GCP density will depend on the required project accuracy, the network geometry and the quality of image observations. Indeed, their Monte Carlo approach also enabled to validate the camera models parameters (through appropriate weighting of tie and control point image observations in bundle adjustment) and to enhance error characterisation. These aspects could further improve the developed workflow.

A second error analysis was carried out on stable wide surfaces (check dam structures; Fig. 4.18a) through the M3C2 distance (Tab. 4.7; Fig. 4.18b).

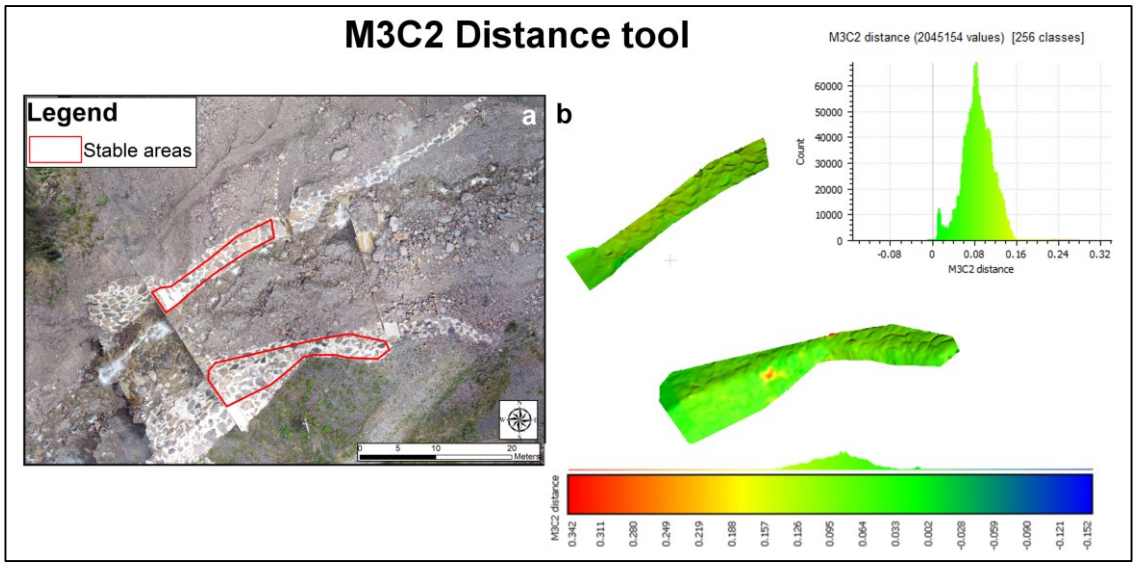

Figure 4.18: Example of the M3C2 tool (distance cloud-to-cloud) implementation. a) The stable zone location in the SfM study area. b) The M3C2 distance map between stable areas of the dense point cloud of July 2018 and December 2015 in CloudCompare software.

The M3C2 distances were also in the magnitude order of centimetres, thus confirming the point quality obtained for the CPs (Tab. 4.6). The cloud-to-cloud comparisons provided a more robust measure of the differences between the two surveys and allow surface-normal differences to be measured (Lague et al., 2013). Some studies (e.g., James and Robson, 2012; Cook, 2017; James et al., 2017b; Eker et al., 2018) compared directly point clouds to assess the errors between two surveys and quantifying topographic change. Working directly on point clouds, especially in stable areas, allow the raw uncertainty definition of surface representation. Such an assessment of uncertainty was particularly relevant in the context of complex geometries where the interpolation process for DEM generation could increase uncertainty for sharp features (Heritage et al., 2009). These analyses could be further examined in depth through the method developed by James et al. (2017b) that enables precision maps to be produced. The standard deviation of M3C2 distance, between two clouds in stable areas, was used as a precision error for the "Data" typology surfaces for the clouds under analysis. For the "No Data" typology, an error of 0.5 m was chosen, while for the typology "Water", the mean water depth was estimated during the surveys to 0.15 m. Vegetation was not present in the study area and, consequently, not considered in the error assessment. For the submerged areas, as stated above, the error assessment could be improved following the works of Woodget et al. (2015) and Dietrich (2017) that assessed the ability of SfM to obtain topography through clear water by applying a refraction correction. However, water depth in the study reach was relatively low, and considering the average depth as the precision in the wetted areas was not far from the range of the errors reported in the literature to correct SfM-based submerged topography. The main surface typologies and their

uncertainty values were identified for each point cloud of the study area (Figure 4.19a), as described in Section 3.2.4. Table 4.8 summarizes the uncertainty values or errors, approximated by excess for a conservative approach, for each surface typology of all point clouds.

Table 4.7: Cloud-to-cloud distance values in the stable zones of Moscardo study area.

M3C2 Distance of Clouds	**Accuracy*** Absolute mean value [mean value]	**Precision****
December 2015 – June 2016	0.044 m [0.024 m]	0.081 m
June 2016 – July 2016	0.034 m [0.007 m]	0.069 m
July 2016 – August 2016	0.016 m [0.003 m]	0.032 m
August 2016 – October 2016	0.020 m [0.010 m]	0.032 m
October 2016 – May 2017	0.005 m [0.009 m]	0.010 m
May 2017 – July 2017	0.015 m [-0.011 m]	0.016 m
July 2017 – August 2017	0.036 m [0.034 m]	0.017 m
August 2017 – June 2018	0.018 m [0.011 m]	0.019 m
June 2018 – October 2018	0.021 m [-0.001 m]	0.026 m
December 2015 – October 2018	0.070 m [0.070 m]	0.032 m

*Accuracy estimated as the absolute mean value of distance. The mean value can be used to assess possible systematic errors.

**Precision assessed as the standard deviation of distance.

Table 4.8: Errors associated with each surface typology of all point clouds. For the "Data" typology, surfaces were chosen the precision errors of the M3C2 distance (Tab. 4.7), while for "No Data" and "Water" typology the uncertainty values were 0.50 m and 0.15 m respectively.

Surface Typology	**Data***	**No Data****	**Water**
December 2015	0.08 m	0.50 m	0.15 m
June 2016	0.07 m	0.50 m	0.15 m
July 2016	0.03 m	0.50 m	0.15 m
August 2016	0.03 m	0.50 m	0.15 m
October 2016	0.01 m	0.50 m	0.15 m
May 2017	0.02 m	0.50 m	0.15 m
July 2017	0.02 m	0.50 m	0.15 m
August 2017	0.03 m	0.50 m	0.15 m
June 2018	0.03 m	0.50 m	0.15 m
October 2018	0.03 m	0.50 m	0.15 m

* This error is based on the M3C2 results (see text for more details).

Figure 4.19b and c show an example of the distribution of the errors in each surface for the July and October 2016 surveys. These errors were combined and propagated to apply a variable *minLoD* (Fig. 4.19d) based on errors typology surfaces as described in Section 3.2.4.

The errors analysis highlights how the quality of 4D-SfM surveys was adequate for investigating topographic changes in the study area.

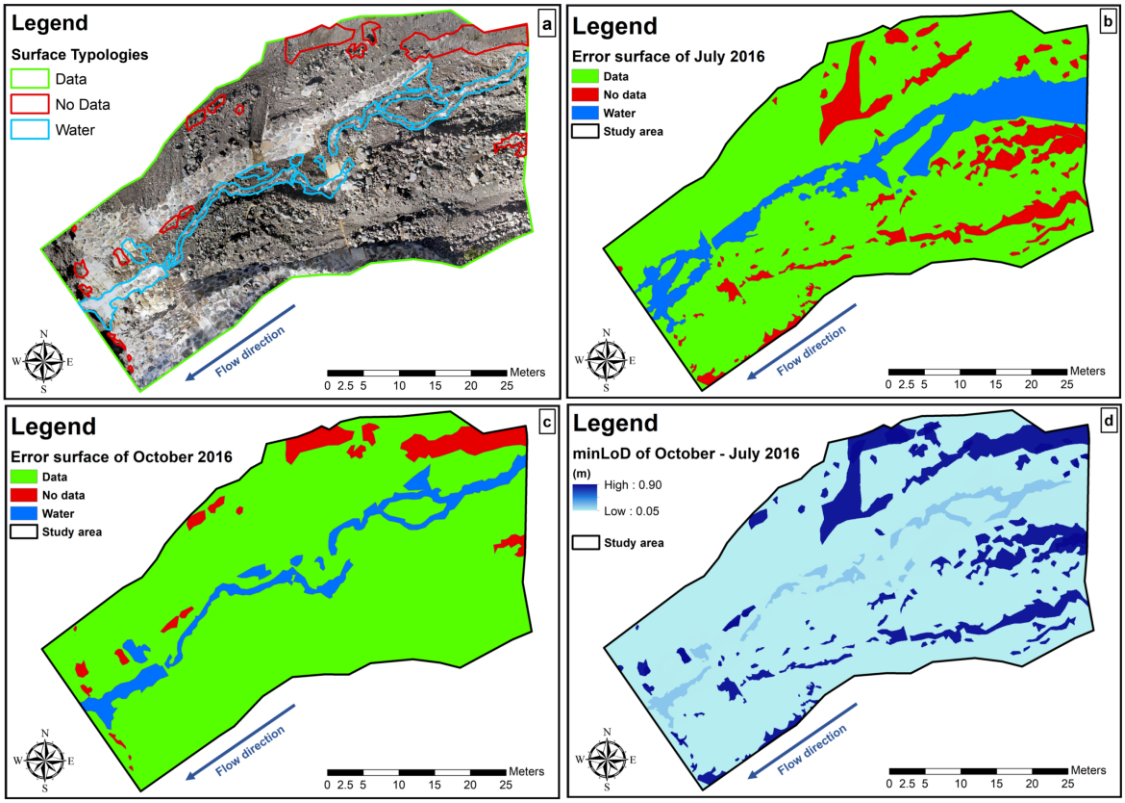

Figure 4.19: The distribution of the errors in each surface for the July and October 2016 surveys. a) Example of the different surface typologies identification for the October 2016 survey in the Moscardo study area. b-c) Examples of rasters representing the errors for each surface typology for the July and October 2016 surveys. d) Example of statistical minLoD raster for the July and October 2016 surveys in the Moscardo study area.

The accuracy of SfM point clouds must be controlled especially in complex topography landscapes (Carrivick et al., 2016; Victoriano et al., 2018) where survey error is uneven across a surface: low error across uniform surfaces with high point density and greater uncertainty associated with breaks of slope and low point density (Wheaton et al., 2010; Milan et al., 2011). Similar outcomes were reported in Schürch et al. (2011) who highlighted how the issues arising from complex surface geometry (e.g., in a river or a debris-flow channel with abrupt changes in slope, aspect, local surface roughness and high local relief) can lead to an increased chance of ambiguous point cloud matching. Moreover, Fonstrad et al. (2013), Micheletti et al. (2015b) and Eltner et al. (2016) argued that transparent (e.g., water), reflective or homogeneous surfaces areas of low image texture can produce poor point clouds. Cook (2017) confirmed that the accuracy and precision of SfM-generated point clouds depend heavily on the characteristics of the measured surface. Therefore, all these errors must be considered in the workflow to produce more realistic spatial representations of topographic changes. In these cases, a distributed error approach was needed to assess volumes of erosion and deposition through DoDs and associated errors.

4.3.4 DoDs and Budget segregation at check dams scale

The error analysis shows that the quality of 4D-SfM surveys was adequate for investigating topographic changes at channel scale by means of DEM differencing. As described in Section 3.2.4 the significance of these changes was evaluated through the *minLoD* that needs to choose a confidence interval *t* (1.28 for 80% CI, 1.96 for 95% CI) for the DoDs thresholding. The most suitable confidence interval for this case of the study was chosen through the result comparison of different DoDs obtained using diverse *t* value. Figure 4.20 shows one DoD of the study reach (based on the surveys carried out in December 2015 and August 2017) used to analyse the DoDs thresholded with diverse confidence interval (see Tab. 4.9 and 4.10). This DoD was chosen as an example because it displayed the greatest net volume difference in the time. The thresholded DoDs were generated using a $t = 1.28$ (80% CI; Fig. 4.20a) and a $t = 1.96$ (95% CI; Fig. 4.20b). The total volume of erosion and deposition, together with the net volume change, are given in Table 4.9. Figure 4.20c shows the raw DoD (without the application of a *minLoD*). By taking a more or a less conservative *t* value, the number of cells considered as real changes, as well as the estimate of net change, slightly vary and the differences are visible not only visually in Figure 4.20 but also in the numerical terms in Table 4.9. Even so, in this case, $t = 1.96$ (95% CI) was used as a more restrictive approach, but the change of the confidence interval ($t = 1.28$) not affected excessively the volume results. The differences between thresholded and raw DoD are also not huge but highlight how the volume estimates are subject to uncertainties that, if they are not considered, could become significant and could have a certain weight on the volume estimates. Furthermore, the small differences also depend on the high quality of the data in relation to the magnitude of change. Indeed, when the analysed datasets are characterized by a spatial resolution in the range of 1-2 meters for carrying out analysis at the regional/catchment scale, the differences can be higher (e.g., Cavalli et al., 2017). Moreover, these minimum differences between thresholded DoDs (both DoD with $t = 1.28$ and DoD with $t = 1.96$) and raw DoD prove how the developed workflow is sturdy and allows the achievement of high quality and coherent data from SfM surveys. The DoDs obtained using a 95% CI for all the analysed periods (December 2015 – October 2018) are presented in Figure 4.21, whereas the Table 4.10 shows the total volume of erosion and deposition and the net volume change for all the DoDs.

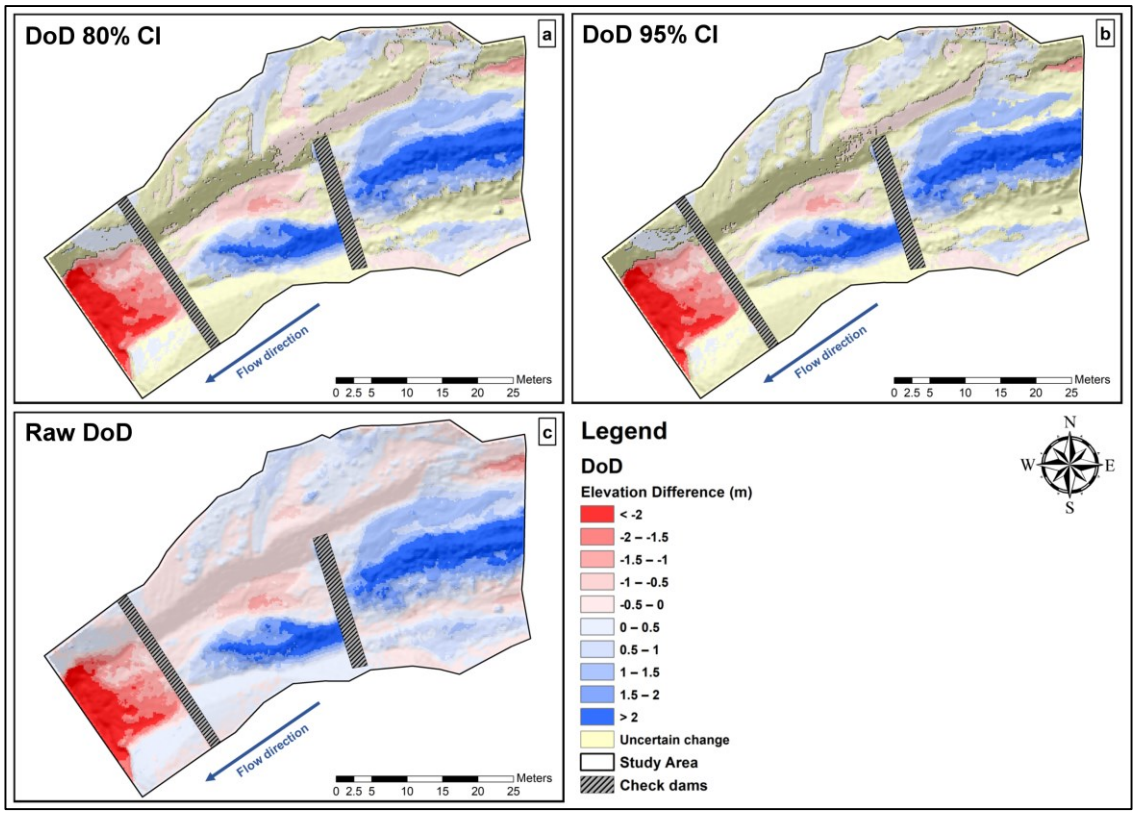

Figure 4.20: The DoDs (August 2017 - December 2015) of the study reach used to analyse the thresholding with diverse confidence interval. a) DoD thresholded used t = 1.28 (80% CI). b) DoD thresholded used t = 1.96 (95% CI). c) DoD without threshold.

*Table 4.9: Total volume of erosion and deposition and the net volume change, for the thresholded DoDs at different confidence intervals and the same DoD without threshold for the survey of December 2015 and August 2017. * Note that the ± volumes were estimated based on the errors associated with each typology of the surface ("Dry zones", "Water" and "Shaded" areas) described in Section 3.2.4*

DoD August 2017 - December 2015	**Thresholded DoD: minLoD**		**Raw DoD**
	80% CI (t > 1.28)	**95% CI (t > 1.96)**	
Erosion (m^3)*	428 ± 76	408 ± 63	469
Deposition (m^3)*	894 ± 129	845 ± 99	934
Net Volume difference (m^3)*	466 ± 149	437 ± 118	464

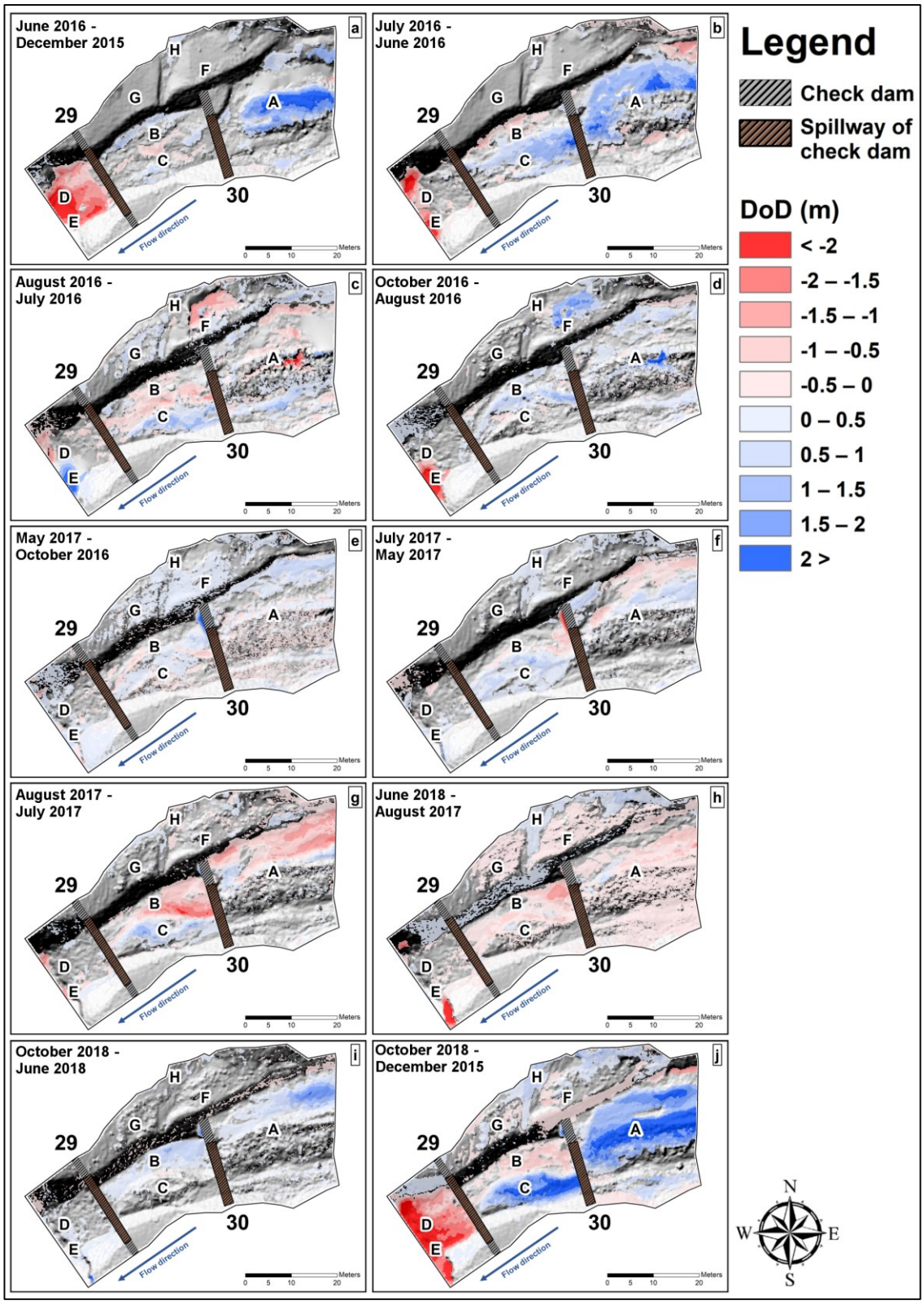

Figure 4.21: Sequence of DoD: a) DoD June 2016 - December 2015 surveys. b) DoD July 2016 - June 2016. c) DoD August 2016-July 2016. d) DoD October 2016 - August 2016. e) DoD May 2017 - October 2016. f) DoD July 2017 – May 2017. g) DoD August 2017 - July 2017. h) DoD June 2018 - August 2017. i) DoD October 2018 - June 2018. j) DoD October 2018 - December 2015. The uppercase letters (A, B, C, D, E, F, G, H) identify the focus zone where the morphological changes were analysed in the Section 4.3.5.

Table 4.10: The total volume of erosion, deposition and net volume changes from the different DoDs of whole study area (2015 m²) . The ± uncertainty of volumes are estimated considering a spatially distributed minLoD based on the typology of error surface presented in the study area ("Dry zones", "Water" and "Shaded" areas) described in Section 3.2.4.*

	Thresholded DoD estimate (95% CI)			
Compared dates	**Erosion (m^3)***	**Deposition (m^3)***	**Net Volume difference (m^3)***	**Net deposition/erosion (m)**
23 June 2016 - 15 December 2015	241 ± 45	296 ± 62	55 ± 77	0.03 ± 0.04
22 July 2016 – 23 June 2016	134 ± 30	419 ± 79	285 ± 84	0.14 ± 0.04
09 August 2016 – 22 July 2016	172 ± 28	189 ± 33	17 ± 43	0.01 ± 0.02
28 October 2016 – 09 August 2016	72 ± 18	187 ± 28	115 ± 33	0.06 ± 0.02
30 May 2017 – 28 October 2016	37 ± 5	111 ± 14	74 ± 15	0.04 ± 0.01
20 July 2017 – 30 May 2017	64 ± 12	118 ± 17	54 ± 21	0.03 ± 0.01
31 August 2017 – 20 July 2017	266 ± 33	77 ± 9	-189 ± 34	-0.09 ± 0.02
19 June 2018 - 31 August 2017	218 ± 36	45 ± 7	-173 ± 37	-0.08 ± 0.02
09 October 2018 - 19 June 2018	10 ± 3	179 ± 32	168 ± 32	0.08 ± 0.02
09 October 2018 - 15 December 2015	435 ± 63	870 ± 100	435 ± 119	0.22 ± 0.06

In addition, the budget segregation function of GCD (see Section 3.2.4.) enabled the DoDs segmentation into specific areas of interest. This enables (*i*) to have the DoDs and the volumetric estimates for each of the specific areas, and (*ii*) to study erosional and depositional processes in different areas and try to understand the mechanisms reshaping them (*iii*) to identify potential local processes that can damage the functionality of these infrastructures. Figure 4.22a shows the main areas of interest used in this study: the right bank area, the zone upstream, and the areas between and downstream of the check dams. A second segmentation aims to study the contribution of the right slope in the debris-flow channel: to this purpose, the study area was divided into the right bank, right slope, and channel (Fig. 4.22b). Finally, to evaluate the right slope input in the debris-flow channel, the DoDs was segmented into the debris-flow zone and right slope area (Fig. 4.22c).

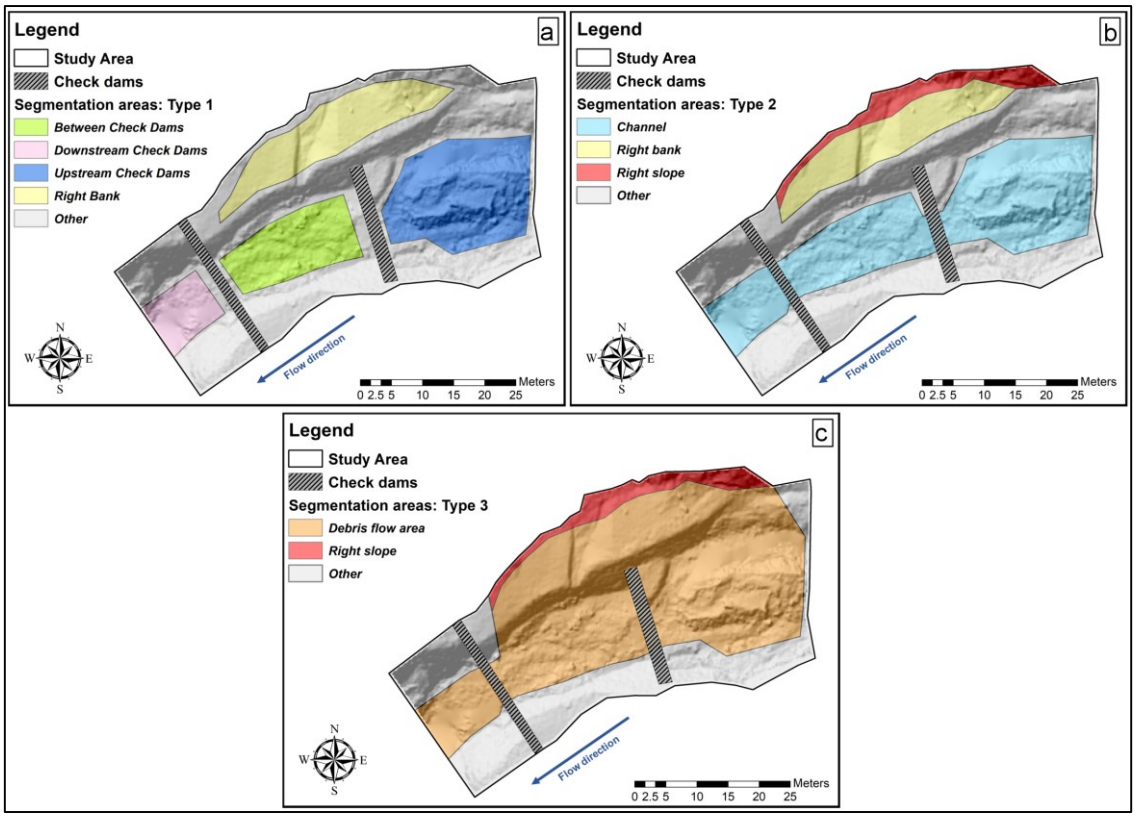

Figure 4.22: Budget segregation zones in the study area. a) The area is divided into 4 zones: right bank, upstream, and areas between and downstream the check dams. b) The area is divided into 3 zones: the right bank, the right slope and the channel. c) The area is divided into 2 zones: the debris-flow zone and the right slope.

The DoD of August 2017 - December 2015 was again chosen to show an example of the budget segregation tool (Fig. 4.23a, b, c, d, e). The volumes of erosion and deposition in different zones with the net volume change for DoD August 2017 - December 2015 and DoD October 2018 - December 2015, obtained through the budget segregation, are given in Table 4.11. The budget segregation helped characterizing the spatial distribution and magnitude of geomorphic changes, leading to a better understanding of control structure effect on the debris-flow dynamics in the study area.

*Table 4.11: Example of the total volume of erosion, deposition, and the net volume change, for the thresholded DoDs (95 % CI) in the DoD August 2017- December 2015 and DoD October 2018 - December 2015 for the segregation area: right bank, upstream, between and downstream the check dams (Fig. 4.22a). *Note that the ± volumes were estimated based on the errors associated with each typology of the surface ("Dry zones", "Water" and "Shaded" areas) described in Section 2.3.4*

	Thresholded DoD (95% CI)					
	DoD August 2017 - December 2015			**DoD October 2018 - December 2015**		
Zone	**Erosion (m^3)***	**Deposition (m^3)***	**Net Volume difference (m^3)***	**Erosion (m^3)***	**Deposition (m^3)***	**Net Volume difference (m^3)***
Right bank	7 ± 2	42 ± 6	35 ± 6	7 ± 2	32 ± 64	26 ± 4
Upstream check dams	0	460 ± 51	460 ± 51	0	468 ± 53	469 ± 53
Between check dams	39 ± 7	140 ± 10	101 ± 12	32 ± 8	126 ± 9	93 ± 12
Downstream check dams	209 ± 24	0	-209 ± 24	202 ± 24	0	-202 ± 24
Other	152 ± 31	202 ± 32	50 ± 44	193 ± 30	243 ± 35	49 ± 47

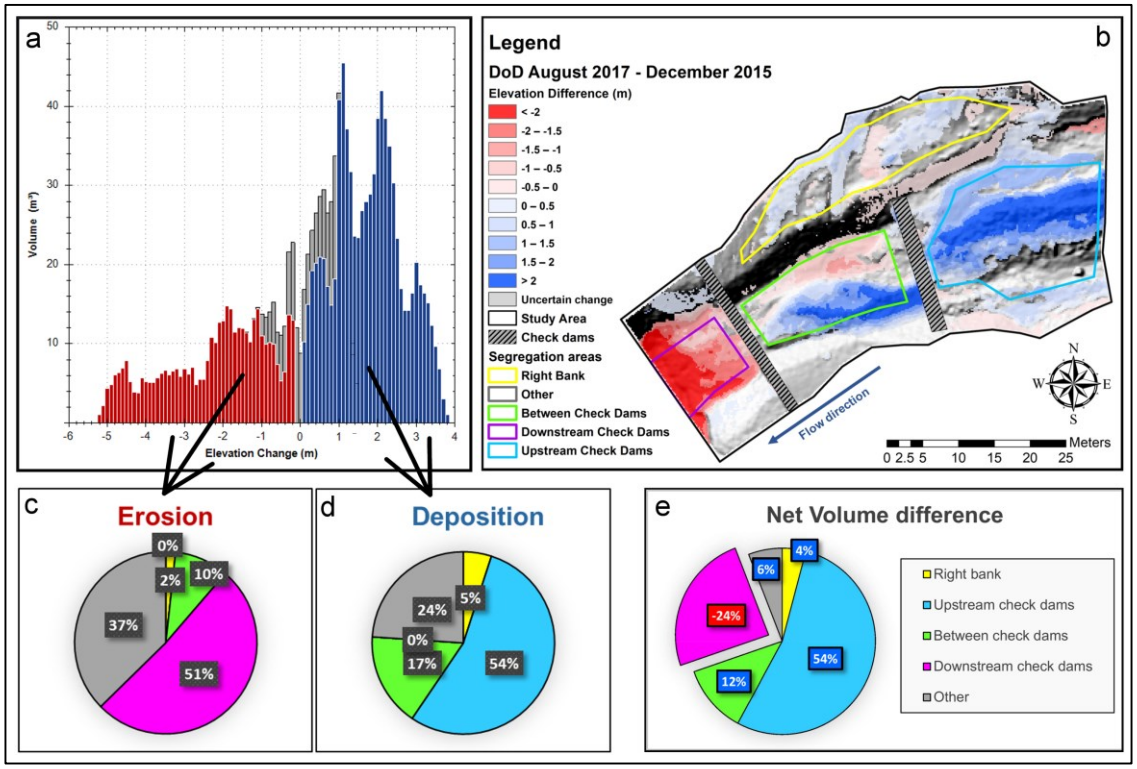

Figure 4.23: Budget segregation analysis for the DoD August 2017 - December 2015. a) Bar chart of DoD elevation change distribution (erosion volume in red, deposition volume in blue, grey shaded areas represent values below the confidence threshold) for the DoD of December 2015 and August 2017. b) DoD August 2017-December 2015 (thresholded, 95% CI) within the budget segregation zones in the study area: right bank, upstream, and between and downstream the check dams. c) Pie chart of relative proportions of erosion (observed in a) for each budget segregation zone. d) Pie chart of relative proportions of deposition (observed in part a) for each budget segregation zone. e) Pie chart of relative proportions of net volume difference for each budget segregation zone.

The developed workflow proves to be adequate for acquiring 4D-HRT from SfM in a rugged environment like a debris-flow channel. However, the limited ability to predetermine data quality in SfM surveys (which can only be evaluated after the field data acquisition) is perhaps the biggest weakness in the approach (Smith et al., 2015). Therefore, this work highlights how the precision in 4D-SfM surveys could only be guaranteed through a careful planning of appropriate survey, an accurate data post-processing, and an uncertainty assessment. Often user-friendly SfM software does not promote a critical analysis of the processing parameters involved, preventing from fully understanding the underlying sources of error in geomorphological studies (James et al. 2017a). Furthermore, moving beyond such a 'black box' SfM approach, an understanding of the full SfM workflow implemented is useful to identify and minimize potential sources of error in the topographic data (Smith et al. 2015). This could further improve a technique that has already proved to be revolutionary, making available to end-users a useful tool with standardized data-acquisition, processing, and post-processing steps. The recent proliferation of SfM validation studies (e.g., James and Robson 2012; Smith et al. 2015; Smith and Vericat 2015; Clapuyt et al. 2016; Cook 2017; James et al. 2017a; James et al. 2017b; Marteau et al. 2017;) calls for the need for an improved coordination and standardisation of such efforts. The present work represents, therefore, another evidence that SfM photogrammetry is a robust and valuable tool for the evaluation of geomorphological changes at detailed spatial and temporal scale.

4.3.5 The sediment dynamic at check dams scale

During the SfM surveys in the upper part of the catchment, six events were recorded at the monitoring station between 2015 and 2018 (Tab. 4.1). Since the monitoring system is located on the alluvial fan (i.e., downstream of the SfM study area; see Fig. 2.4 and Fig. 4.7), debris-flow volumes measured here cannot be directly compared with the volumes estimated by the multi-temporal DEMs obtained from SfM surveys. Discharge and volume data in Table 4.1, however, provide an indication of the debris-flow magnitude, which can be useful for interpreting topographic changes documented at the SfM study site.

The DoD results show an evident pattern of deposition upstream of the check dams (Fig. 4.21j-zone A and C) suggesting that the new check dams effectively stored sediment transported by the debris flows. In addition, Figure 4.24 shows some qualitative information pointing out the sedimentation of debris upstream the check dam.

Figure 4.24: Sediment deposits at the site of the upper check dam (n. 30). a) 15 December 2015. b) 22 July 2016. c) 20 July 2017. d) 19 July 2018.

Overall, during the three years of observations, a total volume of 870 m^3 of debris was deposited upstream of the check dams, while 435 m^3 were eroded (Tab. 4.10). It must be noted that this is a minimum estimate since the values are computed from two surveys, and they do not take into account the volumes eroded and deposited between the two snapshots. The net volume difference shows a deposition of 435 m^3 while the area just downstream the lowest check dam features an evident erosion pattern (around 202 m^3; Fig. 4.21j-zone D). This pattern has been observed in previous works (e.g. Lenzi and Comiti, 2003; Boix-Fayos et al., 2008; García-Ruiz et al., 2013; Piton and Recking, 2014) and is actively contributing to the progressive instability of the check dam itself.

The debris-flow events caused important morphological changes between 2015-2018 on the entire reach, where significant erosion processes were evident especially downstream of the lower check dam (e.g., Fig. 4.21a, b, d and j-zone D and E), while deposition patterns were clearly observed upstream of the torrent control works (e.g., Fig. 4.21a, b, d, i and j-zone A). The area between the two check dams showed a prevalence of deposition on the left side of the channel and erosion in the right one. This spatial pattern appears in several DoDs (e.g., Fig. 4.21c, g, j-zone B and C) and could be ascribed to the dynamics of the flow moving to the right side of the channel, thus favouring erosion there, whereas deposition occurred on the left side. However, the deposited

material could derive also from the right slope above the channel. All these processes can be investigated in detail through the budget segregation analysis (Fig. 4.22).

The study of the first debris flow after the check dam construction (16 June 2016), showed deposition of about 215 m^3 upstream (Fig. 4.21a-zone A) and a significant erosion area downstream of the lowermost check dam (around 158 m^3; Fig. 4.21a-zone D). The upstream deposition process was favoured by the inherent function of the check dams just after the construction: sediment trapping and decreasing of slope. The erosion downstream resulted from the power of the turbulent flow dissipating the energy in the tumbling-flow (Piton and Recking, 2017) that was displaced downstream resulting from the construction of the new hydraulic control works. Indeed, the flow at the toe of check dams can become even more erosive because it often consists of clear water with only suspended sediment. Important erosion was not observed downstream of the upper check-dam. This is due to *i*) the lower stream slope between the two check dams (30% compared to an average stream slope of 55% for the whole study area), *ii*) the absence of an important tumbling flow due to the low height (1.5 m) of the upper check-dam, and *iii*) the lower check dam that acts as a subsidiary dam. Moreover, the results show that from the first survey of December 2015 until July 2016 the right slope supplied the channel with roughly 7 m^3 of sediment (value assessed from the budget segmentation; Fig. 4.22c) because a retention net was installed on the slope to hold the eroded material (Fig. 4.21a-zone H).

The debris flows of 11 and 13 July 2016 filled the area upstream of the check dams almost completely (Fig. 4.21b-zone A and C), with 419 m^3 of sediment, while the material present at the foot of the lowest check dam (Fig. 4.21b-zone D) was moved further downstream. Here the erosion process decreased due to the resistance of the check dam foundation. Such excavations, however, could undermine the stability of the check dam and the channel banks over time. Indeed, after the debris flow of 22 July 2016 (Fig. 4.21c), which was a significant magnitude, the erosion processes provoked a partial collapse of the lower slope of the left bank, producing a deposit of 30 m^3 (Fig. 4.21c-zones E). The deposit was consequently eroded at the foot (35 m^3) and the sediment was removed by the streamflow (Fig. 4.21d-zones E). However, the area upstream of the upper check dam once filled, was mainly affected by erosion processes after above mentioned the debris flow (Fig. 4.21c-zone A), which also scoured and created a deposit (15 m^3) on the top of the right bank (Fig. 4.21c-zone G), whereas previous events flowed within the main channel cross section. Therefore, the sediment flowing around the upstream check dam on the right wing had already been damaged in the past for the same reason (Fig. 4.21c-zone F). This produced important changes in the right bank area, with 36 m^3 of erosion and 15 m^3 of deposition, whereas the right slope contributed to a total net volume difference of around 1 m^3. During this event, the erosion and deposition processes were almost balanced in terms of quantity, considering the total net volume difference (Tab. 4.10 – DoD August 2016 - July 2016).

In the period between August-October 2016, the area upstream of the first check dam experienced deposition again (Fig. 4.21d-zone A), whereas erosion phenomena were observed in the most downstream sector (Fig. 4.21d-zone E).

Throughout the wintertime and the spring, from October 2016 to May 2017 (Fig. 4.21e) rather minor morphological changes in the study area were triggered by relatively moderate rainstorms and by snowmelt runoff. The right bank was mainly affected by deposition processes resulting in a volume of 8 m^3 (Fig. 4.21e-zone G and F) while 3 m^3 (Fig. 4.21e-zone H) of material come from the slope. The sediment supplied from the right slope increased after a partial failure of the retention net, as it arises from the surveys of October 2016 to July 2017 where the total deposited material was around 13 m^3 in this area (Fig. 4.21e, f-zone H).

The debris flows pattern of 2017 (Fig. 4.21e, f) shows a continuity in terms of the spatial path: outflanking of the upstream check dam on the right (Fig. 4.21e, f zone F and G) and slightly higher deposition than erosion processes. This until the debris flows registered in August 2017 (6 and 10 August 2017, Fig. 4.21g), which have scoured much of the material deposited upstream of the check dams up until now. The volume of erosion is around 266 m^3 and in this case, the debris flow flowed around the upstream check dam on the right wing one more time (Fig. 4.21g-zone F and G). The sediment is currently deposited on the left part of the channel (Fig. 4.21g-zone C) while scouring affects the right one (Fig. 4.21g-zone B). The last debris flow, recorded on 12 June 2018, caused a widespread erosion (520 m^3; Fig. 4.21h) especially upstream the check dams and on the right bank where the outflanking of the upstream check dam continued. Therefore, part of the material stored up to now upstream the check dams flowed in large quantities downstream. Subsequently, during the summer of 2018, other material was deposited upstream of the check dams along the paths defined by the debris-flow scouring of June 2018 (Fig. 4.21i-zone A and B).

All these processes highlight the presence of scour-and-fill cycles as described by Berger et al. (2011) and Theule et al. (2015). Overall, the results of the budget segregation using the different areas depicted in Figure 4.22c indicate that the right slope contributed to a positive total net volume difference of about 33 m^3 in the debris-flow channel from 2015 to 2018.

The results indicated that the check dams considerably modified sediment dynamics in the study area but their performance cannot be considered satisfactory for three main reasons:

(*i*) The stream flowed around the upstream check dam (n. 30; Fig. 4.24) on the right wing; this effect was further enhanced by the sediment deposition on the left side, caused by a reduction of the slope due to the presence of the check dam. This deposit is actively driving the stream toward the right slope. This shift of the flow can increase the hillslope-channel coupling because the stream can trigger the slope foot erosion and can activate a shallow landslide. This possible

sediment source area can further increase the debris volumes entrained and transported. Therefore, this torrent control works can hardly help to stabilize the right bank side of the reach.

(*ii*) Local scouring, due to energy dissipation and erosion observed downstream of the check dams (n. 29; Fig. 4.25a and b) after the debris-flow events might undermine the stability of the hydraulic control works (Comiti et al., 2013; Piton and Recking, 2016; Victoriano et al., 2018) decreasing their functionality. The foundation of the downstream check dam already showed the first signs of collapse two years after its construction. This check dams might follow the same fate of the check dams (n. 28; Fig. 4.3d) located 30 m further downstream, wrecked by debris flows in the recent past (Fig. 4.25a).

Figure 4.25: The erosion processes observed downstream of the lower check dams (n. 29). a) The erosion in 2016 after the debris-flow events. Another check dam (n. 28; Fig. 4.3d) located 30 m further downstream, destroyed by debris flows in the recent past, is also visible (red arrow). b) Local scouring and erosion observed in June 2018 that undermined the stability of the hydraulic control works.

In the case of the check dam collapse, the release of the stored material would cause an increase of debris-flow volume, resulting in increased hazard downstream (Batalla and Sala, 1995; Benito et al., 1998; Dell'Agnese et al., 2013; Mazzorana et al., 2014; Piton et al., 2016).

(*iii*) The reduction of a reach slope was not sufficient to allow control of channel incision, indeed, erosion processes were active also in the reach. Furthermore, check dam characteristics reveal their unsuitability for retaining large volumes, although they effectively stopped a small amount of the material transported by the debris flows. Indeed, their storage areas were completely filled in only two years and the future events will flow downstream along preferential paths defined by the torrent control works and by the morphology of debris-flow deposits. In addition, the topographic features of the studied channel reach, with strong lateral confinement, contribute to the failure to store relevant volumes of sediment, in spite of the presence of the check dams. Although the deposits locally attained relevant thickness (Fig. 4.24), the deposited volumes were small (net deposition of 435 m^3, corresponding to an average depth of 0.22 m from December 2015 to October 2018). Moreover, debris-flow lobes deposited upstream of the check dams and the material eroded from the right slope can act as sediment sources further increasing

downstream debris-flow magnitude. This result provides useful information for the check dam design and for the choice of its location if the structure has to be rebuilt. Moreover, the quantification of involved sediment volumes allows an adequate design to avoid flow over and around the right wing. The optimization of check dam location is fundamental for debris-flow control (Remaître et al., 2008; Remaître and Malet, 2013) therefore, sediment flow paths and erodibility of the banks should be considered. However, the choice of check dam site must be made by evaluating the accessibility issues for inspection and maintenance, the stability of surrounding slopes, and cost-benefit concerns (Osti and Egashira, 2008). Furthermore, the risk of foundation undermining, which may lead to the failure of the lower check dam (n. 29; Fig. 4.25b) due to the local scouring process, can be lowered through a reliable prediction of the maximum scour depth downstream of the structure. A proper check dam design cannot overlook this aspect that can be predicted by an empirical model (Comiti et al., 2013) calibrated through the debris-flow monitoring and volume quantification of the scouring process. Although DoDs estimations can integrate theoretical and numerical approaches, field investigations are also important to ascertain the condition and functionality of the realized constructions after the interaction with debris flows, because hydraulic control works are prone to be damaged throughout their lifecycle by the same processes they should mitigate (Mazzorana et al., 2008). As an example, DoDs volumes enabled Victoriano et al. (2018) to quantify erosion downstream flexible ring-net barriers along a debris flow channel and these data were of fundamental interest for prioritizing the maintenance and future management of the structures. It is worth noting that, in terms of the response of control measures to debris flows, this study found similar results with respect to our research.

In addition, the knowledge of the interaction between hydraulic control works and sediment dynamics at a detailed scale can allow the improvement of future planning and decisions on debris-flow management strategies at the catchment scale. While the mere recognition of the patterns of erosion and deposition in debris-flow channels equipped with check dams can be performed by means of visual inspections, quantitative 4D-data enable comparison of the design of hydraulic control works with the real effects of debris flows of different magnitudes in the Moscardo catchment. For example, if we consider that only three years after the check dams building, the studied reach started to act as a sediment source and the net sediment budget resulted in the range of 300-500 m^3, it is possible to extrapolate these values to the entire Moscardo torrent. Indeed, considering the net sediment budget of the channel as representative of the full storage capacity of the controlled reach, a rough estimate of the total storage volume resulting from the regulation of the entire main channel would show a sediment retention in the range of 11000-20000 m^3, which is equivalent to one single debris-flow event recorded in Table 4.1.

4.4 LiDAR data

4.4.1 Co-registration processes

As mentioned in the method chapter, a robust pre-processing procedure finalized to the alignment of the point clouds and DEMs was deemed necessary to obtain reliable results for the analysis at the catchment scale (Section B to E in Fig. 3.2). Figure 4.26 shows that important differences between DoDs arise without point clouds and DEMs pre-processing (Raw DoDs; Fig. 4.26a, c, e) and DoDs derived from co-registered surveys (DoDs Co-registered; Fig. 4.26b, d, f). The impact of the co-registration operation was clearly evident on erosion and deposition patterns. Without co-registration of the data sets, the western part of the catchment displayed a substantial deposition, while the eastern part was characterized by erosion in 2013-2009 DoD (Fig. 4.26c) and 2013-2003 DoD (Fig. 4.26e). This was the result of the not optimal alignment between the LiDAR surveys, while, after the co-registration steps, the anomalous trends of deposition and erosion processes clearly decreased in 2013-2009 DoD (Fig. 4.26d) and 2013-2003 DoD (Fig. 4.26f). Instead, the Raw 2009-2003 DoD (Fig. 4.26a) shows fewer trends of erosion and deposition patterns than the co-registered 2009-2003 DoD (Fig. 4.26b). This result depended on the choice of the reference survey used in the co-registration process. The point cloud and DEM of 2013 were used as references during point cloud alignments and DEM co-registrations respectively. Therefore, the quality of alignment between the surveys 2003-2013 and 2009-2013 was increased whereas the congruence between 2003-2009 data slightly decreased. This can happen when (*i*) the surveys are very different in terms of quality (point cloud density, accuracy, precision), (*ii*) the topography is complex as in the Moscardo catchment and (*iii*) the reference point cloud has small errors that can slightly deviate the registration process. The co-registration process can cause secondary misalignments or shifts when the point clouds and DEM, not chosen as references surveys (i.e., 2003 and 2009), were compared because the identified ICP matrix may not be optimal for this specific task. However, this slight misalignment was acceptable and can be reduced through the use of a *minLoD* that takes into account possible errors.

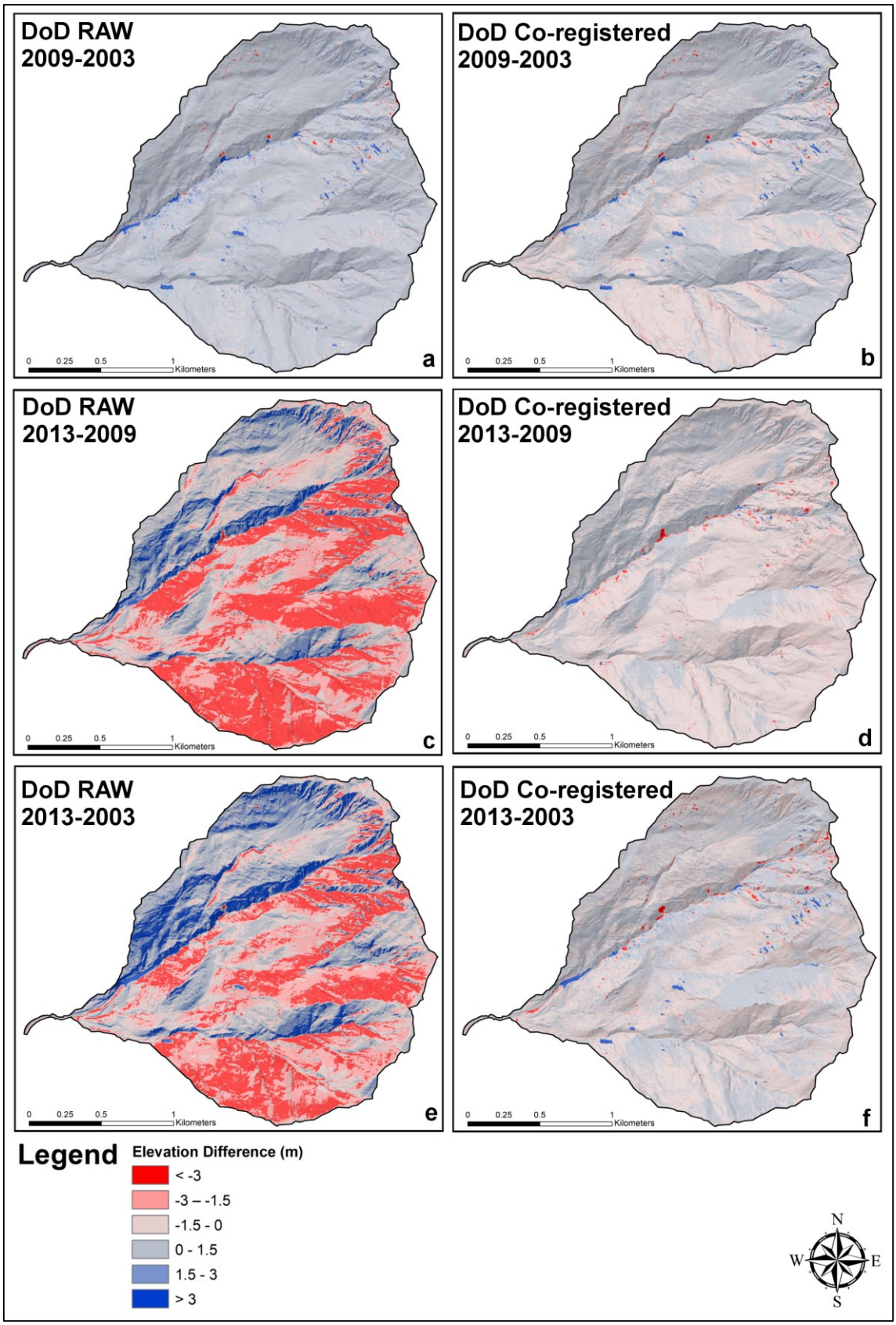

Figure 4.26: The comparison between Raw DoDs (obtained from DEMs without co-registration) and DoDs derived from the co-registered DEMs. a) DoD 2009-2003 obtained without DEM co-registration process. b) DoD 2009-2003

obtained from co-registered DEMs. c) DoD 2013-2009 obtained without DEM co-registration process. d) DoD 2013-2009 obtained from co-registered DEMs. e) DoD 2013-2003 obtained without DEM co-registration process. f) DoD 2013-2003 obtained from co-registered DEMs.

The results and the effectiveness of point cloud co-registration process were confirmed by the values of M3C2 distance tool applied to stable areas of the point clouds as described in Section 3.3.2. Table 4.12 shows the cloud to cloud distance between stable areas in the cloud without co-registration process ("Raw clouds"), after the application of Align tool and ICP algorithm of CloudCompare. The accuracy and precision of point cloud considerably increased after the co-registration steps.

Table 4.12: Cloud-to-cloud distance values in the stable zones of Moscardo catchment.

Clouds of stable areas	**Raw clouds**		**Clouds after Align (Point Pair Picking) tool**		**Clouds after ICP**	
M3C2 distance	**Accuracy*** absolute mean value [mean value] **(m)**	**Precision** (m)**	**Accuracy*** absolute mean value [mean value] **(m)**	**Precision** (m)**	**Accuracy*** absolute mean value [mean value] **(m)**	**Precision** (m)**
2013-2009	0.77 [0.47]	0.86	0.5 [-0.47]	0.45	0.30 [0.05]	0.39
2013-2003	1.13 [0.83]	0.95	0.47 [0.06]	0.57	0.30 [-0.06]	0.37
2009-2003	0.43 [0.43]	0.23	0.84 [0.60]	0.83	0.18 [-0.12]	0.18

*Accuracy estimated as the absolute mean value of distance. The mean value can be used to assess possible systematic errors.
**Precision assessed as the standard deviation of distance.

Table 4.13 reports the values of $RMSE_{xy}$ before and after the application of the planar co-registration tool described in Section 3.3.3. The values of $RMSE_{xy}$ were calculated both on DEM obtained without point cloud co-registration step ("Raw DEMs") and DEMs derived from co-registered point clouds. Table 4.13 shows that the best values of $RMSE_{xy}$ were obtained using a second registration step on DEMs derived from the co-registered point clouds.

Table 4.13: RMSE between targets DEM with reference ones. The RMSE (computed along the x and y directions) were estimated before and after the application of the planar co-registration tool described in Section 3.3.3.

	Raw DEMs		**DEMs from co-registered point clouds**	
RMSE	**Before co-registration tool**	**After co-registration tool**	**Before co-registration tool**	**After co-registration tool**
DEM 2003	2.392 m	1.939 m	1.055 m	0.668 m
DEM 2009	2.469 m	1.818 m	0.969m	0.587 m

All these results of post-processing of LiDAR surveys demonstrated how the co-registration phase was fundamental for the data both at point clouds level and at the DEMs step. Williams et al., 2018 confirmed this observation and highlighted that the accuracy of alignment was one of

key sources of error when detecting change between two point clouds. The studies of Streutker et al. (2011), DeLong et al. (2012) and Lallias-Tacon et al. (2014) also established the importance of point cloud alignment in multi-temporal comparisons using airborne LiDAR data. Similar outcomes can be found in Turner et al. (2015): to prepare data for change detection, it is necessary to check the co-registration of each data pair because there is the potential for some minor misalignments, the most important of which are any differences in the Z-axis (or height). Indeed, the uncertainties could be due to the sensor's precision and accuracy, the georeferencing and the geometry of acquisition (e.g., the range to the ground and the incidence angle), and the position of the sensor (Passalacqua et al., 2015). The use of different instruments during the multi-temporal surveys, the changing of survey technologies, the systematic error in each survey, and the heterogeneity in terms of data quality may be the main factors explaining the offset between point clouds. This happens especially in LiDAR surveys where the technologic developments have been huge in the last decade, and therefore the multi-temporal comparison can show the abovementioned problems. Moreover, the comparability between data sets is a further hard task in morphologically complex terrains as in mountain regions (Victoriano et al., 2018). In these rugged environments were difficult to identify common points (fundamental in the first align step as described in Section 3.3.2) in natural scenes of multi-temporal clouds. This is most likely due to the fact that: (*i*) the point density can be different, (*ii*) the changes can be significant within the catchment in the time, and (*iii*) the surfaces are rough which reduces the accuracy of cloud matching techniques (e.g., Schürch et al., 2011; Lague et al., 2013). A lack of common targets can significantly diminish the quality of the data acquired (Passalacqua et al., 2015). Furthermore, the ICP method significantly improved the results of the multi-temporal clouds registration if it was used with a pre-processing step that moves close the different surveys through the definition of homologous points in the clouds. The ICP method is often applied for the alignment of adjacent scans of terrestrial and airborne LiDAR (Theule et al., 2012; Lallias-Tacon et al., 2014). In addition, the analysis of DEMs obtained from multi-temporal co-registered point clouds proved that, in particular in complex topographic environments and conditions, a second step of co-registration on DEMs level can enhance the results. In the Moscardo catchment, this helped increasing the accuracy of the alignment because: (*i*) 4D-data were not homogeneous in terms of quality; (*ii*) morphologically complex terrains, as in steep slope mountain regions, did not allow a perfect point clouds registration process; (*iii*) there were few areas stable in the time, or they were unequally distributed in space, and their identification was difficult due to abovementioned problems; (iv) the interpolation algorithm used to model survey data can also introduce artefacts to the DEM especially in complex local surface (Heritage et al., 2009). However, the developed DEM planar co-registration tool, described in Section 3.4, allowed the removal of any remaining constant translational bias between the datasets. In steep terrains, a small planimetric offset can

produce a high elevation error and this has a considerable effect on the volumetric computation of erosion and deposition. Therefore, it was important to have accurate co-registered DEMs to assess the real morphological changes in the time. This aspect is also underlined in Lallias-Tacon et al. (2014) where the co-registration step was fundamental to improve high-resolution multi-temporal DoDs and sediment bugged computations that were fundamental tools to study the sediment dynamics in the temporal and spatial scales considered (e.g., Brasington et al., 2012; Clapuyt et al., 2016; Cavalli et al., 2017; Vericat et al., 2017).

4.4.2 DoDs at catchment scale

After the co-registration, the DEMs (2003, 2009, 2013) of the Moscardo catchment were used to generate thresholded DoDs through FIS methodology described in Section 3.3.4. Figure 4.27 shows the thresholded DoDs (after applying the *minLoD*) where the erosion and deposition patterns of sediment dynamic were clearly visible (Section H in Fig. 3.2). Not surprisingly, the most important morphological changes were found along the main channel of the Moscardo Torrent and in the head of the catchment, characterized by widespread sediment sources. The total volume of erosion and deposition, together with the net volume change, are reported in Table 4.14. DoDs data highlight that erosion was moderate throughout 2003-2009 and showed an increase in the period 2009-2013. Instead, the deposition process shows an opposite trend: decreasing in 2013-2009 compared to 2009-2003. This finding was in line with what observed and monitored in the field during those periods. Instead, the net volume changes of 2003-2009 showed not realistic phenomena of deposition that prevailed on the erosion ones during 2003-2009. This result is strongly related to the co-registration problems described in Section 4.4.1 that affected the point clouds and DEM not chosen as references surveys (i.e., 2003 and 2009). Therefore, the DoDs volume estimation is conditioned by the level of accuracy of the multi-temporal LiDAR surveys in a complex topographic environment. The differences between thresholded (e.g., Fig. 4.26b, d, f) and raw DoD (e.g., Fig. 4.26a, c, e) underlined that the using of FIS methodology allows removing a lot of uncertainties from raw DoDs and was useful to recover some information on low magnitude erosion and deposition. However, Figure 4.27 shows still widespread noise areas where no real morphological changes were visible. This could be due to non-optimal filtering of clouds (e.g., the presence of vegetation and noise). The need of taking into account DEMs uncertainty and its propagation into DoDs was confirmed by the magnitude of uncertainties values resulting from thresholded DoDs, especially for DoD 2013-2003 (Tab. 4.14). In complex morphology, as the Moscardo catchment, several studies highlighted how greater uncertainty is found in areas of high topographic variability (high grain and/or form roughness), low point density and the slope steepness (e.g., Bowen and Waltermire, 2002; Hodgson and Bresnahan, 2004; Scheidl et al., 2008; Bater and Coops, 2009; Wheaton et al., 2010;

Milan et al., 2011; Schürch et al., 2011; Blasone et al., 2014; Cavalli et al., 2017; Keilig et al., 2019). Moreover, Heritage et al. (2009) and Milan et al. (2011) stated that the interpolation error calculated as the elevation difference between LiDAR points and DEM elevations increases with the local topographic variability. All these aspects and the obtained results highlighted the importance of the developed error analysis to assess the real morphological changes.

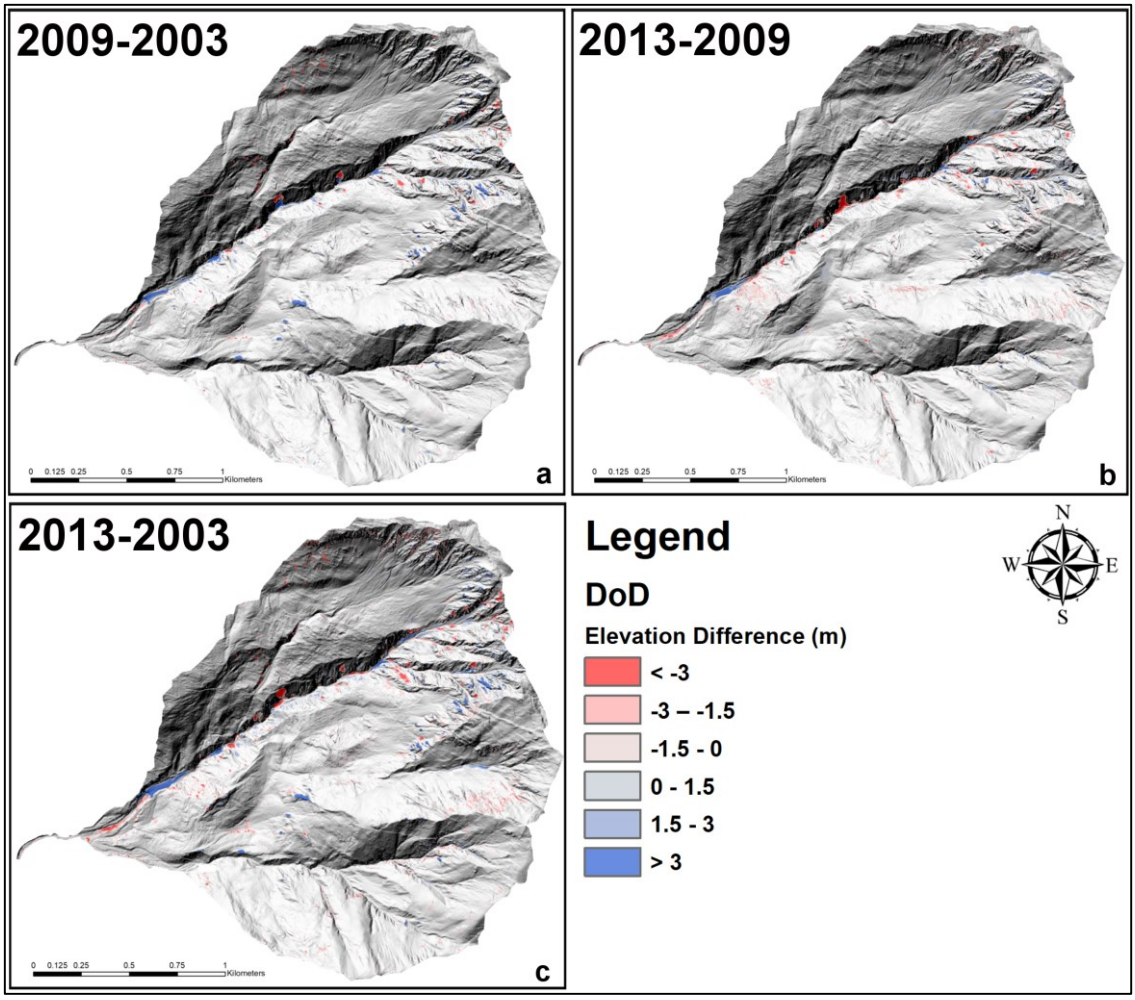

Figure 4.27: Thresholded DoDs of Moscardo catchment. a) DoD of 2003-2009. b) DoD of 2013-2009. c) DoD of 20013-2003.

Table 4.14: Total volume of erosion, deposition and net volume changes from the different DoDs of Moscardo catchment up to the monitoring station (4.11 km^2). The ± volumes were estimated based on the errors associated at the minLoD described in Section 3.3.4.

Compared data	Thresholded DoD estimate (95% CI)		
	Erosion (m^3)*	Deposition (m^3)*	Net Volume difference (m^3)*
2013-2009	240976 ± 69679	138096 ± 39859	-102879 ± 80274
2009-2003	128618 ± 40549	149046 ± 39090	+20427 ± 56323
2013-2003	306411 ± 90533	229821 ± 60023	-76590 ± 108623

In the DoD-based sediment budget, the structural (concrete and stones) volume of the five check dams built between 2005-2006 should be considered as "human-induced". However, the total volume of these check dams amounts to approximately 5400 m^3, and is thus negligible when compared to the volume changes resulting from the DoDs (Tab. 4.14).

The accuracy of the net balance resulting from DoDs volumetric estimate (Tab. 4.14) was confirmed through the data recorded at the monitoring station for the same period (Tab. 4.2) since they are in the same order of magnitude, taking into account the uncertainty bounds, the errors due to the co-registration problems and some approximations. Indeed, the debris-flow volumes recorded at the monitoring station site can be considered representative of sediment output from the drainage basin caused by debris flows. However, it must be noted that the estimations of discharged volume considered the total flowing material (which includes solids and water), while DoDs analyses are based on volume differences estimated from the terrain models (pore fluids escape rapidly from the debris-flow mixture during deposition; Blasone et al., 2014). Moreover, DoDs volumes did not consider only the volumes of debris-flow events but also the others phenomena of sediment transport (e.g., bedload transport and suspended load) occurring in the analysed period in the Moscardo basin.

Nevertheless, the LiDAR data proved to be effective to study debris-flow dynamics at wide spatial scale (catchment), even if this technology is still relatively expensive, which prevents frequent surveys. In addition, LiDAR may encounter intrinsic limitations (in terms of required accuracy and point density in complex terrains) at the reach scale where the use of SfM can be recommended for a continuous and detailed focus on fine-scale morphologies (e.g., Trevisani and Cavalli, 2016).

4.4.3 DoDs and check dams

The DoDs results along with the database of the torrent control works provide important information on sediment dynamics along the Moscardo torrent. The areas investigated through DoD approach (i.e., the channel reaches equipped with check dams; Fig. 4.28) experienced important morphological changes. A detailed analysis of erosion and deposition patterns in specific areas showed how the torrent control works deeply modified the sediment dynamics.

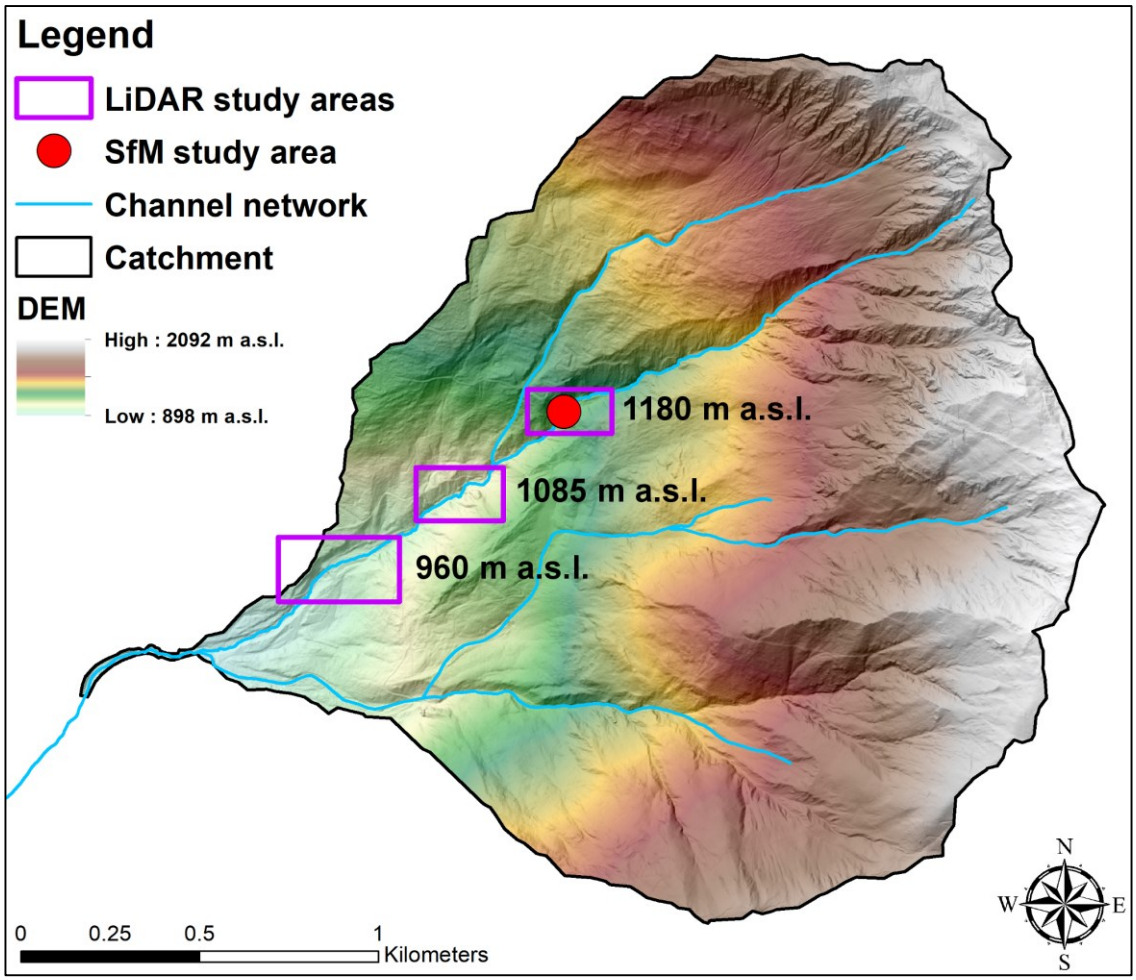

Figure 4.28: Location of specific areas where were carried out a detail analysis of erosion and deposition patterns, using DEMs obtained through LiDAR surveys. These three zone were located at 960 m, 1085 m and 1180 m a.s.l. In the areas at 960 m and 1085 m a.s.l., new check dams (n. 15, 16, 21, 22, 25; Fig. 4.5) were built between 2005-2006, while in the zone at 1180 m a.s.l. a recent structure (n. 29; Fig. 4.6b) was constructed in 2015 and another one was rebuilt (n. 30; Fig. 4.6a). In the area at 1180 m a.s.l. was also analysed through SfM surveys at check dam scale in 2015-2018 period.

Figure 4.29 shows the DoDs results in the area at 960 m a.s.l. where two check dams (n. 15 and 16; Fig. 4.5a and c) were built between 2005-2006. In the DoD 2009-2003 (Fig. 4.29a) the deposition process upstream of the two check dams and the erosion phenomena downstream the structures can be clearly observed. This trend continued in the DoD of 2013-2009 (Fig. 4.29b) and was summarised in the DoD 2013-2003 (Fig. 4.29c). The budget segregation function of GCD ArcGIS plugin (Section H in Fig. 3.2) was used to segment the DoDs by specific areas of interest and Table 4.15 show in detail the erosion and deposition with the net volume change upstream, between and downstream the check dams for all the DoDs. Specifically, Figure 4.29 shows a progressive increase of erosion (from 4400 m^3 to 10550 m^3) downstream the lowermost check dam (n. 15; Fig. 4.5a) that might undermine its stability triggering the failure of the structure. Indeed, during the years of observations (2003-2013), a total volume of 25770 m^3 of

debris was deposited upstream of this check dams, while 15070 m^3 were eroded downstream (Tab. 4.15). The depth of erosion downstream of check dam n. 15 (Fig. 4.5a) suggests that the reduction of a reach slope was not sufficient to allow the control of channel incision. This had important consequences for the stability of the structures, as in the case of the check dams n. 17 and 18 (both built in 1980; Fig. 4.4) that were destroyed and flowed downstream by debris-flow events after 2013. The DoD of 2013-2009 evidence erosion process (around 1120 m^3) in proximity of these structures (Fig. 4.29c). Furthermore, the check dam n.16 (Fig. 4.5c) was over filled in a few years (Fig. 4.3f) after its construction and the structure has been no longer visible in 2018 (Fig. 5f). Deposition acted both downstream (25770 m^3) and upstream (6080 m^3) this check dam during 2003-2013 (Fig. 4.29c).

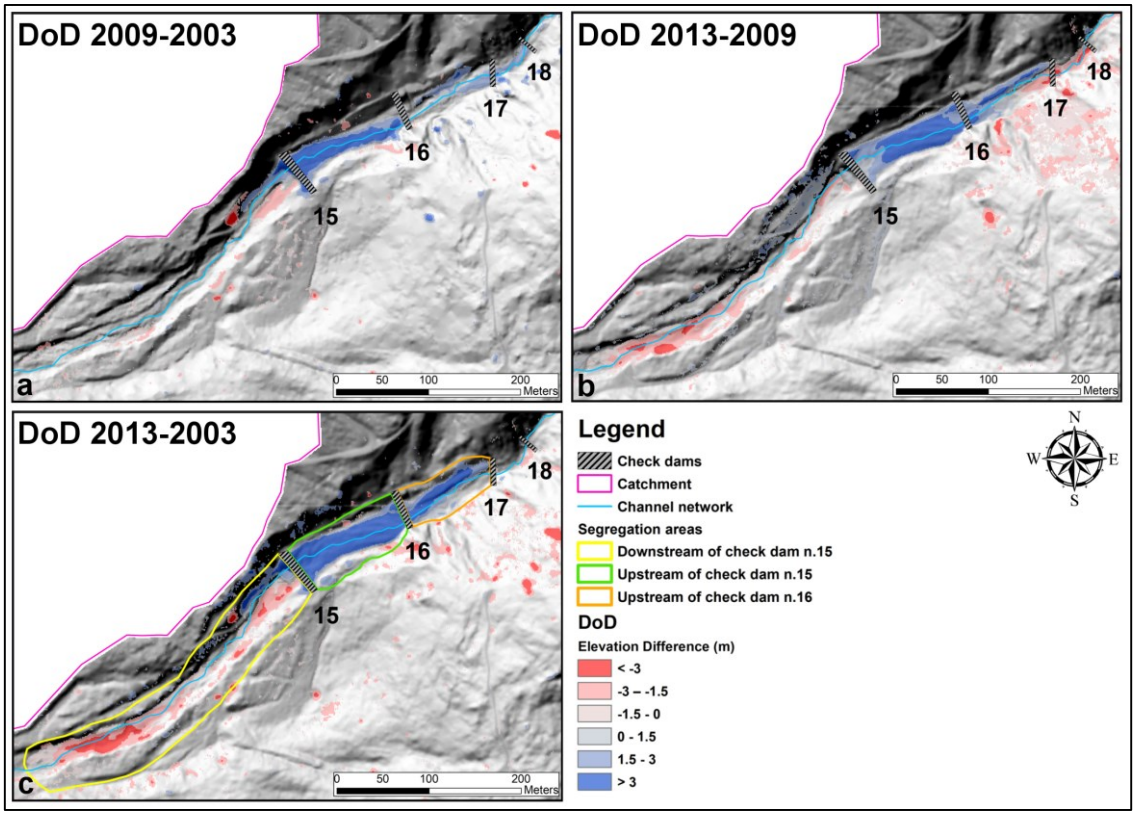

Figure 4.29: Detail of DoDs in the area where two check dams (n. 15 and 16; Fig. 4.5a and c) were built between 2005-2006. a) DoD 2009-2003; b) DoD 2013-2009; c) DoD 2013-2003 with the segregation area: upstream the check dam n. 15 and 16, and downstream the check dams n.15.

Table 4.15: Total volume of erosion, deposition, and the net volume change, for the thresholded DoDs (95 % CI) in the LiDAR survey of 2003, 2009 and 2013 for the segregation area: upstream the check dam n. 15 and 16, and downstream the check dams n.15 (Fig. 4.29c). It is important note that the ± uncertainty of volumes were estimated considering a spatially distributed minLoD based on the FIS to assess spatially variable errors as presented in Section 3.3.4.

Budget segregation of Thresholded DoD estimate (95% CI)									
Segregation areas	**Downstream check dam n. 15**			**Upstream check dam n. 15**			**Upstream check dam n. 16**		
DoD	**2009-2003**	**2013-2009**	**2013-2003**	**2009-2003**	**2013-2009**	**2013-2003**	**2009-2003**	**2013-2009**	**2013-2003**
Erosion (m^3)	4400 ± 1420	10550 ± 1950	15070 ± 3370	470 ± 170	140 ± 50	510 ± 160	80 ± 30	1120 ± 180	60 ± 20
Deposition (m^3)	2410 ± 90	2500 ± 920	3390 ± 790	11650 ± 1580	14180 ± 1110	25770 ± 2260	2610 ± 740	4060 ± 590	6080 ± 1080
Net Volume difference (m^3)	-1990 ± 1540	-8050 ± 2160	-11680 ± 3470	11170 ± 1580	14050 ± 1110	25260 ± 2260	2530 ± 740	2930 ± 610	6020 ± 1080

Figure 4.30 displays another example of how the check dams (Fig. 4.5b, d and e; n. 21, 22 and 25) caused important morphological changes along the main channel. These structures were built in 2005 and 2006 in the middle of the Moscardo catchment 1085 m a.s.l. The deposition process (around 5990 m^3) upstream the check dams n. 21 and 22 (Fig. 4. 5d and 4.5e) between 2003-2009, shown in Figure 4. 30a, was promoted by the inherent function of the check dams just after their construction: sediment trapping and decreasing of slope. Then, during the 2009-2013 time span, the sediment deposit was partially removed by streamflow and debris flow, as can be seen in Figure 4. 30b, highlighting the presence of scour-and-fill cycles as described by Berger et al. (2011) and Theule et al. (2015). Differently, the check dam (n. 25; Fig. 4.5b) presented important erosion areas both downstream (1400 m^3) and upstream (700 m^3) in the 2003-2009 DoD (Fig. 4. 30a). During 2009-2013 time, the sediment flowed around the check dam (n. 25; Fig. 4.5b) on the left wing and the erosion increased (Fig. 4. 30b): the erosion downstream the check dam was around 3450 m^3 while the material eroded upstream the structure was 890 m^3 (Tab. 4.16). The erosion phenomena might undermine the stability of the structure foundation while the stream triggered the left slope foot erosion and activated a shallow landslide (visible in Fig. 4.5b). This sediment source area can further increase the sediment supply to the main channel and thus rise debris flow volumes.

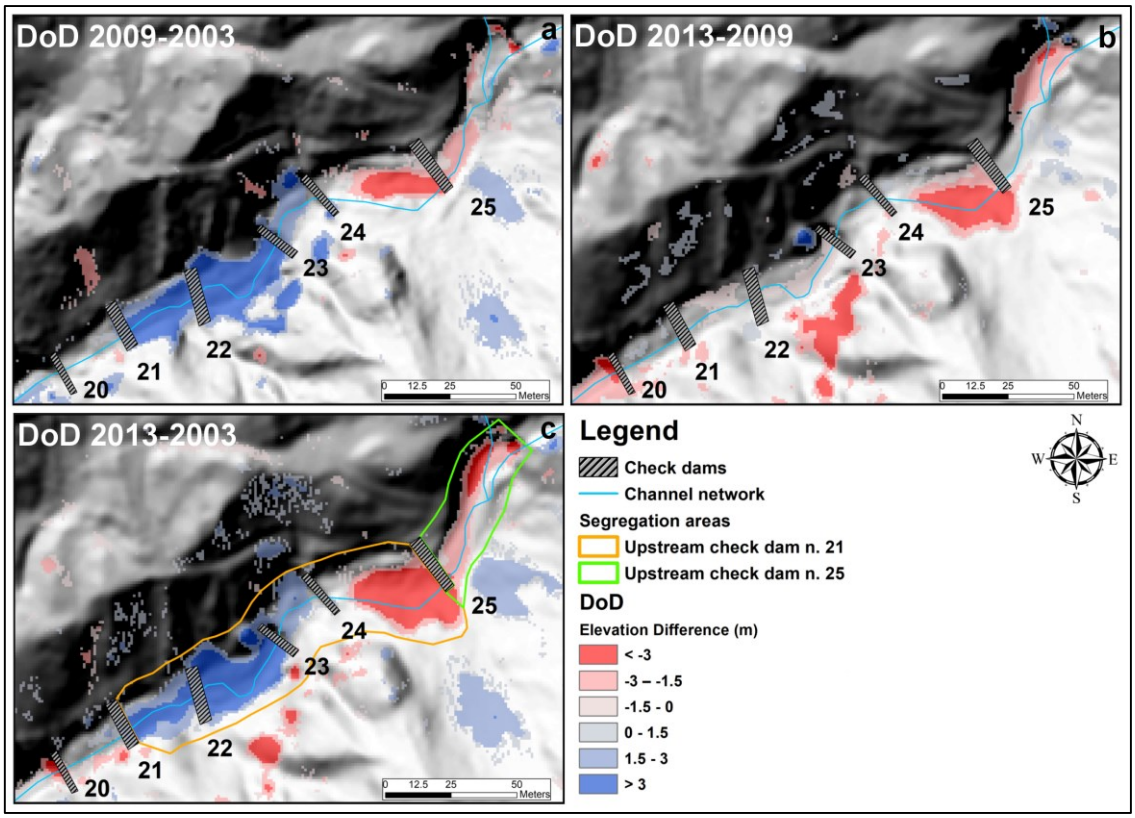

Figure 4.30: Detail of DoDs in the area where three check dams (n. 21, 22 and 25; Fig. 4.5b, d and e) were built between 2005-2006. a) DoD 2009-2003; b) DoD 2013-2009; c) DoD 2013-2003 with the segregation area: upstream the check dam n. 21 and 25.

Table 4.16: Total volume of erosion, deposition, and the net volume change, for the thresholded DoDs (95 % CI) in the LiDAR-survey of 2003, 2009 and 2013 for the segregation area: upstream the check dam n. 21 and 25 (Fig. 4. 30c). It is important note that the ± uncertainty of volumes were estimated considering a spatially distributed minLoD based on the FIS to assess spatially variable errors as presented in Section 3.3.4.

Budget segregation of Thresholded DoD estimate (95% CI)						
Segregation areas	**Upstream check dam n. 21**			**Upstream check dam n. 25**		
DoD	**2009-2003**	**2013-2009**	**2013-2003**	**2009-2003**	**2013-2009**	**2013-2003**
Erosion (m^3)	1400 ± 280	3450 ± 570	4210 ± 510	700 ± 210	890 ± 160	1460 ± 310
Deposition (m^3)	5990 ± 1130	260 ± 90	5280 ± 960	70 ± 30	80 ± 30	20 ± 10
Net Volume difference (m^3)	4590 ± 1170	-3190 ± 580	1090 ± 1080	-630 ± 210	-800 ± 170	-1440 ± 310

In these specific areas (Fig. 4.29 and 4. 30) the DoDs suggest that the check dams effectively stored the sediment transported by the debris flows immediately after their constructions (Fig. 4.29a and 4.30a), except the structure n. 25. Several works (e.g., Lenzi and Comiti 2003; Boix-Fayos et al., 2008; García-Ruiz et al., 2013; Piton and Recking, 2014) observed the same deposition patterns upstream check dams just after their construction and erosion phenomena downstream the structures. The deposition was due to the check dams inherent function of

sediment trapping and decreasing of the slope while erosion was promoted by the power of the turbulent flow dissipating the energy in the tumbling-flow (Piton and Recking, 2017) that was displaced downstream resulting from the construction of the new hydraulic control works. Therefore, the check dam with n. 25 (Fig. 4.5b) showed right away its ineffectiveness.

A further example of the effect of torrent control works on sediment dynamic is presented in Figure 4.31. This area was located in the upper part of the Moscardo catchment (1180 m a.s.l.) and three check dams (n. 28, 30, 31; Fig. 4.3d, 4.6a and 4.6b) were built in the 1980s. In this area, there were no torrent control works built in the period 2003-2013, but in 2015 the check dam (n. 30; Fig. 4.6a) was rebuilt while another structure (n. 29; Fig. 4.6b) was built ex novo. The effects of these last interventions have been analysed in detail in Section 4.3.5, while here, through the DoDs in Figure 4.31 it was possible to analyse the past debris-flow dynamics. The lowermost check dam (n. 28; Fig. 4.3d) was destroyed by a debris flow event between 2003-2009 and the Figure 4.31a evidences this occurrence. Indeed, there was erosion process upstream this check dam (n. 28; Fig. 4.3d) and deposition downstream in DoD of 2003-2009 (Fig. 4.31a), whereas an operative check dam should present opposite erosion and deposition patterns. The uppermost check dam (n. 31; Fig. 4.3c) was filled by a debris flow events between 2003-2009 (Fig. 4.31a) instead, during the period 2009-2013 the sediment flowed downstream the structure because there was erosive process (caused the damage of the check dam spillway) in the same area (Fig. 4.31b). These processes highlighted the interaction between torrent control works and the scour-and-fill cycles along the main channel. The check dam (n. 30; Fig. 4.3e) located between the two structures (n. 28 and 31; Fig. 4.3d and Fig. 4.3c), was rebuilt in 2015 at the site of a former dam that had been seriously damaged by past debris flows. Indeed, the DoD 2009-2003 (Fig. 4.31a) shows how the sediment stream flowed around the check dam on the right wing and undermined the functionality of the structure. This dynamic also continued after the check dam reconstruction as demonstrated by the analysis of DoDs (2015-2018) obtained by SfM in this specific area (see Section 4.3.5). Moreover, the shift of the flow to the right increased the coupling between the stream and the right slope above the check dam in the time (Fig. 4.31c). This process triggered the slope foot erosion and activated a shallow landslide on the right slope, as can be seen in Figure 4.31b, increasing the debris volumes.

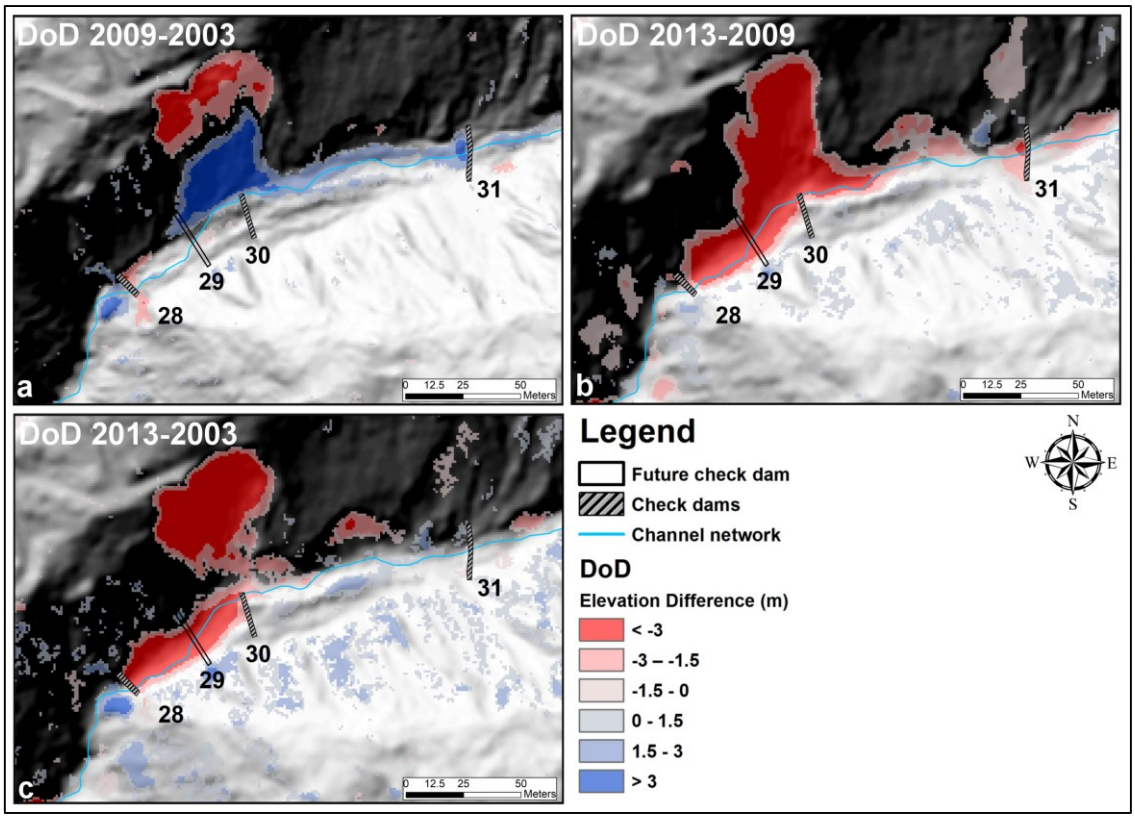

Figure 4.31: Detail of DoDs in the upper part of the Moscardo catchment where there were three check dams (n. 28, 30 and 31; Fig. 4.3d, e and c respectively). a) DoD 2009-2003; b) DoD 2013-2009. c) DoD 2013-2003.

4.4.4 Index of Connectivity (IC) and Difference of IC

The IC analysis was applied to the Moscardo catchment using the 2003, 2009 and 2013 DEMs to assess the changes in sediment transfer pathways. Figure 4.32 shows the maps of the IC calculated with regard to the catchment outlet. The IC maps illustrate quite clearly the different pattern of sediment connectivity in the various parts of the catchment. The maps show high values of IC in the upper part of the catchment and along the steep main channel (covered by alluvium and debris-flow deposits), suggesting that sediment source areas (mainly located at the head of the basin and along channel side slopes) and deeply incised channels are highly connected to the catchment outlet. Higher sediment connection between hillslopes and basin outlet was observed for the sub-catchment, featuring mainly debris flow processes. Lower values of the index were found along gentle slopes (e.g., in the middle tributary on the left-side of the Moscardo torrent) and in the correspondence of low-slope moraine material adjacent to the middle part of the main channel. An important aspect was the change of connectivity values over time along the main channel and unstable areas (Fig. 4.32a), whereas in the remaining part of the catchment, the connectivity has remained quite unchanged during 2013-2003. In particular, Figure 4.32 shows lower values of IC in 2009 than the map of 2003 between the sediment source areas, the hillslopes

and the main channel network. In 2013 map, the IC increased again approaching values similar to the 2003 IC map. Figure 4.32d confirms this connectivity variation over time in changed areas.

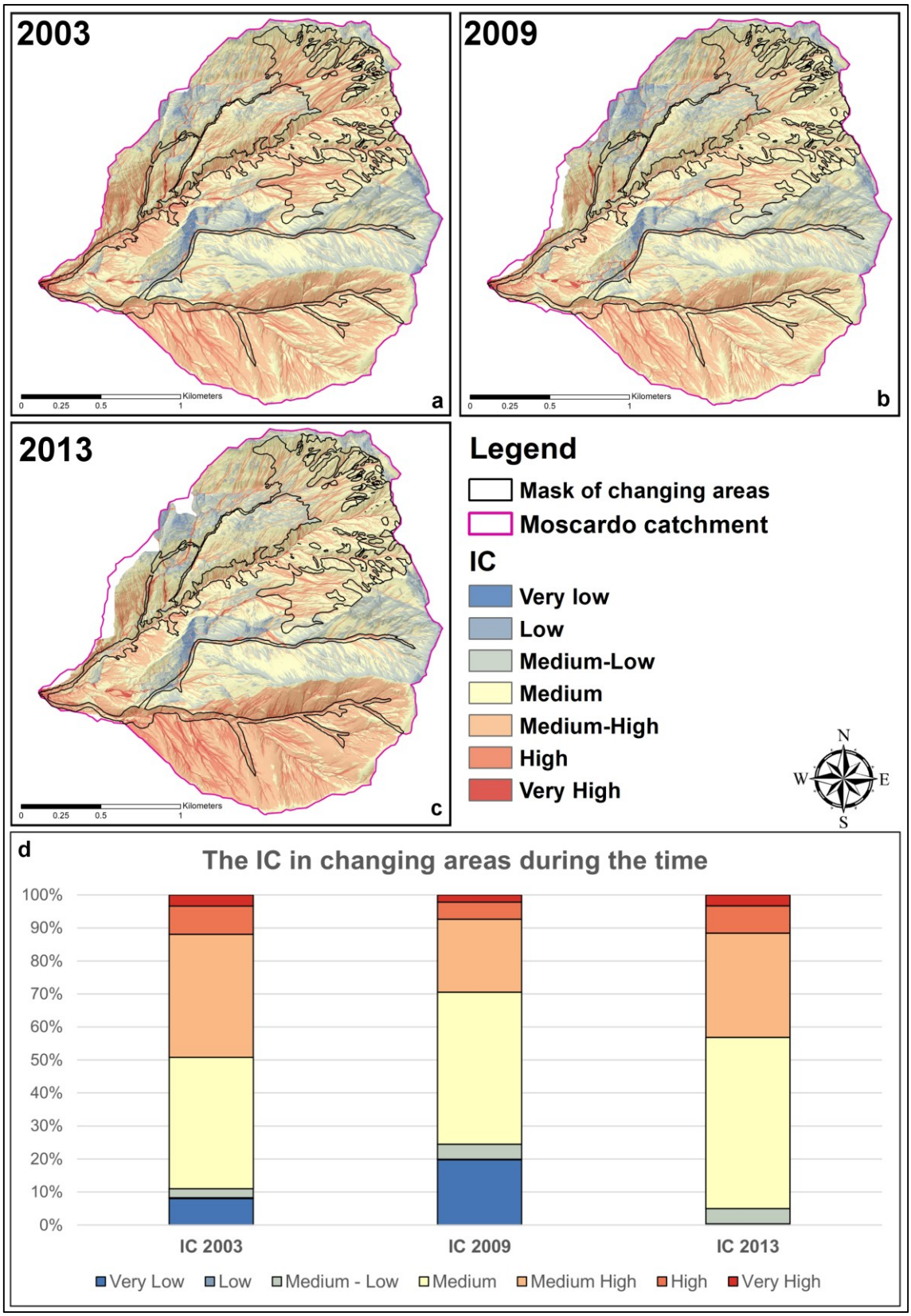

Figure 4.32: Multi-temporal IC of Moscardo catchment with regard to the catchment outlet. The maps of IC display different spatial extension because the building of a road after 2003 modified some surface flow directions and the drainage network on the right hillslope. Therefore, the upslope contributing area of the zone was different and the IC

maps of 2009 and 2013 changed. The index values have been classified into seven classes (very low, low, medium-low, medium, medium-high, high and very high) based on the Natural Breaks classification methods. a) IC of 2003. b) IC of 2009. c) IC of 2013.

The analysis of multi-temporal IC along the Moscardo main channel allowed detailed assessment of the torrent control works role on sediment dynamic over time. For example, Figure 4.33 shows ICs and DoIC maps in the area at 960 m a.s.l. These maps underline how the sediment pathways deeply changed after the building of the check dams and how the presence of the structure modified the sediment dynamic in 2003-2013 time (Fig. 4.33f). After the building of the check dams (n. 15 and 16; Fig. 4.5a and c), the values of connectivity decreased in the map of 2009 (Fig. 4.33b) compared to the IC of 2003 (Fig. 4.33a) in the area upstream the structures, due to the huge deposition process described in Figure 4.29a. This connectivity change is evident in Figure 4.33d where a large decrease of IC upstream the check dams but also a slight connectivity reduction downstream the lowermost check dam (n. 15; Fig. 4.5a) can be clearly observed. Moreover, the coupling between hillslopes and the main channel decreased during 2003-2009 especially on the right slope above the check dams (Fig. 4.33d) highlighting how the local interventions influenced also the large scale connectivity. Afterward, the IC of 2013 (Fig. 4.33c) shows how the sediment started to flow around the deposit upstream the new check dams and the connectivity increased again during 2013-2009 period (Fig. 4.33e), compared to 2003-2009 (Fig. 4.33e), both downstream and upstream the torrent control works. In particular, it can be noticed a large increase of DoIC (Fig. 4.33e) located in the zone of the uppermost check dams (n. 17 and 18) that were damaged by debris flow events and flowed downstream after 2013. Based on these observations, we can argue that future events will flow downstream along preferential paths defined by the torrent control works and by the morphology of debris-flow deposits which could act as sediment sources further increasing downstream debris-flow magnitude.

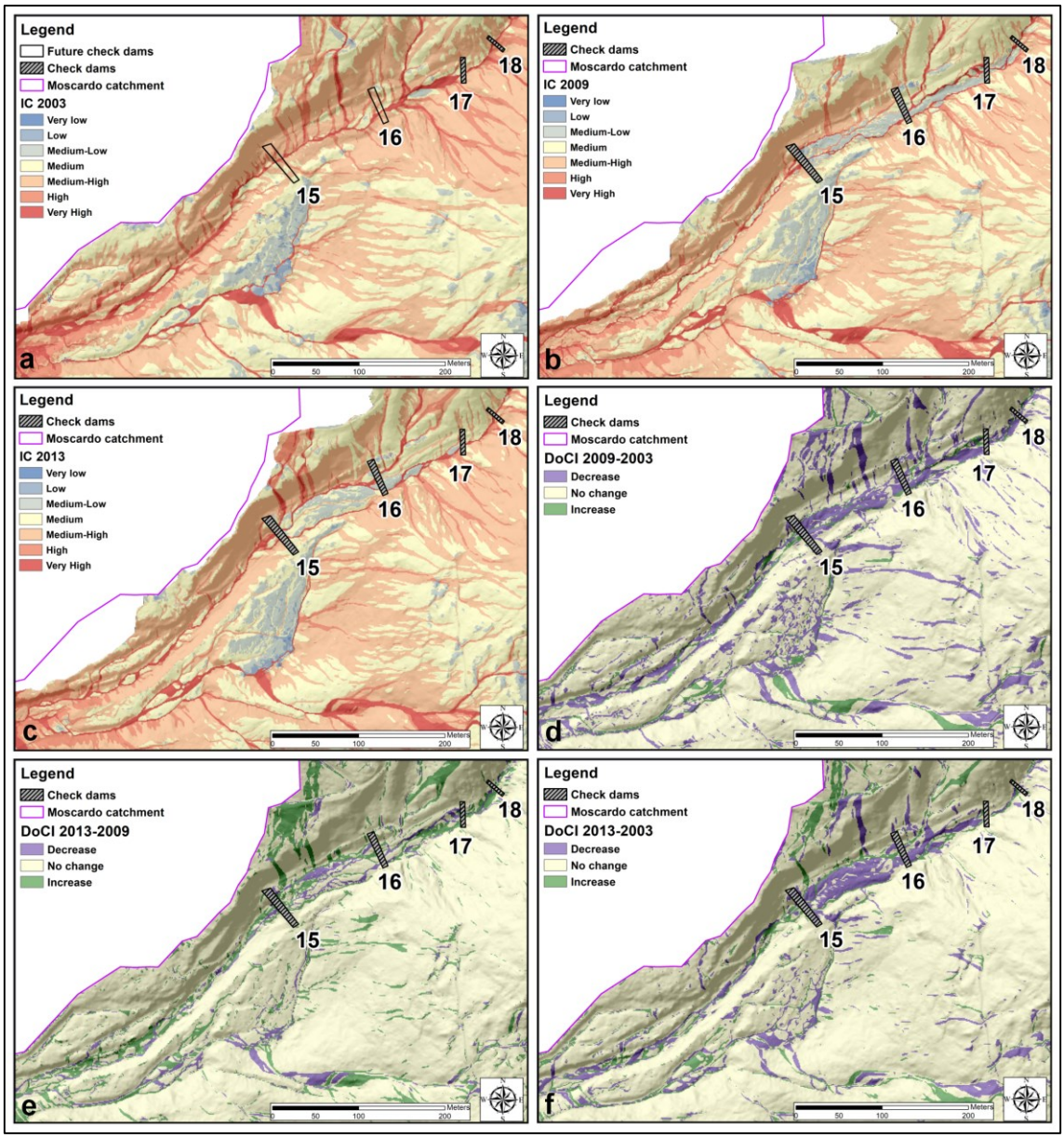

Figure 4.33: ICs and DoICs of the area where two check dam were built in 2005-2006 (Fig. 4.5a and c; n. 15 and 16). The maps of IC display different spatial extent because the building of a road after 2003 modified the flow directions and the drainage area on the right hillslope. Therefore, the upslope contributing area was different and the IC maps of 2009 and 2013 changed. a) IC 2003. b) IC 2009. c) IC 2013. d) DoIC 2009-2003. e) DoIC 2013-2009. f) DoIC 2013-2003.

A further example of multi-temporal IC and DoIC along the Moscardo was presented in Figure 4.34. These results confirmed the dynamic presented in Section 4.4.3 for this area (1180 m a.s.l.; Fig. 4.31). In particular, how the sediment stream flowed around the check dam (n. 30; Fig. 4.6b) on the right wing (Fig. 4.34f) and undermined their functionality. The IC already shows the flunking around the check dam in 2003 (Fig. 4.34a; Fig. 4.35a), then the structure was over-filled by the sediment after a debris-flow event in 2009 that modified the sediment connectivity in this area (Fig. 4.34b; Fig. 4.35b). Then, Figure 4.34c displays how the sediment flow restarted

to flow around the check dam (n. 30; Fig. 4.6b) in 2013 (Fig. 4.35c) and this dynamic also continued after the check dam reconstruction (Fig. 4.35d) as demonstrated by the analysis of DoDs (2015-2018; see Section 4.3.5).

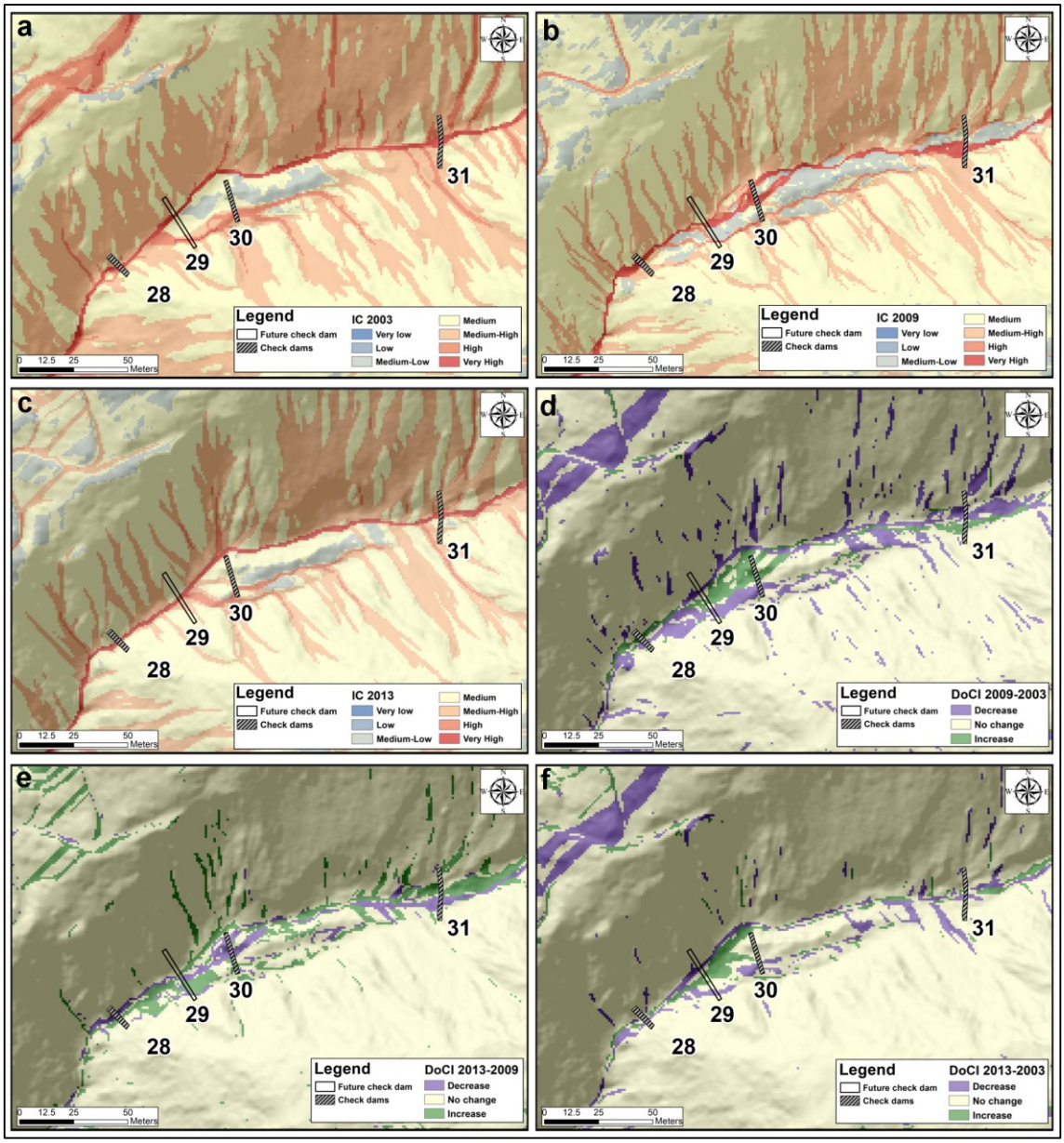

Figure 4.34: ICs and DoICs in the upper part of the Moscardo catchment where there were three check dams (n. 28, 30 and 31; Fig. 4.3d, e and c respectively). a) IC 2003. b) IC 2009. c) IC 2013. d) DoIC 2009-2003. e) DoIC 2013-2009. f) DoIC 2013-2003.

Moreover, Figure 4.34e displays how the shift of the flow on the right increased the coupling between the stream and the right slope above the check dam in the time. Instead, regarding the lowermost check dam (n. 28; Fig. 4.3d), the Figure 4.34b and d shows how the IC increased near the structure after the cheek dam destruction. This can cause a growth of debris-flow volumes, resulting in increased hazard downstream.

Figure 4.35: The check dam (n. 30) over time. a) The damaged right wing of the check dam in 2002 (Dini, 2011). b) The filled check dam in 2009 (Dini, 2011). c) The flunking around the check dam in 2013. Blasone 2013. d) The check dam in October 2018. The water flows on the right wing. Marchi 2018.

4.4.5 DoD and Difference of IC

The analysis of sediment pathways was compared with DoD-derived erosion and deposition patterns (along the main channel). Figure 4.36 shows two examples of overlapping between DoDs (Fig. 4.29c and 4.31c) and DoIC (Fig. 4.33f and 4.34f) maps of 2003-2013 time along the main channel in two areas (960 m and 1180 m a.s.l.) previously described. The comparison of DoD and DoIC data highlight the strong correspondence between deposition patterns and the areas characterized by decreasing values of connectivity while the erosion areas showed increasing measures of connectivity (Fig. 4.36). This trend is confirmed by the cross frequency analysis of DoD and DoIC values (Tab. 4.17) calculated for the main channel zone, shown in Figure 4.36. Higher frequency values occurred at erosion/IC increase and deposition/IC decrease (Tab. 4.17). These examples underlined how the changes in structural connectivity were linked to the morphodynamics changes. The multi-temporal IC and DoIC maps (Fig. 4.33 and 4.34), and DoDs information (Fig. 4.29 and 4.31) prove to be complementary and fundamental tools to assess the effects of torrent control works on sediment dynamic. Indeed, the quantitative analysis of sediment transfer (i.e., DoDs) added to the maps of potential sediment pathways (i.e., IC and

DoIC) contribute to understanding debris-flow dynamic both in terms of the structural (Bracken et al., 2013; Heckmann and Vericat, 2018) and functional (Bracken et al., 2015) connectivity. These study underlined the existence of a relationship between IC and functional connectivity, and hence the predictive (or explanatory) capacity of IC (Heckmann and Vericat, 2018). An evident example of this aspect is shown in Figure 4.36b, where the DoIC displays how the sediment path flowed around the check dam (n. 30; Fig. 4.3e) on the right wing, triggering the shallow landslide identified by DoD analysis (Fig. 4.31). Moreover, this comparison of data could enable the identification of the new potential sediment source areas. Indeed, the building of check dams adversely modified the sediment dynamic creating deposition areas where the level of IC was high, therefore the material can be easily mobilized.

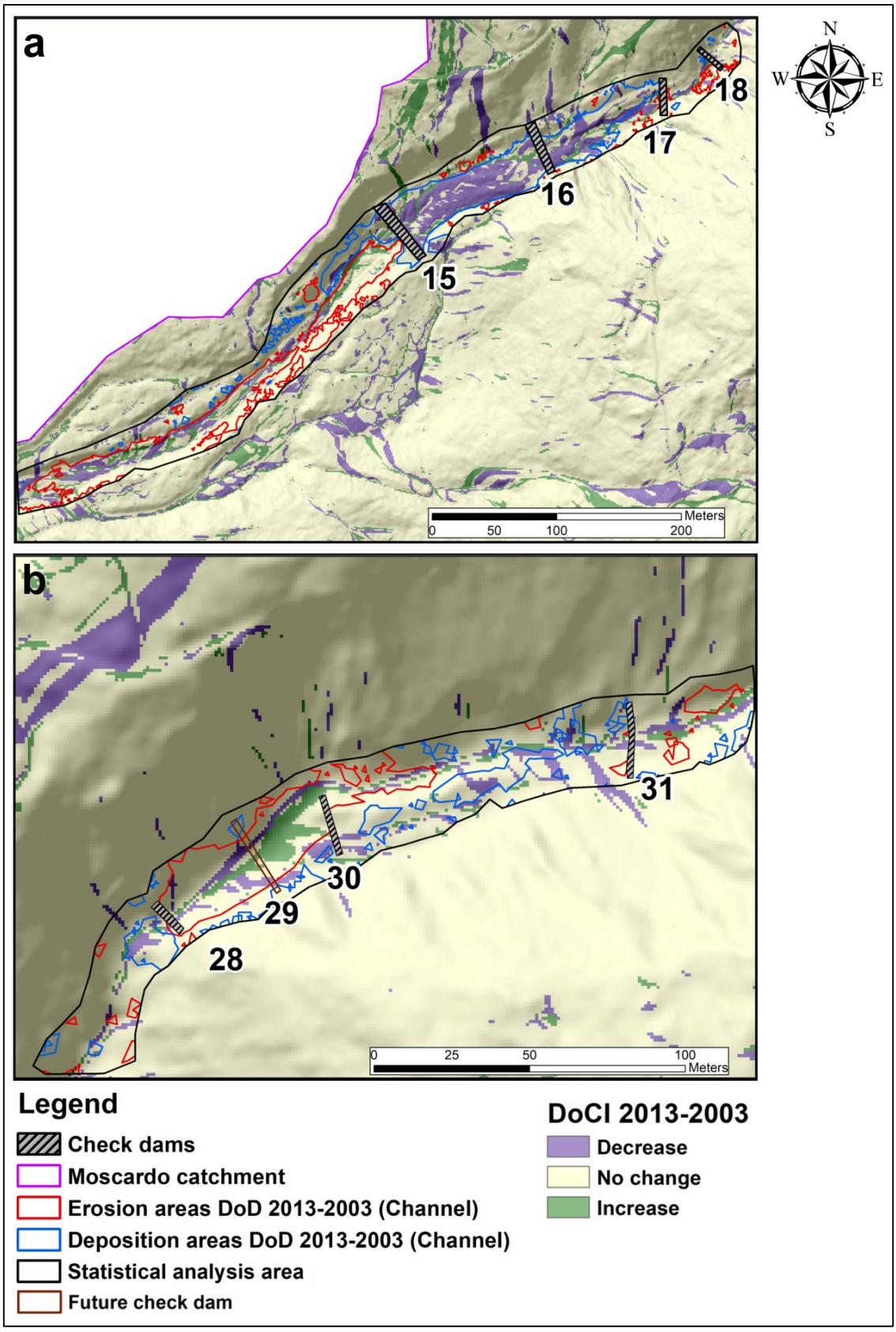

Figure 4.36: Examples of overlapping of DoD and DoIC map of 2003-2013 time window. The DoD data was focalized only on Moscardo main channel. a) Focus on the area where two check dams were built during 2005-2006 period (Fig.

4.5a and c; n. 15 and 16). b) Focus in the upper part of the Moscardo catchment where there were three check dams (n. 28, 30 and 31; Fig. 4.3d, e and c respectively).

Table 4.17: The DoD-DoIC 2013-2003 cross frequency for the analysis area outlined in Figure 4.36. The DoD and DoIC data were divided into positive values (deposition process) and negative values (erosion process) for DoD 2013-2003 and positive values (connectivity index increase) and negative values (connectivity index decrease) for DoIC2013-2003. (a) Statistical analysis for DoD vs DoIC 2013-2003 in the area at 960 m a.s.l. (Fig. 4.36a). b) Statistical analysis for DoD vs DoIC 2013-2003 in the area at 1180 m a.s.l. (Fig. 4.36b).

Area at 960 m a.s.l.	Erosion	Deposition
IC decrease	694	4181
IC increase	725	782
Area at 1180 m a.s.l.		
IC decrease	176	199
IC increase	299	26

4.4.6 The sediment dynamics and check dams at catchment scale

The results showed an increase of erosion patterns due to debris flow activity from 2003-2009 to 2009-2013 time periods both at catchment scale (Fig. 4.27 and 4.32) and along the Moscardo main channel (Fig. 4.29, 4.30, 4.31, 4.33 and 4.34). This finding was in line with field observations and monitoring data during those periods: larger debris flows were recorded throughout 2009-2013 than in the 2003-2009 period (Tab. 4.2). The decreasing of erosion during 2003-2009 period could be ascribed to the building of the new torrent control works (n. 15, 16, 21, 22; Fig. 4.5a, c, d, e) along the main channel in 2005-2006. Indeed, the DoDs analysed areas (Fig. 4.29 and 4.30) suggested that the check dams effectively stored sediment transported by the debris flows immediately after their constructions (Fig. 4.29a and 4.30a), except the structure n. 25 (Fig. 4.5b). The work of Arattano et al. (2012) confirms these observations. They stated that the substantial downstream attenuation of the magnitude, for the event of 24 August 2006 can be ascribed to the effects of the torrent control works that have been implemented in the Moscardo basin since late 1990s. The studied event indicates that the hydraulic works in the Moscardo Torrent were effective in reducing the intensity of debris flows of small and moderate magnitude. This attenuating effect proved to be much less relevant for a large debris flow, which occurred in September 2011.

The new check dams considerably modified the sediment dynamics along the main channel (longitudinal connectivity) but also the hillslope-to-channel connectivity (lateral connectivity), as shown Figure 4.36b. Similar result was underlined by Fryirs (2013) that stated how the structures disrupt longitudinal linkages in the sediment connectivity through their effect on the base level or bed profile of a channel. Other researches (Meade, 1982; Poeppl et al., 2017; Heckmann et al., 2017; Wohl, 2017) reported comparable outcomes, emphasizing how human modifications (like

torrent control works) to rivers induced considerable consequences to the catchment connectivity: the changes in structural (Bracken et al., 2013) connectivity affects functional (Bracken et al., 2015) connectivity by altering sediment pathways and rates of transfer (Heckmann et al., 2018). These effects of channel control works are particularly relevant in a catchment, such as the Moscardo, where the sediment sources and the channel network are closely highly coupled (Fig. 4.32). Table 4.3 (see Section 4.1) seems to confirm that there were no major changes in the rainfall pattern during 2003-2013. Moreover, considering that moderate rainfall events also could trigger debris-flow phenomena in the Moscardo catchment (Deganutti et al., 2000; Marchi et al., 2002; Blasone, 2014), the availability of sediment along the channel network, was the major factor for the triggering and the magnitude of the Moscardo debris flows. Other studies recognized the presence of erodible sediment in channels as a primary control on the occurrence (Deganutti et al., 2000) and magnitude of debris flows (Jakob, 2005; Theule et al., 2012). Various researches reported that the volume of channelized debris-flows is strongly influenced by channel scouring along the flow path (Bovis and Jakob, 1999; Hungr et al., 2005; Remaître et al., 2005; Veyrat-Charvillon and Memier, 2006; Theule et al., 2012; Comiti et al., 2014). This is also the case of the Moscardo Torrent, where the availability of sediment along the channel network is a major factor for the occurrence and the magnitude of the Moscardo debris flows. Not surprisingly, the new check dams were quite effective in reducing channel scour and favouring sediment deposition, thus decreasing debris-flow magnitude in the years immediately after their construction. However, as Bracken et al. (2015) highlighted, the storage of sediment at short timescales (caused by high frequency and low-magnitude events and often over relatively short transport distances) facilitates sediment connectivity at much broader spatial and temporal scales. In our study area, the sediment stored upstream of the new check dams (with n. 15, 16, 21, 22; Fig. 4.5a, c, d, e) in the 2000s was partly mobilized along by the high-magnitude debris flows that occurred in 2012. This effect is reflected by the large erosion values observed in the 2009-2013 period (Fig. 4.29b and 4.30b). Regarding these aspects, some researches, as the ones conducted by Jaeggi and Pellandini (1997) and, Piton and Recking (2017), described how check dams were built to temporarily store and then later release sediment (probably more frequently but with each volume smaller on average) that the torrent would have release abruptly in mass, thus making easier to manage regarding hazard mitigation. However, if the planning of check dams was not optimal (in terms of location and typology of structures) and the frequency and magnitude of events were high, the check dams can be ineffective or damaging in terms of costs/benefits. Moreover, the collapse of check dams (e.g., n. 17 and 18) with the consequent release of the stored material has also increased the debris-flow volume. Therefore, a careful analysis of the context and a sediment dynamic assessment at different spatial and temporal scale

is needed to evaluate the requirement and usefulness of torrent control works before planning any intervention.

5. Final Remarks and Conclusions

The multi-temporal HRT data have proven extremely useful to monitor the sediment dynamics and the morphology changes over the time in a debris-flow catchment. However, the use of HRT required the design of appropriate workflows for data post-processing and uncertainty assessment, to guarantee the coherence among data acquired in different epochs. Indeed, they often show several comparison problems in terms of point cloud density, accuracy and precision. Fundamental steps of the developed workflow were the co-registration and error analysis, which have been important especially in a topographically complex environment as the Moscardo debris-flow catchment. The methodological workflow used to process LiDAR data enabled the achievement of suitable data to monitor geomorphic change at wide spatial scale. Instead, SfM surveys allowed carrying out topographic models with a resolution and accuracy appropriate to study the effects of individual debris flows at a detailed (reach) scale over a time span sufficient to assess the performance of torrent control works. Indeed, the developed SfM workflow proves to be adequate for acquiring 4D-HRT in a rugged environment like a debris-flow channel. Nevertheless, the SfM technique is limited at broad spatial scales. For that reason, an integrated analysis of SfM data and LiDAR survey, as those presented here, allowed a whole assessment of sediment dynamic at any time and space scale. The 4D-DEMs obtained from HRT surveys enabled the analysis of the erosion and deposition patterns (through DoDs) and the maps of potential sediment pathways (through IC and DoIC). All these tools proved to be very useful and interconnected to study the debris-flow dynamic both in terms of the structural and functional connectivity.

In regards to the role of torrent control works on the sediment dynamic, this study underlines how, before taking decisions concerning the maintenance of existing check dams or the design of new ones, an in-depth analysis of sediment connectivity and spatial patterns, and the detailed knowledge of control structure effect on debris-flow dynamics, are needed. This research indicates how the solution of the check dams along the Moscardo main channel cannot be evaluate satisfactory for the following reasons: (*i*) the check dams cannot be considered a long-terms useful solution for debris-flow risk reduction in the Moscardo catchment where the hydro-erosive processes have been huge and widespread. They temporary stored volumes of debris just after their construction but when the structures were filled, (this happened in few years in the Moscardo catchment), the check dams acted as sediment sources that increased debris-flow bulking related to channel scouring during next propagations. Therefore, debris-flow events with higher magnitude flowed downstream structures already damaged by previous erosion process. (*ii*) The unsuitable location of some structures led to their failure and their collapse caused an increase of

debris-flow volume after the release of the stored material. Moreover, the sediment paths flowed around some check dams highlighting an inadequate design of the structures. This process triggered slope foot erosion and activated a shallow landslide, a further sediment source area for debris-flow processes.

The study of the torrent control works role on sediment dynamics over time allowed the understanding the past errors and the improvement of future planning on debris-flow management strategies. Indeed, these observations could help to:

- understand where the torrent control works have negative effect on debris-flow dynamics. For example, the overlapping of DoIC and DoD maps allows to analyze how much the building of check dams changes sediment paths and induces the connectivity increasing in sediment source areas, growing the potential risk of erosion process. In this way, it is possible to understand where operate to correct the realized constructions and improve the future management of the structures;
- optimize the torrent control works location that is fundamental for debris-flow control at catchment scale;
- use the sediment volumes estimation (as the ones presented here) as benchmarks for numerical modelling or simulations of debris flows, especially in channels with check dams, to improve the structural design of torrent control works;
- evaluate the susceptibility of check dams at the damage. This can be used together with natural hazard risk assessments to prioritize and rationalize future maintenance investments;
- obtain more realistic cost-benefit ratios of the adopted strategies and, in this way, select the best solutions. Indeed, the 4D sediment dynamic analysis leads to consider the possibility of adopting other more effective engineering solutions to reduce the debris-flow risk and to use efficiently the public financial resources in the Moscardo catchment; for example, flexible ring-net barriers or sediment retention basins (they must undergo periodical emptying).

References

AgiSoft LLC, 2010. Agisoft Lens User-Manual. Version 1.2.0. http://www.agisoft.com/downloads/user-manuals. [Accessed on 22 June 2017].

Arattano, M., Deganutti, A.M., Marchi, L., 1997. Debris flow monitoring activities in an instrumented watershed of the Italian Alps. In: Chen, C. (Ed.), Proceedings, First International Conference on Debris-flow Hazard Mitigation: Mechanics, Prediction, and Assessment. Water Resources Engineering Division/ ASCE, New York, pp. 506–515.

Arattano, M., Marchi, L., 2005. Measurements of debris flow velocity through cross-correlation of instrumentation data. Nat. Hazards Earth Syst. Sci. 5, 137–142.

Arattano, M., Marchi, L., 2008. Systems and sensors for debris-flow monitoring and warning. Sensors 8, 2436-2452.

Arattano, M., Mortasa, G., Deganutti, A.M., Marchi, L., 1996. Esperienze di monitoraggio delle colate detritiche nel Torrente Moscardo (Alpi Carniche). Supplemento a GEAM – Geoingegneria Ambientale e Mineraria, Anno 33, 2-3, 33-43.

Arattano, M., Marchi, L., Cavalli, M., 2012. Analysis of debris-flow recordings in an instrumented basin: Confirmations and new findings. Nat. Hazards Earth Syst. Sci. 12, 679–686.

Ashmore, P.E., Church, M., 1998. Sediment transport and river morphology: a paradigm for study. In: Klingeman, P.C., Beschta, R.L., Komar, P.D., Bradley, J.B. (Eds.), Gravelbed Rivers in the Environment. Water Res. Pubs, CO, 115-148.

Ballesteros Cánovas, J.A., Stoffel, M., Corona, C., Schraml, K., Gobiet, A., Tani, S., Sinabell, F., Fuchs, S., Kaitna, R., 2016. Debris-flow risk analysis in a managed torrent based on a stochastic life-cycle performance. Sci. Total Environ. 557–558, 142–153.

Batalla, R.J., Salka, M., 1995. Estimacions hidrologiques i de moviment de sediment a la riuada del 7 d'Agost de 1996 a la conca del Barranco de Arás (Pirineu aragones). Acta Geològica Hispànica 30, 51-59.

Bater, C.W., Coops, N.C., 2009. Evaluating error associated with LiDAR-derived DEM interpolation. Comput. Geosci. 35, 289–300.

Bemis S.P., Micklethwaite, S., Turner, D., James, M.R., Akciz, S., Thiele, S.T., Bangash, H.A., 2014. Ground-based and UAV-Based photogrammetry: A multi-scale, high-resolution mapping tool for structural geology and paleoseismology. J. Struct. Geol. 69, 163-178.

Benito, G., Grodek, T., Enzel, Y., 1998. The geomorphic and hydrologic impacts of the catastrophic failure of flood-control-dams during the 1996-Biescas flood (Central Pyrenees, Spain). Zeitschrift für Geomorphologie 42, 417-437.

Berger, C., McArdell, B., Schlunegger, F., 2011. Sediment transfer pattern at Illgraben catchment, Switzerland: Implications for the time of debris flow activities. Geomorphology 125, 421-432.

Bianco, G., Franzi L., 2000. Estimation of debris flow volumes from storm events. In Debris-flow Hazards Mitigation: Mechanics, Prediction, and Assessment, Wieczorek GF, Naeser ND (Eds). Balkema: Rotterdam; 441– 448.

Blasone G., 2014. Monitoraggio dei processi idroerosivi con impiego di rilievi ad alta risoluzione. PhD thesis in economia, ecologia e tutela dei sistemi agricoli e paesistico ambientali. Supervisor Prof. Cazorzi, F., University of Udine, XXVI Cycle, 176 p.

Blasone, G., Cavalli, M., Marchi, L., Cazorzi, F., 2014. Monitoring sediment source areas in a debris-flow catchment using terrestrial laser scanning. Catena 123, 23–36.

Boix-Fayos, C., de Vente, J., Martínez-Mena, M., Barberá, G.G., Castillo, V., 2008. The impact of land use change and check-dams on catchment sediment yield. Hydrol. Process. 22, 4922-4935.

Borga, M., Stoffel, M., Marchi, L., Marra, F., Jakob, M., 2014. Hydrogeomorphic response to extreme rainfall in headwater systems: Flash floods and debris flows. J. Hydrol. 518, 194–205.

Borselli, L., Cassi, P., Torri, D., 2008. Prolegomena to sediment and flow connectivity in the landscape: a GIS and field numerical assessment. Catena 75, 268-277.

Bovis, M.J., Jakob, M., 1999. The role of debris supply conditions in predicting debris flow activity. Earth Surf. Process. Landf. 24, 1039-1054.

Bowen, Z.H., Waltermire, R.G., 2002. Evaluation of light detection and ranging (LIDAR) for measuring river corridor topography. J. Am. Water Resour. Assoc. 38 (1), 33–41.

Brasington, J., Langham, J., Rumsby, B., 2003. Methodological sensitivity of morphometric estimates of coarse fluvial sediment transport. Geomorphology 53, 299–316.

Brasington, J., Rumsby, B.T., McVey, R.A., 2000. Monitoring and modelling morphological change in a braided gravel-bed river using high-resolution GPS-based survey. Earth. Surf. Process. Landf. 25, 973-990.

Brasington, J., Vericat, D., Rychkov, I., 2012. Modeling riverbed morphology, roughness, and surface sedimentology using high-resolution terrestrial laser scanning. Water Resour. Res. 48, 1–18.

Bracken, L.J., Turnbull, L., Wainwright, J., Bogaart, P., 2015. Sediment connectivity: A framework for understanding sediment transfer at multiple scales. Earth Surf. Process. Landforms.

Bracken, L.J., Wainwright, J., Ali, G.A., Tetzlaff, D., Smith, M.W., Reaney, S.M., Roy, A.G., 2013. Concepts of hydrological connectivity: Research approaches, Pathways and future agendas. Earth-Science Rev. 119, 17–34.

Bremer, M., Sass, O., 2012. Combining airborne and terrestrial laser scanning for quantifying erosion and deposition by a debris flow event. Geomorphology 138, 49–60.

Carbonneau, P.E., Dietrich, J.T., 2017. Cost-effective non-metric photogrammetry from consumer-grade sUAS: implications for direct georeferencing of structure from motion photogrammetry. Earth. Surf. Process. Landf. 42, 473-486.

Carley, J.K., Pasternack, G.B., Wyrick, J.R., Barker, J.R., Bratovich, P.M., Massa, D.A., Reedy, G.D., Johnson, T.R., 2012. Significant decadal channel change 58-67years post-dam accounting for uncertainty in topographic change detection between contour maps and point cloud models. Geomorphology 179, 71–88.

Carrivick, J.L., Smith, M.W., Quincey, D.J., 2016. Structure from Motion in the Geosciences. New Analytical Methods in Earth and Environmental Science. WILEY-BLACKWELL.

Cavalli, M., Goldin, B., Comiti, F., Brardinoni, F., Marchi, L., 2017. Assessment of erosion and deposition in steep mountain basins by differencing sequential digital terrain models. Geomorphology 291, 4–16.

Cavalli, M., Marchi, L., 2008. Characterisation of the surface morphology of an alpine alluvial fan using airborne LiDAR. Nat. Hazards Earth Syst. Sci. 8, 323–333.

Cavalli, M., Tarolli, P., 2011. Application of LiDAR technology for river analysis. Italian Journal of Engineering Geology and Environment. Special Issue 1, 33-44

Cavalli, M., Trevisani, S., Comiti, F., Marchi, L., 2013. Geomorphometric assessment of spatial sediment connectivity in small Alpine catchments. Geomorphology 188, 31–41.

Clapuyt, F., Vanacker, V., Van Oost, K., 2016. Reproducibility of UAV-based earth topography reconstructions based on Structure-from-Motion algorithms. Geomorphology 260, 4-15.

Clapuyt, F., Vanacker, V., Schlunegger, F., Van Oost, K., 2017. Unravelling earth flow dynamics with 3-D time series derived from UAV-SfM models. Earth Surf. Dyn. 5, 791–806.

Comiti, F., Marchi, L., Macconi, P., Arattano, M., Bertoldi, G., Borga, M., Brardinoni, F., Cavalli, M., D'Agostino, V., Penna, D., Theule, J., 2014. A new monitoring station for debris flows in the European Alps: first observations in the Gadria basin. Nat. Hazards 73, 1175-1198.

Conesa-García, C., López-Bermúdez, F., García-Lorenzo, R., 2007. Bed stability variations after check dam construction in torrential channels (South-East Spain). Earth Surf. Process. Landforms.

Cook, K.L., 2017. An evaluation of the effectiveness of low-cost UAVs and structure from motion for geomorphic change detection. Geomorphology 278, 195-208.

Coussot, P., 1992. Rheology of Debris Flows – Study of Concentrated Dispersions and Suspensions. PhD Thesis, INPG, Grenoble, France.

Coussot, P., Meunier, M., 1996. Recognition, classification and mechanical description of debris flows. Earth-Science Reviews 40, 209-227.

Coviello, V., Arattano, M., Turconi, L., 2015. Detecting torrential processes from a distance with a seismic monitoring network. Nat. Hazards 78, 2055-2080.

Crema, S., Cavalli, M., 2018. SedInConnect: a stand-alone, free and open source tool for the assessment of sediment connectivity. Comput. Geosci. 111, 39–45.

Cucchiaro, S., Cavalli, M., Vericat, D., Crema, S., Llena, M., Beinat, A., Marchi, L., Cazorzi, F., 2019. Geomorphic effectiveness of check dams in a debris-flow catchment using multi-temporal topographic surveys. Catena 174, 73-83.

Cucchiaro, S., Cavalli, M., Vericat, D., Crema, S., Llena, M., Beinat, A., Marchi, L., Cazorzi, F., 2018a. Methodological workflow for topographic changes detection in mountain catchments through 4D-Structure-from-Motion photogrammetry: application to a debris-flow active channel. Environ. Earth Sci. 77, 632.

Cucchiaro, S., Maset, E., Fusiello, A., Cazorzi, F., 2018b. 4D-SfM photogrammetry for monitoring sediment dynamics in a debris-flow catchment: software testing and results comparison. Int. Arch. Photogramm. Remote Sens. Spat. Inf. Sci. XLII-2, 281-288.

D'Agostino, V., 2013. Filtering-retention check dam design in mountain torrents. In: Conesa-Garcia, C., Lenzi, M.A. (Eds.), Check Dams, Morphological Adjustments and Erosion Control in Torrential Streams, Nova Science Publishers, New York, pp. 185-210.

Daehne, A., Corsini, A., 2013. Kinematics of active earthflows revealed by digital image correlation and DEM subtraction techniques applied to multi-temporal LiDAR data. Earth Surf. Process. Landforms.

Deganutti, A.M., Marchi, L., Arattano, M., 2000. Rainfall and debris flow occurrence in the Moscardo basin (Italian Alps). In: Wieczorek, G.F., Naeser, N.D. (Eds.), Debris Flow Hazards Mitigation-Mechanics, Prediction, and Assessment. Balkema, Rotterdam, pp. 67-72.

Dell'Agnese, A., Mazzorana, B., Comiti, F., Von Maravic, P., D'Agostino, V., 2013. Assessing the physical vulnerability of check dams through an empirical damage index. J. Agric. Eng. 44, 1-8.

DeLong, S.B., Prentice, C.S., Hilley, G.E., Ebert, Y., 2012. Multitemporal ALSM change detection, sediment delivery, and process mapping at an active earthflow. Earth Surf. Process. Landforms 37, 262–272.

Destro E., Marra, F., Nikolopoulos, E. I., Zoccatelli, D., Creutin, J. D., and Borga, M., 2017. Spatial estimation of debris flows-triggering rainfall and its dependence on rainfall return period. Geomorphology, 278, 269-279.

Dietrich, J.T., 2017. Bathymetric Structure-from-Motion: extracting shallow stream bathymetry from multi-view stereo photogrammetry. Earth Surf. Process. Landf. 42, 355-364.

Dini, M., 2011. Interventi di salvaguardia ambientale del bacino idrografico del torrente Moscardo in comune di Paluzza (UD) – Progetto esecutivo – Allegato n. 4 – Relazione geologico-tecnica. Regione Autonoma Friuli Venezia Giulia – Direzione centrale risorse rurali, agroalimentari e forestali – Servizio Gestione Territorio Rurale e Irrigazione – Struttura tecnico amministrativa di Tolmezzo (UD).

Eker, R., Aydın, A., Hübl, J., 2018. Unmanned aerial vehicle (UAV)-based monitoring of a landslide: Gallenzerkogel landslide (Ybbs-Lower Austria) case study. Environ. Monit. Assess. 190, 28

Eltner, A., Kaiser, A., Abellan, A., Schindewolf, M., 2017. Time lapse structure-from-motion photogrammetry for continuous geomorphic monitoring. Earth Surf. Process. Landforms 42, 2240-2253.

Eltner, A., Kaiser, A., Castillo, C., Rock, G., Neugirg, F., Abellán, A., 2016. Image-based surface reconstruction in geomorphometry-merits, limits and developments. Earth. Surf. Dyn. 4, 359-389.

Foerster, S., Wilczok, C., Brosinsky, A., Segl, K., 2014. Assessment of sediment connectivity from vegetation cover and topography using remotely sensed data in a dryland catchment in the Spanish Pyrenees. J. Soils Sediments 14.

Fonstad, M.A., Dietrich, J.T., Courville, B.C., Jensen, J.L., Carbonneau, P.E., 2013. Topographic structure frommotion: a new development in photogrammetric measurement. Earth Surf. Process. Landf. 38, 421-430.

Fonstad, M.A., Marcus, W.A., 2010. High resolution, basin extent observations and implications for understanding river form and process. Earth Surface Processes and Landforms 35, 280–298.

Fryirs, K., 2013. (Dis)Connectivity in catchment sediment cascades: A fresh look at the sediment delivery problem. Earth Surf. Process. Landforms.

García-Ruiz, J.M., Alatorre, L.C., Gómez-Villar, A., Beguería, S., 2013. Upstream and downstream effects of check dams in braide drivers, central Pyrenees, in: Conesa-Garcia, C., Lenzi, M.A. (Eds), Check Dams, Morphological Adjustments and Erosion Control in Torrential Streams. Nova Science Publishers, New York, pp. 307–322.

Glendell, M., McShane, G., Farrow, L., James, M.R., Quinton, J., Anderson, K., Evans, M., Benaud, P., Rawlins, B., Morgan, D., Jones, L., Kirkham, M., DeBell, L., Quine, T.A., Lark, M., Rickson, J., Brazier, R.E., 2017. Testing the utility of structure-from-motion photogrammetry reconstructions using small unmanned aerial vehicles and ground photography to estimate the extent of upland soil erosion. Earth Surf. Process. Landf. 42, 1860-1871.

Granshaw, S.I., 1980. Bundle adjustment methods in engineering photogrammetry. Photogramm. Rec. 10, 56, 181-207.

Griffiths, D., Burningham D., 2018. Comparison of pre- and self-calibrated camera calibration models for UAS-derived nadir imagery for a SfM application. Progress in Physical Geography: Earth and Environment.

Gruen, A., 2012. Development and Status of Image Matching in Photogrammetry. Photogramm. Rec. 27, 36–57.

Hassanli, A.M., Beecham, S., 2010. Criteria for optimizing check dam location and maintenance requirements. Check Dams, Morphol. Adjust. Eros. Control Torrential Streams 11–31.

Heckmann, T., Haas, F., Abel, J., Rimböck, A., Becht, M., 2017. Feeding the hungry river: Fluvial morphodynamics and the entrainment of artificially inserted sediment at the dammed river Isar, Eastern Alps, Germany. Geomorphology 291, 128-142.

Heckmann, T., Schwanghart, W., 2013. Geomorphic coupling and sediment connectivity in an alpine catchment - Exploring sediment cascades using graph theory. Geomorphology 182, 89–103.

Heckmann, T., Vericat, D., 2018. Computing spatially distributed sediment delivery ratios: inferring functional sediment connectivity from repeat high ‐ resolution digital elevation models. Earth Surf. Process. Landforms, 43: 1547–1554.

Heritage, G.L., Milan, D.J., Large, A.R.G., Fuller, I.C., 2009. Influence of survey strategy and interpolation model on DEM quality. Geomorphology 112, 334-344.

Hodgson, M.E., Bresnahan, P., 2004. Accuracy of airborne LiDAR-derived elevation: empirical assessment and error budget. Photogramm. Eng. Remote. Sens. 70 (3), 331–339.

Hungr, O., Evans, S. G., Bovis, M. J., and Hutchinson, J. N., 2001. A review of the classification of landslides of the flow type, Environmen. Eng. Geosci. 7, 221-238.

Hungr, O., McDougall, S., Bovis, M., 2005. Entrainment of material by debris flows, in: Jakob, M., Hungr, O. (Eds), Debris-Flow Hazards and Related Phenomena. Praxis. Springer, Berlin Heidelberg, pp. 135–158.

Hungr, O., Morgan, G. C., and Kellerhalls, R., 1984. Quantitative analysis of debris torrent hazards for design of remedial measures, Can. Geotech. J. 21, 663–667.

Hübl, J., Fiebiger, G., 2005. Debris-flow mitigation measures in: Jakob, M., Hungr, O. (Eds), Debris-Flow Hazards and Related Phenomena. Praxis. Springer, Berlin Heidelberg, pp. 445-487.

Hübl, J., Strauss, A., Holub, M., Suda, J., 2005. Structural mitigation measures, in: Proceedings zum 3rd Probabilistic Workshop: Technical Systems + Natural Hazards, 24-25 November, Wien.

Hübl, J., Suda, J., 2008. Debris flow mitigation measures in Austria, in: Debris flows: Disasters, Risk, Forecast, Protection. Sevkavgiprovodkhoz Institute, Pyatigorsk.

Immerzeel, W.W., Kraaijenbrink, P.D.A., Shea, J.M., Shrestha, A.B., Pellicciotti, F., Bierkens, M.F.P., de Jong, S.M., 2014. High-resolution monitoring of Himalayan glacier dynamics using unmanned aerial vehicles. Remote Sens. Environ. 150, 93–103.

IRDAT, 2018. http://irdat.regione.fvg.it/WebGIS. *Accessed 8 August 2018.*

Itakura, Y., Inaba, H., Sawada, T., 2005. A debris-flow monitoring devices and methods bibliography. Nat. Hazards Earth Syst. Sci. 5, 971–977.

Iverson, R. M., 1997. The physics of debris flows, Rev. Geophys. 35, 245–296.

Izumida, A., Uchiyama, S., Sugai, T., 2017. Application of UAV-SfM photogrammetry and aerial lidar to a disastrous flood: repeated topographic measurement of a newly formed crevasse splay of the Kinu River, central Japan. Nat. Hazards Earth Syst. Sci. 17, 1505–1519.

Jaeggi, M.N.R., Pellandini, S., 1997. Torrent check dams as a control measure for debris flows. In: Armanini, A., Michiue, M. (Eds.), Recent Developments on Debris Flows. Springer, Berlin Heidelberg, pp. 186–207.

Jakob, M., 2005. Debris-flow hazard analysis. In: Debris-flow Hazards and Related Phenomena. Jakob, M., Hungr, O. (Eds.), Springer, Berlin, 411-443.

James, M.R., Robson, S., 2012. Straightforward reconstruction of 3D surfaces and topography with a camera: Accuracy and geoscience application. J. Geophys. Res. Earth Surf. 117, 1-17.

James, M.R., Robson, S., 2014. Mitigating systematic error in topographic models derived from UAV and ground-based image networks. Earth Surf. Process. Landf. 39, 1413-1420.

James, M.R., Robson, S., D'Oleire-Oltmanns, S., Niethammer, U., 2017a. Optimising UAV topographic surveys processed with structurefrom-motion: ground control quality, quantity and bundle adjustment. Geomorphology 280, 51–66.

James, M.R., Robson, S., Smith, M.W., 2017b. 3-D uncertainty-based topographic change detection with structure-from-motion photogrammetry: precision maps for ground control and directly georeferenced surveys. Earth Surf. Process. Landf. 42, 1769-1788.

James, M.R., Varley, N., 2012. Identification of structural controls in an active lava dome with high resolution DEMs: Volcn de Colima, Mexico. Geophys. Res. Lett. 39, 1-5.

Javernick, L., Brasington, J., Caruso, B., 2014. Modeling the topography of shallow braided rivers using Structure-from-Motion photogrammetry. Geomorphology 213, 166–182.

Jenness, J., 2013. DEM Surface Tools for ArcGIS (surface_area.exe). Jenness Enterprises. Available at http://www.jennessent.com/arcgis/surface_area.htm. Accessed 12 January 2018.

Johnson, A.M., 1970. Debris Flows. In Physical Processes in Geology: a method for interpretation of natural phenomena, intrusion in igneous rocks, fractures and folds, flow of debris and ice; Freeman, Cooper and co., San Francisco, pp. 433-534.

Johnson, P.A., McCuen, R.H., 1996. Mud and Debris Flows. In: Singh V.P. (Eds.), Hydrology of Disasters, Kluwer Academic Publishers, pp. 161-181.

Kaplinski, M., Hazel, J.E., Grams, P.E., Davis, P.A., 2014. Monitoring Fine-Sediment Volume in the Colorado River Ecosystem, Arizona – Construction and Analysis of Digital Elevation Models. Open File Report 152 Gravel-Bed Rivers: Processes and Disasters 2014-1052, US Geological Survey, Grand Canyon Monitoring Research Center: Flagstaff, AZ, 29.

Keilig, K.P., Dietrich, A., Krautblatter, M., 2019. Comparison of Multi-temporal Elevation Models of a Debris-Flow Channel. In: Shakoor A., Cato K. (Eds) IAEG/AEG Annual Meeting Proceedings, San Francisco, California, 2018 - Volume 1. Springer, Cham.

Kienholz, H., 2003. Early warning systems related to mountain hazards. In: J. Zschau A.N. Kuppers (Eds.), Early Warn. Syst. Nat. disaster reduction, New York, pp. 555–564.

Koci, J., Jarihani, B., Leon, J.X., Sidle, R., Wilkinson, S., Bartley, R., 2017. Assessment of UAV and Ground-Based Structure from Motion with Multi-View Stereo Photogrammetry in a Gullied Savanna Catchment. ISPRS Int. J. Geo-Information, 6, 328.

Kravina, G., 1974. Sistemazioni idraulico forestale del bacino del Moscardo. Rassegna Tecnica del Friuli Venezia Giulia, Anno 25, 24-29.

Lague, D., Brodu, N., Leroux, J., 2013. Accurate 3D comparison of complex topography with terrestrial laser scanner: application to the Rangitikei canyon (N-Z). ISPRS J. of Photogramm. and Remote Sens. 82, 10-26.

Lallias-Tacon, S., Liébault, F., Piégay, H., 2014. Step by step error assessment in braided river sediment budget using airborne LiDAR data. Geomorphology 214, 307–323.

Lane, S.N., Chandler, J.H., 2003. The next generation of high quality topographic data for hydrology and geomorphology: new data sources, new applications and new problems. Earth Surf. Process. Landf. 28, 229-230.

Lane, S.N., Westaway, R.M., Hicks, D.M., 2003. Estimation of erosion and deposition volumes in a large, gravel-bed, braided river using synoptic remote sensing. Earth Surf. Process. Landf. 28, 249-271.

Lenzi, M.A, Comiti, F., 2003. Local scouring and morphological adjustments in steep channels with check dam sequences. Elsevier Science B.V. Geomorphology 55, 97-109.

Lopez Saez, J., Corona, C., Stoffel, M., Gotteland, A., Berger, F., Lièbault, F., 2011. Debris-flow activity in abandoned channels of the Manival torrent reconstructed with LiDAR and tree-ring data. Nat. Hazards Earth Syst. Sci., 11, 1247-1257.

Loye, A., Jaboyedoff, M., Theule, J., Liébault, F., 2016. Headwater sediment dynamics in a debris flow catchment constrained by high-resolution topographic surveys. Earth Surf. Dynamics 4, 489-513.

Meade, R.H., 1982. Sources, sinks, and storage of river sediment in the Atlantic drainage of the United States. J. of Geology, 90, 235-252.

Mallalieu, J., Carrivick, J.L., Quincey, D.J., Smith, M.W., James, W.H.M., 2017. An integrated Structure-from-Motion and time-lapse technique for quantifying ice-margin dynamics. J Glaciol. 63,937-949.

Mao, L., Cavalli, M., Comiti, F., Marchi, L., Lenzi, M.A., Arattano, M., 2009. Sediment transfer processes in two Alpine catchments of contrasting morphological settings. J. Hydrol. 364, 88-98.

Marcato, G., Mantovani, M., Pasuto, A., Zabuski, L., Borgatti, L., 2012. Monitoring, numerical modelling and hazard mitigation of the Moscardo landslide (Eastern Italian Alps). Eng. Geol., Integration of Technologies for Landslide Monitoring and Quantitative Hazard Assessment 128, 95-107.

Marchi, L., Arattano, M., Deganutti, A.M., 2002. Ten years of debris-flow monitoring in the Moscardo Torrent (Italian Alps). Geomorphology 46, 1-17.

Marchi, L., Cavalli, M., D'Agostino, V., 2010. Hydrogeomorphic processes and torrent control works on a large alluvial fan in the eastern Italian Alps. Nat. Hazards Earth Syst. Sci. 10, 547-558.

Marchi, L., Cavalli, M., Sangati, M., Borga, M., 2009. Hydrometeorological controls and erosive response of an extreme alpine debris flow. Hydrol. Process. 23,19, 2714-2727.

Marchi, L., D'Agostino, V., 2004. Estimation of debris-flow magnitude in the Eastern Italian Alps. Earth Surf. Process. Landforms 29, 207-220.

Marteau, B., Vericat, D., Gibbins, C., Batalla, R.J., Green, D.R., 2017. Application of Structure-from-Motion photogrammetry to river restoration. Earth Surf. Process. Landf. 42, 503-515.

Mazzorana, B., Scherer, C., Marangoni, N., 2008. Additional torrent control strategies on debris flow alluvial fans with extremely high vulnerable settlements. In: Sànchez-Marrè, M., Béjar, J., Comas, J., Rizzoli, A., Guariso, G. (Eds.), International Congress on Environmental Modelling and Software. International Environmental Modelling and Software Society (iEMSs).

Mazzorana, B., Trenkwalder-Platzer, H.J., Fuchs, S., Hübl, J., 2014. The susceptibility of consolidation check dams as a key factor for maintenance planning. ÖsterreichischeWasser-und Abfallwirtschaft 66, 214-216.

Micheletti, N., Chandler, J.H., Lane, S.N., 2015a. Investigating the geomorphological potential of freely available and accessible structure- from-motion photogrammetry using a smartphone. Earth Surf. Process. Landf. 40, 473-486.

Micheletti, N., Chandler, J.H., Lane, S.N. 2015b. Structure from Motion (SfM) photogrammetry. In: Cook, S.J., Clarke, L.E., Nield, J.M., (Eds.) Geomorphological Techniques. British Society for Geomorphology, London, pp 1-12.

Milan, D.J., Heritage, G.L., Large, A.R.G., Fuller, I.C. 2011. Filtering spatial error from DEMs: Implications for morphological change estimation. Geomorphology 125, 160-171.

Mosbrucker, A.R., Major, J.J., Spicer, K.R., Pitlick, J., 2017. Camera system considerations for geomorphic applications of SfM photogrammetry. Earth Surf. Process. Landf. 42, 969-986.

Norman, L.M., Niraula, R., 2016. Model analysis of check dam impacts on long-term sediment and water budgets in Southeast Arizona, USA. Ecohydrol. Hydrobiol. 16, 125-137.

O'Connor, J., Smith, M.J., James, M.R., 2017. Cameras and settings for aerial surveys in the geosciences: Optimising image data. Progress in Physical Geography: Earth and Environment 41, 325-344.

Okuda, S., Suwa, H., Okunishi, K., Yokoyama, K., Nakano, M., 1980. Observations on the motion of a debris flow and its geomorphological effects. Zeitschrift fur Geomorphologie, N.F., Supplementband 35, 142-163.

Omnia, 2018. Available at *http://omnia.meteo.fvg.it. Accessed 31 October 2018.*

Osanai, N., Mizuno, H., and Mizuyama, T., 2010. "Design standard of control structures against debris flow in Japan." J. Disaster Res., 5(3), 307-314

Osti, R., Egashira, S., 2008. Method to improve the mitigative effectiveness of a series of check dams against debris flows. Hydrol. Process. 22, 4986-4996.

Passalacqua, P., Belmont, P., Staley, D.M., Simley, J.D., Arrowsmith, J.R., Bode, C.A., Crosby, C., DeLong, S.B., Glenn, N.F., Kelly, S.A., Lague, D., Sangireddy, H., Schaffrath, K., Tarboton, D.G., Wasklewicz, T., Wheaton, J.M., 2015. Analyzing high-resolution topography for advancing the understanding of mass and energy transfer through landscapes: A review. Earth-Science Rev. 148, 174-193.

Persichillo, M.G., Bordoni, M., Cavalli, M., Crema, S., Meisina, C., 2018. The role of human activities on sediment connectivity of shallow landslides. Catena.

Picco, L., Mao, L., Cavalli, M., Buzzi, E., Rainato, R., Lenzi, M.A., 2013. Evaluating short-term morphological changes in a gravel-bed braided river using terrestrial laser scanner. Geomorphology 201, 323–334.

Piermattei, L., Carturan, L., Guarnieri, A., 2015. Use of terrestrial photogrammetry based on structure-from-motion for mass balance estimation of a small glacier in the Italian alps. Earth Surf. Process. Landforms 40, 1791-1802.

Piermattei, L., Karel, W., Vettore, A., Pfeifer, N., 2016. Panorama Image Sets for Terrestrial Photogrammetric Surveys. ISPRS Ann. Photogramm. Remote Sens. Spat. Inf. Sci. III-5, 159-166.

Pierson, T.C., 1986. Flow behavior of channelized debris flows, Mount St. Helens, Washington. In: Abrahms, A.D. (Ed.), Hillslope Processes. Allen and Unwin, Boston, pp. 269-296.

Pierson, T.C., Costa, J.E., 1987. A rheologic classification of subaerial sediment-water flows. In: J.E. Costa and G.F. Wieczorek (Eds.), Debris Flows/Avalanches: Process, Recognition, and Mitigation. Geological Society of America Reviews in Engineering Geology VII, 1-12.

Piton, G., Carladous, S., Recking, A., Tacnet, J., Liebault, F., Kuss, D., Quefféléan, Y., Marc, O., 2016. Why do we build check dams in Alpine streams? An historical perspective from the French experience. Earth Surf. Process. Landf. 42, 91-108.

Piton, G., Recking, A., 2014. The dynamic of streams equipped with check dams. Proceeding of the International Conference on Fluvial Hydraulics, RIVER FLOW 2014, 1437-1445.

Piton, G., Recking, A., 2016. Design of Sediment Traps with Open Check Dams. I: Hydraulic and Deposition Processes. J. Hydraul. Eng. 142, 04015045.

Piton, G., Recking, A., 2017. Effects of check dams on bed-load transport and steep-slope stream morphodynamics. Geomorphology 291, 94-105.

Poeppl, R.E., Keesstra, S.D., Maroulis, J., 2017. A conceptual connectivity framework for understanding geomorphic change in human-impacted fluvial systems. Geomorphology, 277, 237–250.

Puntel, G., 1993. La sistemazione idraulica del Moscardo. Rassegna Tecnica del Friuli Venezia Giulia, Anno 44, 26-30.

Remaître, A., Asch, W.J., Malet, J.P., Maquaire, O., 2008. Influence of check dams on debris-flow run-out intensity. Nat. Hazards Earth Syst. Sci. 8, 1403-1416.

Remaître, A., Malet, J.P., 2013. The effectiveness of torrent check dams to control channel instability: Example of debris-flow events in clay shales. In: Conesa-Garcia, C., Lenzi, M.A. (Eds), Check Dams, Morphological Adjustments and Erosion Control in Torrential Streams. Nova Science Publishers, New York, pp. 211–237.

Remaître, A., Maquaire, O., Malet, J.P., 2005. Morphology and sedimentology of a complex debris flow in clay-shales basin. Earth Surf. Process. Landf. 30, 339-348.

Remondino, F., Nocerino, E., Toschi, I., Menna, F., 2017. A Critical Review of Automated Photogrammetric Processing of Large Datasets. ISPRS - Int. Arch. Photogramm. Remote Sens. Spat. Inf. Sci. XLII-2/W5, 591-599.

Sanz-Ablanedo, E., Chandler, J., Rodríguez-Pérez, J., Ordóñez, C., Sanz-Ablanedo, E., Chandler, J.H., Rodríguez-Pérez, J.R., Ordóñez, C., 2018. Accuracy of Unmanned Aerial Vehicle (UAV) and SfM Photogrammetry Survey as a Function of the Number and Location of Ground Control Points Used. Remote Sens. 2018, Vol. 10, Page 1606 10, 1606.

Scheidl, C., Rickenmann, D., Chiari, M., 2008. The use of airborne LiDAR data for the analysis of debris flow events in Switzerland. Nat. Hazards Earth Syst. Sci. 8, 1113–1127.

Schlunegger, F., Badoux, A., McArdell, B.W., Gwerder, C., Schnydrig, D., Rieke-Zapp, D., Molnar, P., 2009. Limits of sediment transfer in an alpine debris-flow catchment, Illgraben, Switzerland. Quat. Sci. Rev. 28, 1097–1105.

Schürch, P., Densmore, A.L., Rosser, N.J., Lim, M., Mcardell, B.W., 2011. Detection of surface change in complex topography using terrestrial laser scanning: Application to the Illgraben debris-flow channel. Earth Surf. Process. Landf. 36, 1847-1859.

Simoni, S., Vignoli, G., Mazzorana, B., 2017. Enhancing sediment flux control and natural hazard risk mitigation through a structured conceptual planning approach. Geomorphology 291, 159-173.

Smith, M.W., Carrivick, J.L., Hooke, J., Kirkby, M.J., 2014. Reconstructing flash flood magnitudes using "Structure-from-Motion": A rapid assessment tool. J. Hydrol. 519, 1914-1927.

Smith, M., Vericat, D., 2015. From experimental plots to experimental landscapes: topography, erosion and deposition in sub-humid badlands from Structure-from-Motion photogrammetry. Earth Surf. Process. Landf. 40, 1656-1671.

Smith, M.W., Carrivick, J.L., Quincey, D.J., 2015. Structure from motion photogrammetry in physical geography. Prog. Phys. Geogr. 40, 247-275.

Schrott, L., Hufschmidt, G., Hankammer, M., Hoffmann, T., Dikau, R., 2003. Spatial distribution of sediment storage types and quantification of valley fill deposits in an alpine basin, Reintal, Bavarian Alps, Germany. Geomorphology 55, 45–63.

Shortis, M.R., Bellman, C.J., Robson, S., Johnston, G.J., Johnson, G.W., 2006. Stability of Zoom and Fixed Lenses used with Digital SLR Cameras. Int. Arch. Photogramm. Remote Sensing, Spat. Inf. Sci. 36, 285-290.

Stöcker, C., Eltner, A., Karrasch, P., 2015. Measuring gullies by synergetic application of UAV and close range photogrammetry - A case study from Andalusia, Spain. Catena 132, 1-11.

Streutker, D.R., Glenn, N.F., Shrestha, R., 2011. A slope-based method for matching elevation surfaces. Photogramm. Eng. Remote. Sens. 77 (7), 743–750.

Stumpf, A., Malet, J.P., Allemand, P., Pierrot-Deseilligny, M., Skupinski, G., 2015. Ground-based multi-view photogrammetry for the monitoring of landslide deformation and erosion. Geomorphology 231, 130-145.

Suda, J., Hübl, J., and Bergmeister, K., 2010. "Design and construction of high stressed concrete structures as protection works for torrent control in the Austrian Alps." Proc., 3rd Int. Fib Congress, Precast Prestressed Concrete Institute (PCI), Chicago, 1–12.

Takahashi, T., 2007. Debris Flow: Mechanics, Prediction and Countermeasures. Psychology Press, pp. 448.

Tarolli, P., 2014. High-resolution topography for understanding Earth surface processes: Opportunities and challenges. Geomorphology 216, 295-312.

Tarolli, P., Sofia, G., Ellis, E., 2017. Mapping the topographic fingerprints of humanity across. Earth, Eos 98.

TerraScan User's Guide, 2016. Available at https://www.terrasolid.com/download/tscan.pdf *Accessed 31 September 2017.*

Theule, J., Liébault, F., Laigle, D., Loye, A., Jaboyedoff, M., 2015. Channel scour and fill by debris flows and bedload transport. Geomorphology 243, 92–105.

Theule, J.I., Liébault, F., Loye, A., Laigle, D., Jaboyedoff, M., 2012. Sediment budget monitoring of debris-flow and bedload transport in the Manival Torrent, SE France. Nat. Hazards Earth Syst. Sci. 12, 731-749.

Torresan, C., Berton, A., Carotenuto, F., Chiavetta, U., Miglietta, F., Zaldei, A., Gioli, B., 2018. Development and performance assessment of a low-cost UAV laser scanner system (LasUAV). Remote Sens. 10, 1-17.

Trevisani, S., Cavalli, M., 2016. Topography-based flow-directional roughness: potential and challenges. Earth Surf. Dyn. 4, 343-358.

Turner, D., Lucieer, A., de Jong, S.M., 2015. Time series analysis of landslide dynamics using an Unmanned Aerial Vehicle (UAV). Remote Sens. 7.

Vericat, D., Brasington, J., Wheaton, J., Cowie, M., 2009. Accuracy assessment of aerial photographs acquired using lighter than air blimps: low-cost tools for mapping river corridors. River Res Appl. 28, 985-1000.

Vericat, D., Smith, M., Brasington, J., 2014. Patterns of topographic change in sub-humid badlands determined by high-resolution multi-temporal topographic surveys. Catena 120, 164-176.

Vericat, D., Wheaton, J.M., Brasington, J., 2017. Revisiting the Morphological Approach: Opportunities and Challenges with Repeat High-Resolution Topography. In: Tsutsumi, D., Laronne, J.B. (Eds) Gravel-Bed Rivers: Processes and Disasters, 1st edn. John Wiley & Sons Ltd, pp. 121-158.

Veyrat-Charvillon, S., Memier, M., 2006. Stereophotogrammetry of archive data and topographic approaches to debris-flow torrent measurements: calculation of channel-sediment states and a partial sediment budget for Manival torrent (Isère, France). Earth Surf. Process. Landf. 31, 201-219.

Victoriano, A., Brasington, J., Guinau, M., Furdada, G., Cabré, M., 2018. Geomorphic impact and assessment of flexible barriers using multi- temporal LiDAR data: The Portainé mountain catchment (Pyrenees) Geomorphic impact and assessment of fl exible barriers using multi-temporal LiDAR data : The Portainé mountain catchment (Pyrenees). Eng. Geol. 237, 168-180.

Wackrow, R., Chandler, J.H., 2011. Minimising systematic error surfaces in digital elevation models using oblique convergent imagery. The Photogrammetric Record 26, 133, 16-31.

Westoby, M.J., Brasington, J., Glasser, N.F., 2012. 'Structure-from-Motion' photogrammetry: A low-cost, effective tool for geoscience applications. Geomorphology 179, 300-314.

Wheaton, J.M., Brasington, J., Darby, S.E., Sear, D.A., 2010. Accounting for uncertainty in DEMs from repeat topographic surveys: improved sediment budgets. Earth Surf. Process. Landf. 35, 136-156.

Willi, C., Graf, C., Deubelbeiss, Y., Keiler, M., 2015. Methods for detecting channel bed surface changes in a mountain torrent - experiences from the dorfbach torrent. Geogr. Helv. 70, 265–279.

Williams, J.G., Rosser, N.J., Hardy, R.J., Brain, M.J., Afana, A.A., 2018. Optimising 4-D surface change detection: An approach for capturing rockfall magnitude-frequency. Earth Surf. Dyn. 6, 101-119.

Wohl, E., 2017. Connectivity in rivers. Prog. Phys. Geogr. 41, 345–362.

Woodget, A.S., Carbonneau, P.E., Visser, F., Maddock, I.P., 2015, Quantifying submerged fluvial topography using hyperspatial resolution UAS imagery and structure from motion photogrammetry. Earth Surf. Process. Landf. 40, 47-64.

Wulder, M.A., Coops, N.C., 2014. Make Earth observations open access: freely available satellite imagery will improve science and environmental-monitoring products. Nature 513, no. 7516, 30.

Zhang, Z., 1992, Iterative point matching for registration of free-form curves. International J. of Computer Vision 13, 119-152.

Acknowledgements

Alla fine di questa tesi voglio ringraziare tutte le persone che, durante questi tre anni, mi hanno fatto crescere, imparare, migliorare e senza le quali non sarei riuscita a raggiungere questo traguardo.

Il primo doveroso ringraziamento va sicuramente a Prof. Federico Cazorzi che con le sue lezioni mi ha fatto innamorare di questa materia e mi ha guidato e sostenuto sin dalla laurea triennale. I suoi insegnamenti durante le ripide camminate lungo i versanti delle nostre montagne e le piacevoli discussioni d'ufficio hanno rappresentato per me delle esperienze importanti da cui ho potuto capire ed imparare molto.

Desidero ringraziare immensamente Marco Cavalli per avermi fatto crescere in questi anni da ogni punto di vista, seguendomi ad ogni mio passo e dandomi l'opportunità di imparare divertendomi. Grazie per la sua grandissima disponibilità e, soprattutto, per le qualità professionali e umane con cui ho avuto il privilegio di avere a che fare.

Un grazie particolare va a Lorenzo Marchi per avermi insegnato tanto con cura e passione attraverso le sue accurate revisioni. Grazie a Stefano Crema e Alberto De Luca per tutto l'aiuto, i preziosi consigli e il supporto datomi da sempre.

Ringrazio in modo speciale Alberto Beinat per le sue istruttive lezioni e le lunghe chiacchierate, grazie alle quali mi sono appassionata al mondo della topografia e dei GNSS. Grazie per tutto l'aiuto, gli accurati suggerimenti e la pazienza durante i lunghi rilievi sul Moscardo.

Desidero ringraziare Damià Vericat per tutti i suoi preziosi insegnamenti, la disponibilità e per il piacevole periodo trascorso a Lleida. Grazie a Manel Llena per tutto l'aiuto e i bei momenti passati assieme.

Grazie a Paolo Tarolli e Frédéric Liébault per l'accurata revisione di questa tesi che mi ha permesso di arricchire e migliorare il presente lavoro.

Un grazie speciale ad Eleonora Meset per tutti gli scambi di idee, gli utilissimi confronti, l'aiuto e l'amicizia dimostratami in questi anni.

Voglio ringraziare in particolar modo i miei compagni di dottorato: Daniel Lizzi, Gloria Misson e Chiara Palandrani che mi sono stati sempre accanto e hanno condiviso con me fatiche, frustrazioni e soddisfazioni di questi anni di dottorato. Grazie per tutte le scorribande, i tè, le merende e le lunghe chiacchierate.

Grazie ad "8" per aver ospitato i lunghi pranzi di "Quelli del Moscardo" altamente istruttivi sia dal punto di vista scientifico che umano.

Un immenso grazie a tutti gli amici e famigliari che durante il fine settimana mi hanno accompagnato e hanno faticato lungo i sentieri del Moscardo alla ricerca di pluviometri e "non solo". Grazie infinite agli amici di sempre e alla mia squadra che mi hanno aiutato e sopportato in tutti questi anni.

Ovviamente il ringraziamento più importante va alla mia famiglia, senza il cui grande sostegno e instancabile affetto non avrei mai raggiunto questo traguardo. Grazie a mia nonna che prima di tutti mi ha insegnato a riconoscere ed osservare le nostre montagne. Infine, grazie di cuore a Luca per avermi accompagnato nelle uscite sul Moscardo così come nella vita, assieme al quale mi auguro di continuare a condividere le cose più belle e importanti.